# General Disclaimer

One or more of the Following Statements may affect this Document

- This document has been reproduced from the best copy furnished by the organizational source. It is being released in the interest of making available as much information as possible.

- This document may contain data, which exceeds the sheet parameters. It was furnished in this condition by the organizational source and is the best copy available.

- This document may contain tone-on-tone or color graphs, charts and/or pictures, which have been reproduced in black and white.

- This document is paginated as submitted by the original source.

- Portions of this document are not fully legible due to the historical nature of some of the material. However, it is the best reproduction available from the original submission.
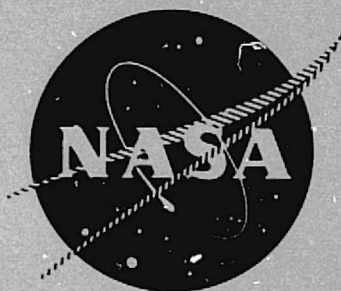
NASA CR-134960

NASA

ANALYTICAL AND EXPERIMENTAL STUDIES OF AN OPTIMUM MULTISEGMENT PHASED LINER NOISE SUPPRESSION CONCEPT

BY
DAVID T. SAWDY, ROY J. BECKEMEYER
AND JOHN D. PATTERSON

MAY 1976

THE *BOEING* COMPANY
WICHITA DIVISION - WICHITA, KANSAS, 67210

BOEING D3-9812-1

PREPARED FOR
NATIONAL AERONAUTICS AND SPACE ADMINISTRATION

NASA-LEWIS RESEARCH CENTER
CONTRACT NAS 3-18550

IG750792

1. Report No. CR-134960	2. Government Accession No.	3. Recipient's Catalog No.
4. Title and Subtitle Analytical and Experimental Studies of An Optimum Multisegment Phased Liner Noise Suppression Concept		5. Report Date May 1976
		6. Performing Organization Code 7000
7. Author(s) David T. Sawdy, Roy J. Beckemeyer and John D. Patterson		8. Performing Organization Report No. D3-9812-1
		10. Work Unit No.
9. Performing Organization Name and Address The Boeing Company Wichita Division Wichita, Kansas 67210		11. Contract or Grant No. NAS 3-18550
		13. Type of Report and Period Covered Contractor Report
12. Sponsoring Agency Name and Address National Aeronautics and Space Administration Washington, D.C. 20546		14. Sponsoring Agency Code

15. Supplementary Notes

Final Report: Project Managers, Dr. Gene Minner and Dr. Kenneth Baumeister, V/STOL and NOISE Division, NASA Lewis Research Center, Cleveland, Ohio 44135

16. Abstract

Results are presented from detailed analytical studies made to define methods for obtaining improved multisegment lining performance by taking advantage of relative placement of each lining segment. Properly phased liner segments reflect and spatially redistribute the incident acoustic energy and thus provide additional attenuation. A mathematical model was developed for rectangular ducts with uniform mean flow. Segmented acoustic fields were represented by duct eigenfunction expansions, and mode-matching was used to ensure continuity of the total field. Parametric studies were performed to identify attenuation mechanisms and define preliminary liner configurations. An optimization procedure was used to determine optimum liner impedance values for a given total lining length, Mach number, and incident modal distribution. Optimal segmented liners are presented and it is shown that, provided the sound source is well-defined and flow environment is known, conventional infinite duct optimum attenuation rates can be improved. To confirm these results, an experimental program was conducted in a laboratory test facility. The measured data are presented in the form of analytical-experimental correlations. Excellent agreement between theory and experiment verifies and substantiates the analytical prediction techniques The results of this study indicate that phased liners may be of immediate benefit in the development of improved aircraft exhaust duct noise suppressors.

17. Key Words (Suggested by Author(s)) Acoustic Lining Eigenfunction Expansions Flow Duct Acoustics Liner Optimization Noise Suppression Sound Propagation	18. Distribution Statement Unclassified - Unlimited
19. Security Classif. (of this report) Unclassified	20. Security Classif. (of this page) Unclassified

19. Security Classif. (of this report) Unclassified	20. Security Classif. (of this page) Unclassified	21. No. of Pages	22. Price*

* For sale by the National Technical Information Service, Springfield, Virginia 22161

NASA-C-168 (Rev. 10-75)

TABLE OF CONTENTS

SUMMARY

More stringent noise regulations for commercial jet aircraft have prompted continuing research into methods for the design of improved engine noise suppression systems. This report presents the results of a research program that was undertaken to analytically and experimentally evaluate the use of phased multisegment linings to provide more efficient attenuation than that provided by current generation liners. Analytical methods were developed to take advantage of relative placement of lining segments so as to reflect and spatially redistribute the acoustic energy incident on the lining. These multisegment linings were shown to outperform single-segment optimum liners. The results of this investigation are immediately applicable to the design of improved aircraft exhaust duct noise suppressors. Further investigations appear to be necessary before phased liner techniques can definitely be shown to be adaptable to inlet liner design. The overall investigation involved analytical studies conducted to identify the principal mechanisms by which phased linings achieve improved attenuations, and the development of methods to utilize these mechanisms in the design of improved liners which were built and then tested in a laboratory facility. The test data were subsequently analyzed both to substantiate and to augment the analytical techniques.

The analyses were based on a mathematical model for rectangular ducts with uniform mean flow. Segmented acoustic fields were represented by duct eigenfunction expansions and mode-matching was used to ensure continuity of the total field. Parametric studies were performed to identify attenuation mechanisms and define preliminary liner configurations. An optimization procedure was used to determine optimum liner impedance values for a given total lining length, Mach number, and incident modal distribution. Optimal segmented liners were developed and it was shown that, provided the sound source is well-defined and flow environment is known, conventional infinite duct optimum attenuation rates can be exceeded. The primary suppression mechanism of the multisegment liners was found to be "modal conditioning." (The incident sound is redistributed by the front liners into modes that are more readily absorbed by the remaining lining segments.)

An experimental program was conducted in a laboratory test facility to confirm the analysis results. The measured data are presented in the form of analytical-experimental correlations. Six lining configurations of one, two and three segments were designed and tested for two flow conditions, $M = 0.0$ and $M = 0.4$. The two- and three-segment liners designed for $M = 0$ produced 4.6 and 6.4 dB more PWL attenuation respectively than the single-segment liner for the design frequency. For the $M = 0.4$ tests, the two- and three-segment liners produced 6.0 and 10.0 dB more attenuation than the single-segment liner. Results of this research demonstrate that acoustic linings with improved suppression effectiveness can be designed for application to future quiet propulsion systems which meet more stringent noise goals.

INTRODUCTION

Background

Current and proposed noise regulations for commercial aircraft have prompted continuing research and development of improved suppression systems for turbofan engines. Although some reduction in turbofan noise has been achieved by suitable engine cycle selection and component design acoustic treatment is still required to suppress the internally generated noise. The imposition of increasingly stringent noise reduction goals, which must be met with minimum impact on airplane performance, requires that acoustic lining design techniques must be continually refined and upated.

Standard uniform infinite duct theories (ref. 1) are based on the assumption that the duct acoustic field includes only modes moving away from the source. The acoustic energy in the duct may then be uniquely associated with the cut-on or propagating modes. Cremer's theory (ref. 2), which involves choosing a liner for which the attenuation rate for the least attenuated mode is optimized, has been reinvestigated in detail by Tester (ref. 3) and Zorumski and Mason (ref. 4).

Rice (ref. 5) has shown that, for an initially plane pressure distribution in an infinite uniform lined duct, the optimum liner would produce much less attenuation than that predicted by the Cremer theory. This is due to the presence of other modes which are required to produce the initial plane pressure wave. The sound power level attenuation rate for the complicated wave system is quite different from that of any single mode. The total sound power includes not only direct contributions from each mode, but also cross terms contributed by modal interaction. For very long ducts the plane wave attenuation per unit length will approach the Cremer value; however, the total attenuation over a given length will be different.

Obviously, this method of approach (See also Snow, ref. 6, who investigated other pressure distributions in addition to the plane wave) should yield more meaningful results than the Cremer theory for the lining lengths typically used in practical applications. However, regardless of which of the infinite theories is used, there are still factors related to finite liner length and the impedance discontinuity at the boundary between liners which have not been taken into account.

Method of Approach

To evaluate finite liner length effects on attenuation performance, acoustic wave reflection from duct nonuniformities should be considered. The computational method generally used for this purpose is the mode matching technique, in which the acoustic field is represented by eigenfunction expansions in terms of incident and reflected duct modes. The undetermined modal coefficients for the field description in any uniform section are determined by requiring continuity of the fields at segment junctions. This method has only recently begun to be applied to acoustic investigations (refs. 7-12) although it has been often used in electromagnetic applications (refs. 13-15).

Lansing and Zorumski (ref. 7) were the first to use this theory to investigate the advantages afforded by the inclusion of impedance discontinuity effects in the evaluation of liner performance. Their preliminary study provided limited insight into the mechanisms responsible for the behavior of the linings. Among the limitations of their study were the facts that liner admittance was assumed constant with frequency, and purely reactive liners were allowed; realistic liners have characteristics which vary with frequency and have finite resistance values.

The present investigation was conceived as an extension of the work of Lansing and Zorumski (ref. 7), aimed at accounting for some of the limitations of their investigation. Identification of the segmented duct mechanisms and experimental verification of predicted performance were primary goals. Realistic liner impedance models were used and very practical constraints on liner design were imposed so that the test panels could be constructed using conventional materials.

To identify mechanisms and develop liner designs, detailed analytical studies were made. These studies involved both extensive parameter variations and numerical optimization runs. Liners chosen for testing were built and installed in a grazing flow duct facility. Performance comparisons and analytical-experimental correlations were based on comparisons of measured and analytical axial distributions of pressure magnitude and phase. The philosophy of the bench-test program was to compare optimum single-segment performance with that of the best multisegment liner which could be built subject to the constraints of material availability and uncertainty regarding details of sound source modal structure.

The multiparameter optimization technique used in the analytical studies to be reported here was the conjugate gradient method. Similar steepest descent algorithms have been used in liner investigations by Martenson and Liu (ref. 16) and Wilkinson (ref. 17) and in expansion chamber studies by Kessler and Puri (ref. 18). However, the present investigation and concurrent work by H. C. Lester and J. W. Posey (private communication) of NASA Langley Research Center appear to be the first in which highly accurate mathematical models and large numbers of parameters (lengths and impedances of multiple segments) have been considered.

NOMENCLATURE

a_n^j Complex modal coefficient for nth right moving mode in jth segment

$\overline{A}$ Liner specific admittance

A_m Value of definite integral defined in Appendix E and G

b_n^j Complex modal coefficient for nth left moving mode in jth segment

B_{mn} Value of definite integral defined in Appendix E

c Speed of sound

C_m Value of definite integral defined in Appendix G

d Denotes differential

D Eigenvalue equation defined in Appendix B

e Denotes base of natural logrithms

E_j Residual error in pressure as defined in Appendix J

g Stands for general acoustic scalar field variable

H Duct height

i One of the two imaginary square roots of -1.0

$\hat{j}$ Unit vector in duct axial direction

J Number of duct segments

$\hat{k}$ Unit vector in duct transverse direction

k Wavenumber $k = \omega/c$

L Total liner length

M Mach number of mean flow

N_j Number of modes in eigenfunction expansion of acoustic field in jth duct segment

p Acoustic pressure

t Time

NOMENCLATURE (CONT'D)

v	Axial acoustic velocity component
$\overline{V}$	Vector acoustic velocity
w	Transverse acoustic velocity component
y	Transverse duct coordinate
z	Axial duct coordinate
Z	Liner specific impedance
α	Real part of modal eigenvalue
β	Imaginary part of modal eigenvalue
Γ_n^j	Constant defined in Appendix G
ζ	Transverse component of acoustic particle displacement
ζ_n	Axial velocity component contributed to right moving wave system by nth eigenfunction (Appendix F)
η	Ratio of duct height to wavelength of sound, $\eta = H/\lambda$
λ	Wavelength of sound, $\lambda = 2\pi c/\omega$
μ	Eigenvalue
ν	Dimensionless propagation constant, $\nu = \lambda/k$
ξ	Quantity defined in Appendix A
ξ_n	Axial velocity component contributed to left moving wave system by nth eigenfunction (Appendix F)
π	Ratio of the length of the circumference of a circle to the diameter
Π	Axial acoustic energy flux
ρ	Mass density of fliud
σ_n^j	Constant defined in Appendix G

NOMENCLATURE (CONT'D)

Φ Phase angle in radians

Φ_n Pressure component contributed to right moving wave system by nth eigenfunction (Appendix F)

ψ_n Pressure component contributed to left moving wave system by nth eigenfunction (Appendix F)

ω Frequency (radians/second)

SUPERSCRIPTS

(prime)   Denotes acoustic field scalar function of time and of the axial and transverse coordinates

*   Denotes complex conjugate

j   Denotes jth segment

$\longleftarrow$ Denotes right moving wave

$\longrightarrow$ Denotes left moving wave

SUBSCRIPTS

n   Denotes nth mode

j   Denotes jth segment

LIST OF FIGURES

PAGE

LIST OF TABLES

THEORETICAL DEVELOPMENT

Problem Formulation

An analytical technique has been developed for studying the propagation of sound waves in flow ducts with segmented liners. The configuration investigated consists of a uniform geometry two-dimensional duct containing uniform mean flow with the duct linings and the acoustic excitation symmetric about the duct centerline. The acoustically lined segments were placed in an infinite hard-walled duct and the reflection and transmission characteristics resulting from incidence of a specified combination of duct modes were investigated. Acoustic fields for ducts with nonuniform boundary conditions have been described by eigenfunction expansions (refs. 7-9), perturbation techniques (refs. 19-21), finite difference formulations (refs. 22-23), and variational and weighted-residual approaches (refs. 10, 11, 24, 25). The geometry of the present problem makes it amenable to efficient solution by the mode matching or eigenfunction expansion method. The problem was, therefore, formulated as a multiregion coupled boundary value problem. Since the boundaries of the duct correspond to coordinate surfaces of a rectangular coordinate system for each region, the acoustic fields may be expressed in terms of eigenfunctions which explicitly satisfy the Helmholtz equation and the wall boundary conditions. In addition, to ensure continuity of the field, solutions in each region must have coinciding boundary data at the junction between regions.

Acoustic Field in Duct Segment

Duct Eigenmodes

The acoustic field in a two-dimensional flow duct is governed by the convected wave equation and by the axial and transverse components of the momentum equation:

$$\frac{\partial^2 p'}{\partial y^2} + (1 - M^2) \frac{\partial^2 p'}{\partial z^2} - \frac{1}{c^2} \frac{\partial^2 p'}{\partial t^2} - \frac{2M}{c} \frac{\partial^2 p'}{\partial z \, \partial t} = 0, \tag{1}$$

$$\rho \frac{\partial w'}{\partial t} + \rho c M \frac{\partial w'}{\partial z} = - \frac{\partial p'}{\partial z} \quad , \text{ and} \tag{2}$$

$$\rho \frac{\partial v'}{\partial t} + \rho c M \frac{\partial v'}{\partial z} = - \frac{\partial p'}{\partial y} \tag{3}$$

The primed symbols used to denote the physical quantities in these equations are functions of y, z and t. The perturbation velocity $\overline{V}'$, a vector field, is defined in terms of its axial and tranverse components.

$$\overline{V}' = v'\hat{j} + w'\hat{k}$$

$$v' = \frac{\partial \zeta'}{\partial t} + cM \frac{\partial \zeta'}{\partial z} \tag{4}$$

where the axial component is expressed in terms of axial particle displacement ζ'

The axial wave propagation and exponential time dependence are characterized by:

$$g'(y,z,t) = g(y)e^{i\omega t - i\lambda z} \tag{5}$$

where g' stands for fields p', v', w', or ζ', and unprimed quantities are functions of y alone.

Use of equation (5) in (1) to (3) yields the following set of reduced governing equations:

$$\frac{\partial^2 p}{\partial y^2} + k^2 [(1 - \nu M)^2 - \nu^2] \, p = 0$$

$$w = \lambda p / [\rho c k (1 - \nu M)] \tag{6}$$

$$v = i \frac{\partial p}{\partial y} / [\rho c k (1 - \nu M)]$$

$$\zeta = -iv / [ck(1 - \nu M)]$$

The boundary condition at a normally-reacting acoustically lined wall is derived by imposing continuity of acoustic particle displacement normal to the wall (ref. 26). This assumption results in the expression:

$$\frac{\partial p}{\partial y} = -ik\overline{A}(1 - \nu M)^2 \quad \text{at wall} \tag{7}$$

where $\overline{A}$ is the specific acoustic admittance of the wall. For the symmetric duct configuration the transverse variation of the pressure field is given by the symmetric eigenmodes which are expressed in terms of eigenvalues μ_n.

$$P_n = \cos(\mu_n y)$$

The eigenvalues μ_n satisfy:

$$\mu_n \tan(\mu_n y) - ik\overline{A}(1 - \nu_n M)^2 = 0 \tag{8}$$

at the wall, and are related to the modal propagation constants ν_n:

$$\mu_n^2 = k^2 [(1 - \nu_n M)^2 - \nu_n^2]$$

2

For the hard-wall duct (A = 0.0) the eigenvalues are

$$\mu_n = 2n\pi/H$$

(H being the duct height).

Table 1 contains a summary of the eigenvalue equations and definition of the propagation constants $\lambda_n = \nu_n k$ for the hard-walled and soft-walled ducts with and without mean flow. Rationale for these definitions is given in Appendix A.

Solutions to the duct eigenvalue equation (8) have been obtained by three different numerical techniques:

- Newton-Raphson iteration (refs. 27-28)

- Numerical integration of a differential equation which has eigenvalue equation as a solution (refs. 4-5) (see Appendix B)

- Rayleigh-Ritz technique (Appendix C)

Multiple eigenvalues associated with the Cremer optimum impedance values were determined using the method of Tester (ref. 3) (see Appendix D). Zorumski and Mason (ref. 4) have shown that the conventional duct eigenfunction expansions are no longer valid at the Cremer optimum. To avoid having to alter the form of the eigenfunction expansions used in these algorithms, exact Cremer impedance values were never used in computing segmented liner performance. It was found that by choosing an impedance several percent off the exact Cremer value, adequate eigenvalue separation could be obtained to ensure validity of the conventional expansion with little loss in accuracy of the performance predictions.

Eigenfunction Expansions

The acoustic fields in each of the duct segments are represented by eigenfunction expansions in terms of right moving (incident) and left moving (reflected) modes. The axial variation of these modes is defined so that they are phased with respect to the point of generation; right moving modes have zero phase at the left end, and left moving or reflected modes have zero phase at the right-hand end of the segment.

Modal expansions for the incident hard-wall, a typical soft-wall, and the transmitting (semi-infinite) hard-walled segments, respectively (Figure 1), are given by:

$$P_o = \sum_{n=0}^{N_o-1} a_n^o \cos(2n\pi y/H)\, e^{-i\overrightarrow{\lambda}_n^o z} + \sum_{n=0}^{N_o-1} b_n^o \cos(2n\pi/H)\, e^{-i\overleftarrow{\lambda}_n^o z} \tag{9}$$

$$p_j = \sum_{n=0}^{N_j-1} a_n^j \cos(\overrightarrow{\mu}_n^j y)\, e^{-i\overrightarrow{\lambda}_n^j z_j} + \sum_{n=0}^{N_j-1} b_n^j \cos(\overleftarrow{\mu}_n^j y)\, e^{-i\overleftarrow{\lambda}_n^j (z_j - L_j)} \tag{10}$$

3

TABLE 1
SUMMARY OF EIGENVALUE EQUATIONS AND PROPAGATION CONSTANTS, SYMMETRIC DUCT MODES

$$P_n = \cos(\mu_n y)e^{iwt - i\lambda_n z}$$

	HARD-WALLS	SOFT-WALLS
WITH MEAN FLOW	$\mu_n = 2n\pi/H$ $\overrightarrow{\lambda_n} = \begin{cases} \dfrac{-kM}{1-M^2} - \dfrac{ik}{1-M}2 \left[(2n\pi/kH)^2 (1-M^2)-1\right]^{1/2}, & (\frac{2n\pi}{kH})^2 > \dfrac{1}{1-M^2} \\ \dfrac{-kM}{1-M^2} + \dfrac{k}{1-M}2 \left[1-(1-M^2)(2n\pi/kH)^2\right]^{1/2}, & (\frac{2n\pi}{kH})^2 < \dfrac{1}{1-M^2} \end{cases}$ $\overleftarrow{\lambda_n} = \begin{cases} \dfrac{-kM}{1-M^2} + \dfrac{k}{1-M}2 \left[(2n\pi/kH)^2 (1-M^2)-1\right]^{1/2}, & (\frac{2n\pi}{kH})^2 > \dfrac{1}{1-M^2} \\ \dfrac{-kM}{1-M^2} - \dfrac{k}{1-M}2 \left[1-(1-M^2)(2n\pi/kH)^2\right]^{1/2}, & (\frac{2n\pi}{kH})^2 < \dfrac{1}{1-M^2} \end{cases}$	$\mu_n H \tan(\mu_n H/2) - ik\,A(1 - \nu_n/M^2\,H = 0,\ \nu_n - \lambda_n/k$ $\overrightarrow{\lambda_n} = \dfrac{-kM}{1-M}2 - \dfrac{k}{1-M}2 \left[1-(\mu_n/k)^2(1-M^2)\right]^{1/2}$ $\overleftarrow{\lambda_n} = \dfrac{-kM}{1-M}2 + \dfrac{k}{1-M}2 \left[1-(\mu_n/k)^2(1-M^2)\right]^{1/2}$ $\left[1-(\mu_n/k)^2(1-M^2)\right]^{1/2} = \alpha_n + i\beta_n,\ \beta_n > 0$
WITHOUT MEAN FLOW	$\overrightarrow{\lambda_n} = \begin{cases} \left[k^2 - (2n\pi/H)^2\right]^{1/2}, & k > 2n\pi/H \\ -i\left[(2n\pi/H)^2 - {}^2\right]^{1/2}, & k < 2n\pi/H \end{cases}$ $\overleftarrow{\lambda_n} = \begin{cases} -\left[k^2 - (2n\pi/H)^2\right]^{1/2}, & k > 2n\pi/H \\ i\left[(2n\pi/H)^2 - k^2\right]^{1/2}, & k < 2n\pi/H \end{cases}$	$\overrightarrow{\lambda_n} = -\left[k^2 - \mu_n^2\right]^{1/2}$ $\overleftarrow{\lambda_n} = \left[k^2 - \mu_n^2\right]^{1/2}$ $\left[k^2 - \mu_n^2\right]^{1/2} = \alpha_n + i\beta_n,\ \beta_n > 0$

4
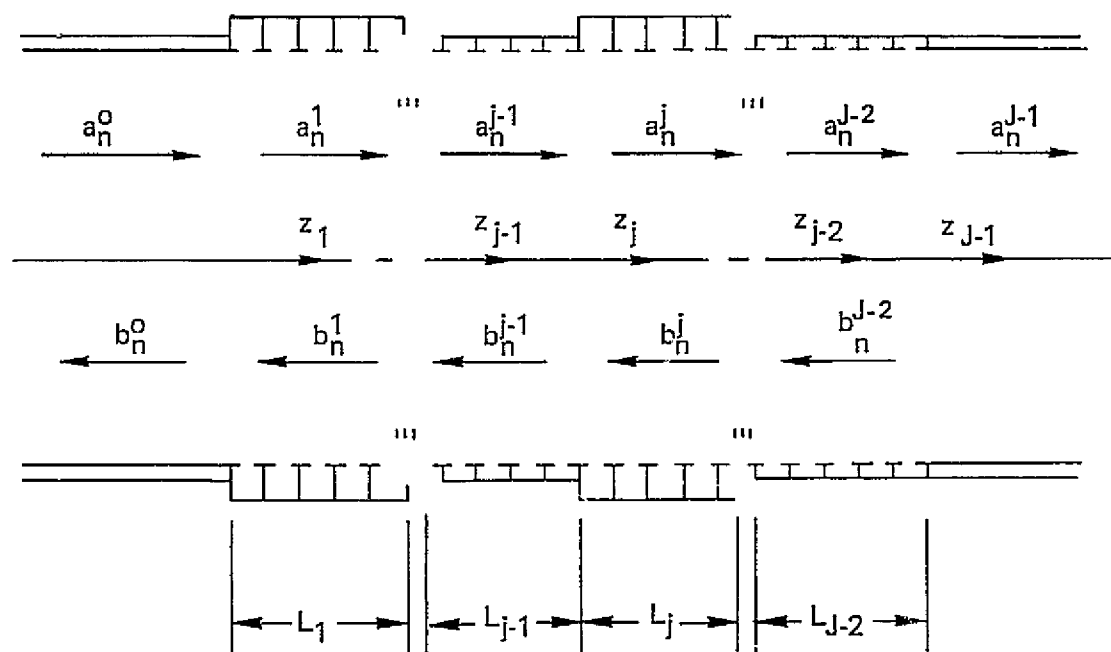
Figure 1. Notation for Segmented Duct Model

and

$$P_{J-1} = \sum_{n=0}^{N_{J-1}-1} a_n^{J-1} \cos(2n\pi y/H) e^{-i\overrightarrow{\lambda}_n^{J-1} z_{J-1}} \tag{11}$$

The a_n^o are the known modal coefficients of the incident sound field. Expressions for the axial acoustic particle velocity in each region are:

$$k\rho c w_o = \sum_{n=0}^{N_o-1} \frac{a_n^o \overrightarrow{\lambda}_n^o}{(1-\overrightarrow{\lambda}_n^o M/k)} \cos(2n\pi y/H) e^{-i\overrightarrow{\lambda}_n^o z} + \sum_{n=0}^{N_o-1} \frac{b_n^o \overleftarrow{\lambda}_n^o}{(1-\overleftarrow{\lambda}_n^o M/k)} \cos(2n\pi y/H) e^{-i\overleftarrow{\lambda}_n^o z} \tag{12}$$

$$k\rho c w_j = \sum_{n=0}^{N_j-1} \frac{a_n^j \overrightarrow{\lambda}_n^j}{(1-\overrightarrow{\lambda}_n^j M/k)} \cos(\overrightarrow{\mu}_n^j y) e^{-i\lambda_n^j z} + \sum_{n=0}^{N_j-1} \frac{b_n^i \overleftarrow{\lambda}_n^i}{(1-\overleftarrow{\lambda}_n^i M/k)} \cos(\overleftarrow{\mu}_n^i y) e^{-i\overleftarrow{\lambda}_n^j (z_j - L_j)} \tag{13}$$

$$k\rho c w_{J-1} \sum_{n=0}^{N_{J-1}-1} \frac{a_n^{J-1} \overrightarrow{\lambda}_n^{J-1}}{(1-\overrightarrow{\lambda}_n^{J-1} M/k)} \cos(\overrightarrow{\mu}_n^{J-1} y) e^{-i\overrightarrow{\lambda}_n^{J-1} z_{J-1}} \tag{14}$$

Matching of Segment Acoustic Fields

Continuity to first order of mass and momentum between adjacent duct segments can be ensured by imposing continuity of acoustic pressure and axial acoustic particle velocity, respectively. The errors in pressure, $p^j - p^{j+1}$, and velocity, $w^j - w^{j+1}$, at the duct cross section between segments j and $j + 1$ are minimized by use of the method of weighted residuals. By multiplying the pressure residual by the left moving modes in segment j and the velocity residual by the right moving modes in segment $j + 1$, and requiring that the errors be orthogonal to each mode of the expansion, the following matching equations are obtained:

$$\int_{-H/2}^{H/2} (p^j - p^{j+1}) \cos(\overleftarrow{\mu}_m^j y) dy = 0, \quad m = 0, (1), N_{j-1}-1, \quad \text{and} \tag{15}$$

$$\int_{-H/2}^{H/2} (w^j - w^{j+1}) \cos(\overrightarrow{\mu}_m^{j+1} y) dy = 0, \quad m = 0, (1), N_{j+1}-1 \tag{16}$$

This matching procedure involves the tacit assumption that the eigenfunctions form a complete set. Although completeness can be proved for the no-mean flow modal functions and for the mean flow hard-wall duct functions, proof of the completeness of the mean-flow soft-wall eigenfunctions is not available. (If they are not complete, the whole concept of eigenfunction expansions becomes invalid; thus, they are assumed to be complete.)

Closed form expressions for the duct matching equations (15) and (16) are given in Appendix E for various interfaces in a two-dimensional symmetric duct. These equations are summarized in matrix form on Figures 2 and 3 for the case of a semi-infinite hard-wall termination and for an arbitrary nonuniform termination, respectively. Development of the arbitrary termination equations is given in Appendix F. It was necessary to allow for this case in order to model the termination characteristics of the test flow duct facility. The duct termination was designed to minimize acoustic reflections for a lower frequency regime, but it was not anechoic at the frequencies used in the present investigation.

Energy Flux Expressions

Several energy flux expressions are available in the literature for describing acoustic energy transmission in ducts with parallel mean flow fields. As noted by Goldstein (ref. 29), the acoustic energy flux and acoustic intensity cannot be uniquely defined. There are thus several expressions available. Two expressions were selected for use in this study: a) the form presented by Morfey (ref. 30), and b) that suggested by Ryshov and Shefter (ref. 31). In terms of the problem variables, these are:

$$\Pi_a = \frac{1}{2} \text{REAL} \left\{ \int_{-H/2}^{H/2} \left[(1+M^2) \, p \, w^* + \frac{M}{\rho c} \, p \, p^* + M \rho c \, w \, w^* \right] dy \right\}$$

$$\Pi_b = \frac{1}{2} \text{REAL} \left\{ \int_{-H/2}^{H/2} \left[p \, w^* + \frac{M \rho c}{2} (v \, v^* + w \, w^*) + \frac{M}{2\rho c} \, p \, p^* \right] dy \right\}$$

(17)

where Π is the axial acoustic energy flux and the asterisk denotes the complex conjugate.

A measure of the accuracy of acoustic field matching may be obtained by computing the axial energy flux on either side of a junction between duct segments. Both flux expressions have been found to provide an accurate measure of field matching, although generally the values computed using the Morfey expression match more closely. Unless otherwise noted, all liner performance values (sound power attenuations) quoted in this report are based on the Morfey expressions for energy flux.

Appendix G contains energy flux expressions for hard-wall incident, hard-wall transmitting, and soft-wall segments. The incident energy flux contains cross product terms due to interaction of incident and reflected modes. These terms can contribute to incident energy even if all modes are cut off. It is also significant that, in general, the energy dissipation in a soft-walled segment cannot be inferred from modal attenuation rates.

7
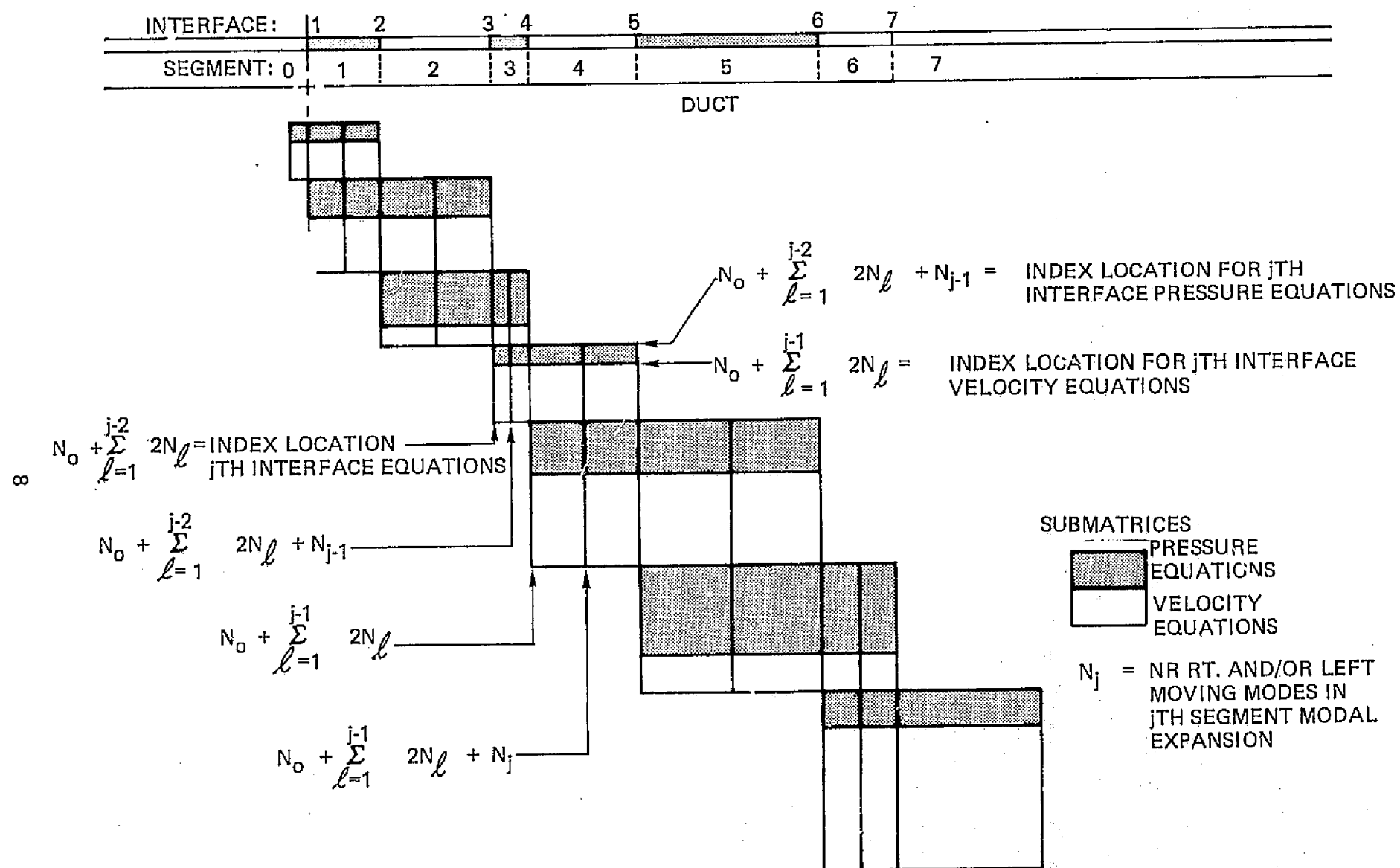
Figure 2. Matrix Form of Duct Acoustic Field Matching Equations - Semi-Infinite Termination

INTERFACE: 1 2 3 4 5 6 7

SEGMENT: 0 1 2 3 4 5 6 7

DUCT

$N_o + \sum_{\ell=1}^{j-2} 2N_\ell + N_{j-1} =$ INDEX LOCATION FOR jTH INTERFACE PRESSURE EQUATIONS

$N_o + \sum_{\ell=1}^{j-1} 2N_\ell =$ INDEX LOCATION FOR jTH INTERFACE VELOCITY EQUATIONS

$N_o + \sum_{\ell=1}^{j-2} 2N_\ell =$ INDEX LOCATION jTH INTERFACE EQUATIONS

$N_o + \sum_{\ell=1}^{j-2} 2N_\ell + N_{j-1}$

$N_o + \sum_{\ell=1}^{j-1} 2N_\ell$

$N_o + \sum_{\ell=1}^{j-1} 2N_\ell + N_j$

SUBMATRICS
PRESSURE EQUATIONS
VELOCITY EQUATIONS

$N_j =$ NR RT. AND/OR LEFT MOVING MODES IN jTH SEGMENT MODAL EXPANSION

R -I

R REFLECTION COEFFICIENT MATRIX REPRESENTING ARBITRARY DUCT TERMINATION

I UNIT MATRIX

Figure 3. Matrix Form of Duct Acoustic Field Matching Equations. Nonuniform Termination.

Semi-Infinite and Infinite Duct Liners

Two additional duct lining models were developed to provide comparisons with published data for checkout of the mode matching equations and for comparison of finite and infinite duct theories. The first involves the junction between a semi-infinite hard-walled and a semi-infinite soft-walled duct. This case, which allows the estimation of single interface effects and for frequencies below second mode cut-on, provides a comparison with closed form solutions available in the literature (ref. 32).

The matching equations for the semi-infinite case are:

$$
\sum_{\ell=0}^{N_1-1} a_\ell^1 \left\{ \sum_{n=0}^{N_0-1} \left[\frac{\overleftarrow{\lambda}_n^0 \overrightarrow{\mu}_\ell^1 H^2 (-1)^m \sin(2\overrightarrow{\mu}_\ell^1/H)}{2(1-\overleftarrow{\lambda}_n^0 M/k)[(\overrightarrow{\mu}_\ell^1)^2 - (n\pi)^2] A_n} \int_{-H/2}^{H/2} \cos(2n\pi y/H)\cos(\overrightarrow{\mu}_m^1 y)\, dy \right. \right.
$$

$$
\left. - \frac{\overrightarrow{\lambda}_\ell^1}{1-\overrightarrow{\lambda}_\ell M/k} \int_{-H/2}^{H/2} \cos(\overrightarrow{\mu}_\ell^1 y)\cos(\overrightarrow{\mu}_m^1 y)\, dy \right\} \tag{18}
$$

$$
= \sum_{n=0}^{N_0-1} a_n^0 \left[\left(\frac{\overleftarrow{\lambda}_n^0}{1-\overleftarrow{\lambda}_n^0 M/k} - \frac{\overrightarrow{\lambda}_n^0}{1-\overrightarrow{\lambda}_n^0 M/k} \right) \int_{-H/2}^{H/2} \cos(2n\pi y/H)\cos(\overrightarrow{\mu}_m^1 y)\, dy \right]
$$

for $m = 0, (1), N_1-1$

$$
b_m^0 = -a_n^0 + \sum_{n=0}^{N_1-1} a_n^1 \left[\frac{\overrightarrow{\mu}_n^1 H^2 (-1)^m \sin(\overrightarrow{\mu}_n^1 H/2)}{(\overrightarrow{\mu}_n^1)^2 - (m\pi)^2} \right] / A_m
$$

for $m = 0, (1), N_1-1$

$$
A_m = \begin{cases} H, & m = 0 \\ H/2, & m > 0 \end{cases}
$$

The second model is for an infinite soft-wall (Rice's model, ref. 33) in which the attenuation characteristics of specified initial transverse pressure distributions are investigated. For an infinite soft-walled duct with an initial pressure distribution defined by:

$$
p = \sum_{n=0}^{N_0-1} a_n^0 \cos(2n\pi y/H) \qquad \text{at} \qquad z = 0 \tag{19}
$$

the Fourier decomposition of the soft-wall pressure field is:

$$p = \sum_{n=0}^{N_1-1} a_n^1 \cos(\vec{\mu}^1 y)\, e^{-i\vec{\lambda}_n z} \tag{20}$$

where

$$a_n^1 = \sum_{n=0}^{N_1-1} a_n^0 \left\{ \frac{\vec{\mu}_\ell^1 H(-1)^n \sin(\vec{\mu}_\ell^1 H/2)}{[(\vec{\mu}_\ell^1 H/2)^2 - (n\pi)^2]\left[1 + \sin(\vec{\mu}_\ell^1 H)/(\vec{\mu}_\ell^1 H)\right]} \right\} \tag{21}$$

In either case, the axial energy flux in the soft-wall duct is:

$$\Pi_a = \frac{1}{2\rho c} \text{REAL} \sum_{n=0}^{N_1-1} \sum_{m=0}^{N_1-1} a_n^0 (a_m^0)^* e^{-i(\vec{\lambda}_n^1 - (\vec{\lambda}_m^1)^*)z} \; \bullet$$

$$\bullet \left[M + (1+M^2)\left(\vec{\Gamma}_m^1\right)^* + M\,\vec{\Gamma}_n^1\left(\vec{\Gamma}_m^1\right)^* \right]\left[\frac{2\cos(\vec{\mu}_n^1 H/2)\cos((\vec{\mu}_m^1)^* H/2)}{(\vec{\mu}_n^1)^2 - ((\vec{\mu}_m^1)^*)^2} \right] \bullet$$

$$\bullet \left[\vec{\mu}_n^1 \tan(\vec{\mu}_n^1 H/2) - (\vec{\mu}_m^1)^* \tan((\vec{\mu}_m^1)^* H/2) \right] \tag{22}$$

The reference energy flux is given by equation (G1) of Appendix G (with the $b_m^0 = 0$) for the semi-infinite case, but by equation (22) with $z = 0$ for the infinite duct case.

Analytical Results

Computational investigations were performed to identify attenuation mechanisms and define optimum segmented liner configurations. Because of the large number of parameters involved, a multivariable optimization technique was used to determine segmented configurations that produced maximum attenuation for specified modal inputs. The conjugate gradient optimization technique was used, with the total sound power attenuation as a cost function, and various constrained segment lengths and resistive and reactive impedances as independent variables. Excellent results were obtained, but it should be pointed out that the optimum liners referred to here are generally local optimums but not necessarily global optimums. Also, the local optimum obtained in any given solution may vary depending on the starting values and the optimization variable step sizes.

In all of these studies the acoustic source was specified by a set of incident modal pressure amplitudes in the left-hand hard-walled segment. To ensure adequate representation of acoustic fields, ten terms were used in the eigenfunction expansions [equations (9) through (14)]. Pressure and particle velocity profiles were calculated on both sides of each interface to verify that the total acoustic fields were continuous. Sound power levels were also calculated for both sides of each interface and found to match to within a few percent for small to moderate values of attenuation. Soft-wall eigenvalues, modal expansion coefficients, and sound power levels for single and multiple segment liners were checked and found to agree with corresponding results obtained by J. F. Unruh, who used the mode matching method to study single segment liners at very low frequencies (ref. 34).

Single segment optimum liners were used as baseline configurations against which to measure the performance of the multisegment configurations. For the lengths and frequencies under consideration, the optimum single-segment liners were identical to those which would be obtained using the infinite lined duct theory of Rice (ref. 5), as pointed out in Appendix H. The finite and infinite theories produce conflicting results for optimum single-segment liners only for cases in which the excitation frequency is quite close to a cut-on frequency for a low order mode or when the segment length is very small compared with the wavelength of the incident sound. For the latter cases more sound can be reflected by low resistance liners using length resonance effects than can be attenuated by high resistance dissipative liners.

Two-Segment Optimum Liners

Figure 4 shows the results of a two-segment plane wave constrained optimization run. For this case the total lining length and the second segment impedance were held constant while the first segment length and impedance were allowed to vary. The resistance of the first segment was constrained so as to maintain a reactive front liner. Total attenuation for the single-segment optimum for this case was 17.9 dB; the attenuation provided by the two-segment liner was 28.9 dB, obviously a substantial improvement. One of the most significant discoveries made during the multisegment studies is well illustrated by this case. On Figure 4 the attenuation contributions due to reflection from the first interface, absorption in the first segment, and absorption in the second segment, respectively, have been plotted separately versus iterations in the optimization procedure. As shown, there is effectively no reflection taking place. Increased attenuation for the final configuration is due solely to the fact that the first liner has varied the modal content (or, equivalently, the transverse pressure distribution) of the sound incident on the second segment. This made the second segment more effective. Figures 5 through 10 show the results of an investigation into the nature of the modal redistribution caused by the front liner of this two-segment configuration.

Detailed pressure and velocity data at the inlet side of the dissipative liner were computed for both the initial "a" and final "b" two-segment configurations defined on Figure 5. Here "a" refers to the configuration chosen as the initial guess to the optimum liner and "b" to the configuration identified by the optimization algorithm as the best liner for attenuation of the incident plane wave. In addition, the dissipative liner was placed as a single-segment into a hard-walled duct (Figure 5) and subjected to various incident modal combinations to determine the source configuration for which the liner produced maximum attenuation. Figures 6 and 7 illustrate the results obtained, and show that optimum attenuation was obtained for the case with the first and second modes incident with 48 percent of the incident energy in the first mode, 52 percent in the second, and with the second mode phased 100 degrees with respect to the first mode.

12

TWO SEGMENT CONSTRAINED OPTIMIZATION
PLANE WAVE INPUT, kH = 10.0

INDEPENDENT VARIABLES: L_1, Z_1

CONSTRAINTS: $.15H \leq L_1 \leq 1.5H$
REAL $(Z_1) \leq 0.1$

FIXED PARAMETERS: $L_1 + L_2 = 3.0H$
$Z_2 = 1.581 - 1.340i$

STARTING VALUES: $Z_1 = 0.05 - 1.0i$ (REACTIVE LINER)
$L_1 = 0.5H$

FINAL VALUES: $Z_1 = .079 - 1.401i$
$L_1 = .526H$

A: $10 \log_{10} (\Pi_R / \Pi_I)$

B: $10 \log_{10} (\Pi_{T_1} / \Pi_I) - 10 \log_{10} (\Pi_R / \Pi_I)$

C: $10 \log_{10} (\Pi_{T_2} / \Pi_I) - 10 \log_{10} (\Pi_{T_1} / \Pi_I)$

TOTAL ATTENUATION in dB = A + B + C

ΔdB

NUMBER OF ITERATIONS
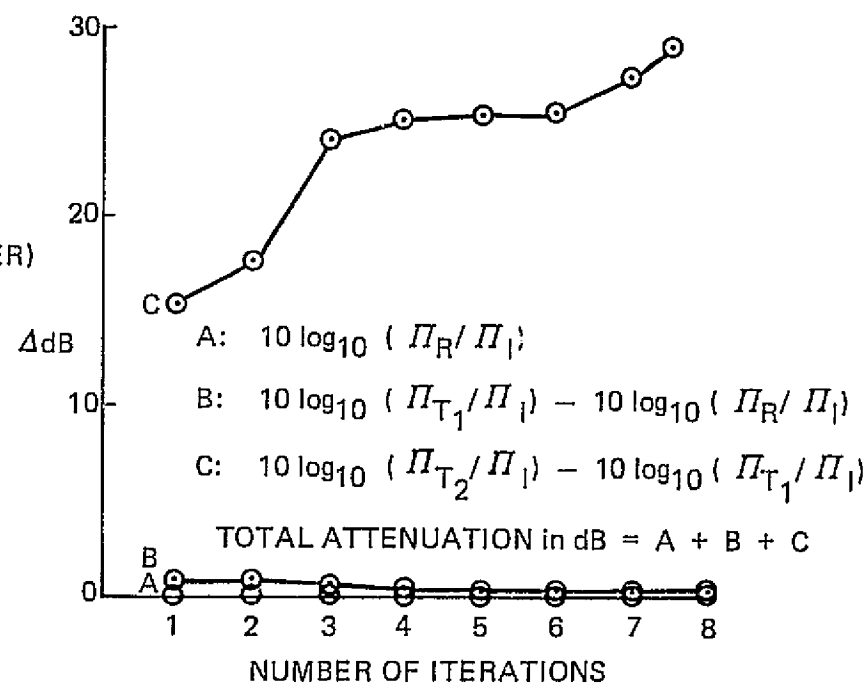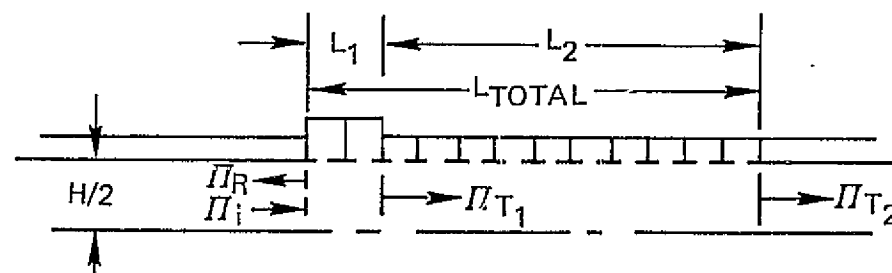
Figure 4. Determination of Constrained Optimum Two-Segment Plane Wave Liner Using Conjugate
Gradient Optimization Technique, M = 0.0.

a.

INITIAL TWO SEGMENT DUCT, PLANE WAVE INCIDENT,
Z_1 = .05 - 1.0i, Z_2 = 1.581 - 1.34i

b.

FINAL TWO SEGMENT DUCT, PLANE WAVE INCIDENT,
Z_1 = .079 - 1.405i, Z_2 = 1.581 - 1.34i

c.

SINGLE SEGMENT DUCT, LINER = 2ND SEGMENT OF CONFIGURATION b,
Z = 1.581 - 1.34i, SUBJECT TO INCIDENT MODES FOR WHICH THIS SINGLE
SEGMENT PRODUCES MAXIMUM ATTENUATION, 47.6% OF INCIDENT
ENERGY IN PLANE WAVE, 52.4% IN SECOND MODE, SECOND MODE
PHASED 105° WITH RESPECT TO PLANE WAVE

Figure 5. Two-Segment Liner Configurations Used in Attenuation Mechanisms Study.
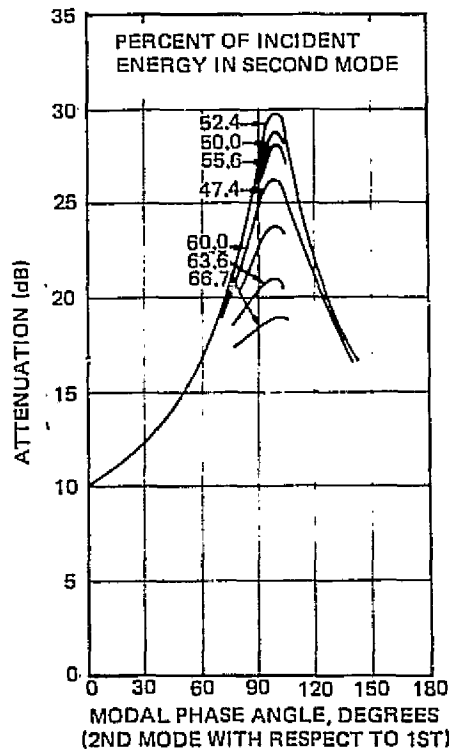
Figure 6.   Performance of Aft Section of Two-Segment Liner as Function of
Equivalent Hard-Wall Modal Distribution of Incident Sound, M = 0.

14
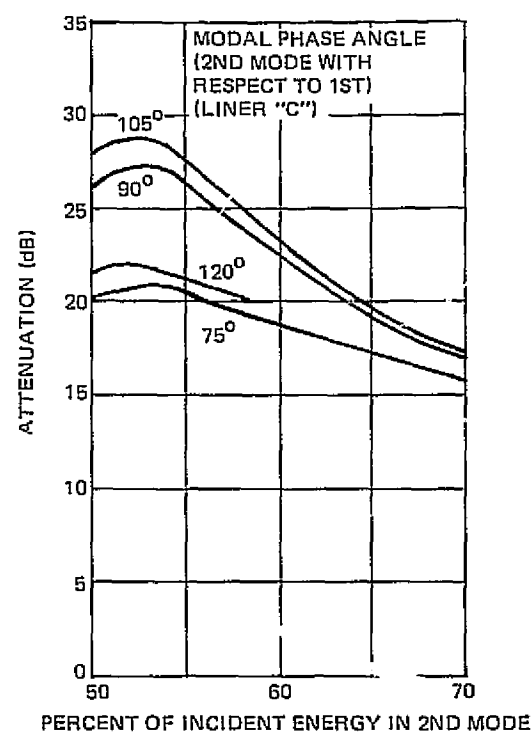
Figure 7. Performance of Aft Section of Two-Segment Liner as Function of
Equivalent Hard-Wall Modal Distribution of Incident Sound, M = 0.
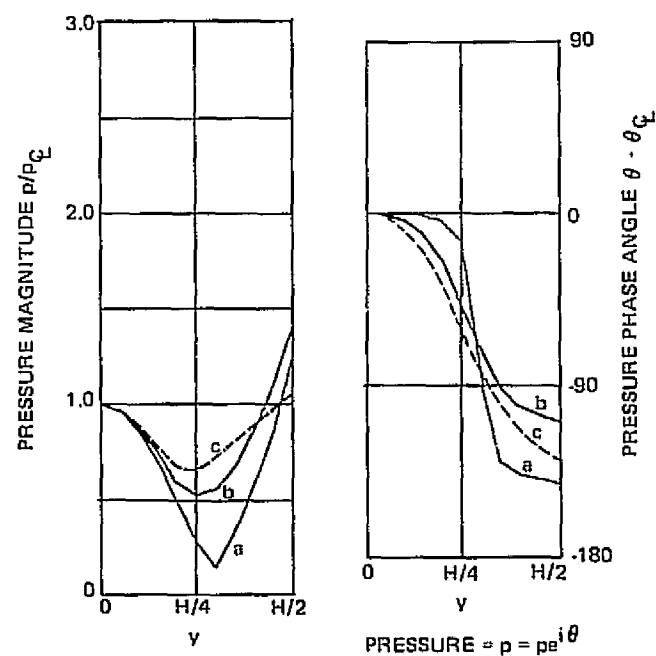
Figure 8. Transverse Distribution of Pressure at Entrance to Aft Duct
Segment for Duct Liner Configurations of Figure 5, M = 0.

15

Figures 8, 9 and 10 show the transverse pressure, axial velocity, and product of the pressure and the conjugate of the axial velocity, respectively, at the incident plane of the dissipative liner. These quantities, normalized with respect to their centerline values, are plotted in each figure for cases a, b and c. In going from configuration a to b, the optimization algorithm forced the acoustic field incident on the liner into a close approximation of the modal content for which the dissipative liner performs best.

Thus, the improved performance is seen to be due to redistribution of the modal content of the sound incident on the dissipative liner and not the result of reflection of acoustic energy. (It should be pointed out, however, that the method of operation of the low resistance front liner appears to be through interaction of right and left moving wave systems; thus, modal reflection in the reactive liner is a key to the phenomenon but energy reflection from the reactive liner is not.) The modal redistribution mechanism has also been identified by Baumeister (ref. 35).

Table 2 contains optimum two-segment plane wave liners found by taking various initial guesses and constraining only the minimum resistance of the front liner and total length. In each case, the final local optimum configuration obtained had a low front liner resistance, even though the initial iteration was begun with substantial resistance values. Similar trends have been found by Baumeister (ref. 35) and by Quinn (ref. 36) in their investigations. This is gratifying in view of the significant differences between their finite difference models and this modal expansion model. (The finite difference model involves a finite segmented liner bounded on the incident side by a semi-infinite continuation of the initial liner, and on the transmitting side by a ρc termination, while the present eigenfunction expansion model uses hard-wall terminating ducts on both sides of the lined segments.) However, it is important to note that, because of the model difference, these optimum configurations will have different impedances and different attenuations for the liner configurations in which reactive elements are found. (These configurations include not only the two-segment liner, but also the single-segment liners for those cases for which reactive effects are important.) The most significant effect of the difference in models will be that, for example, an initial plane wave input may be distorted by higher order mode reflection in the model of this report, while the distribution will remain plane in the finite difference models since they do not account for the impedance discontinuity.

Figure 11 depicts the variation with frequency of optimum segment impedances and lengths for a two-segment plane wave liner, with $L/H = 3.0$ and zero Mach number. Specific acoustic resistance values were constrained to be greater than 0.048, but the variables were otherwise not restricted. The frequency range $6.0 < kH < 10.4$ is covered. For frequencies greater than $kH = 9.6$, the optimum front liner goes to minimum resistance. Maximum attainable sound power level attenuations decrease with increasing frequency. (Although not shown, they are well over 100 dB for frequencies below 3.0; they drop to 30 to 50 dB in the frequency region investigated.) These are definite improvements to be gained in the frequency range studied; by superimposing the single segment attenuations on the figure, it is seen that 10 to 15 dB may be achieved by using a two-segment configuration.

Also shown on Figure 11 is a curve of Cremer optimum impedance for the (0, 1) mode pair plotted versus reduced frequency. For a reduced frequency of kH near 10, the impedance of the dissipative liner, Z_2 approaches that of a Cremer liner. For this case, the front liner apparently converted the transverse acoustic field incident on the dissipative liner into a shape similar to the least attenuated mode. This behavior does not occur for reduced frequencies $kH < 10$, and an examination of Table 2 reveals that local two-segment optimums can be found for $kH = 10$ that do not approach a Cremer

16
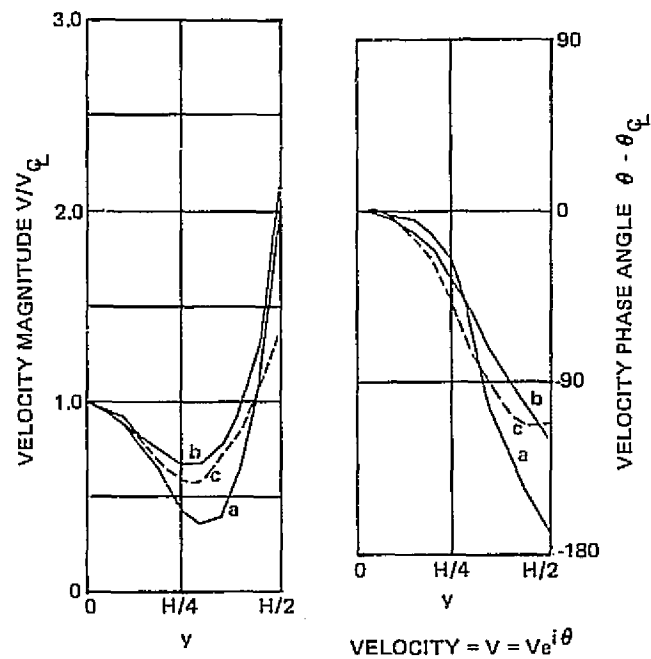
Figure 9. Transverse Distribution of Velocity at Entrance to Aft Duct Segment for Duct Liner Configurations of Figure 5, M = 0.
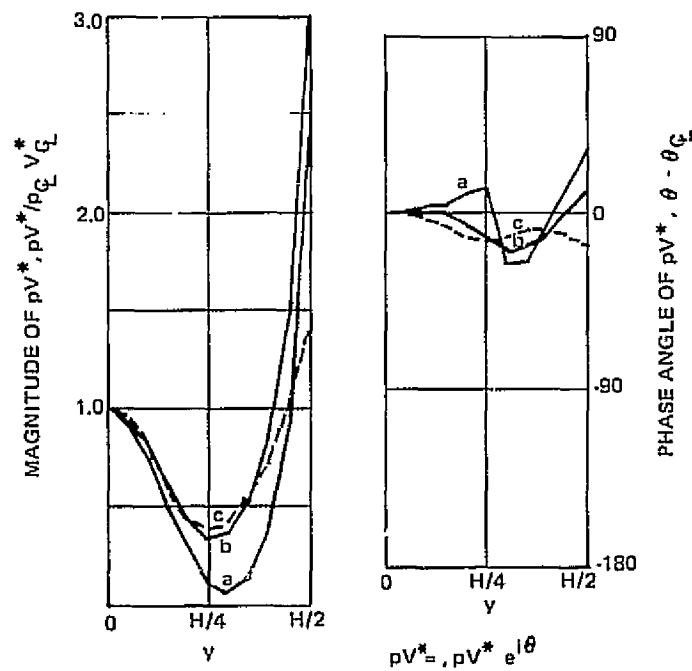
Figure 10. Transverse Distribution of Product of Pressure and Conjugate of Velocity for Duct Liner Configurations of Figure 5, M = 0.

TABLE 2
OPTIMUM TWO-SEGMENT LINING CONFIGURATIONS FOR PLANE WAVE, L/H = 3.0, η = 1.6, M = 0.

RUN IDENTIFICATION		INITIAL CONFIGURATION			FINAL CONFIGURATION		
		IMPEDANCE	LENGTH L/H	ATTENUATION	IMPEDANCE	LENGTH L/H	ATTENUATION
A	Liner 1 Liner 2	.079 - 1.40i 1.581 - 1.34i	.526 2.474	28.9	.048 - 1.75i 1.424 - 1.19i	.740 2.260	34.5
B	Liner 1 Liner 2	1.0 - 1.40i 1.581 - 1.34i	.526 2.474	15.5	.048 - 1.70i 1.440 - .84i	.841 2.159	40.8
C	Liner 1 Liner 2	2.0 - 1.40i 1.581 - 1.34i	.526 2.474	13.3	.048 - 1.77i 1.400 - 1.21i	.719 2.281	33.9
D	Liner 1 Liner 2	.079 - 1.40i 1.581 - .1i	.526 2.474	11.8	.048 - 1.52i 1.753 - .50i	.829 2 171	35.2
E	Liner 1 Liner 2	1.0 -1.40i 1.581 - .1i	.526 2.474	8.4	.048 - 1.67i 1.500 - .930i	.800 2.200	38.1

Figure 11. Attenuation, Segment Lengths and Impedance for Optimum 2-Segment Plane Wave Liner as Functions of Reduced Frequency. Total Liner Length = Three Duct Heights.

19

value for the dissipative liner impedance. Furthermore, variation of front liner reactance was found to be contrary to the results of Baumeister (ref. 36) which show that the reactance of the front liner should also approach the Cremer or least attenuated mode value.

Three-Segment Optimum Liners

The analytical studies which were conducted to select lining configurations for the experimental tests revealed that the attenuation performance of optimum two-segment lining configurations is sensitive to the modal content of the incident wave. Three-segment configurations were studied to determine whether an additional segment could reduce this sensitivity to modal content and also provide more attenuation than a single segment liner. In conducting the optimization studies, optimum single segment plane wave liners for the lengths $L_1/H = L_3/H = .5$ and $L_2/H = 2.0$ were used as initial values. Final configurations obtained by using these single segment optimums as initial values are shown in Table 3. Also shown are configurations that were obtained from other arbitrary starting values of liner impedance for a plane wave input. The optimization program located many local attenuation peaks that have nearly identical attenuations. Note that for the final configurations for cases A-E, the front liner has a high resistance. Only one case could be found for the three-segment optimization search which tended toward a low resistance front liner configuration. This is different from the trend observed in the case of the two-segment liners. However, the three-segment liner also appears to have "modal conditioning" as its operative mechanism for improved attenuation. Quinn (ref. 22) has obtained similar results; i.e., for his three-segment liners, there is no general tendency for the front liner to have low resistance. An exception is the case for $kH/2\pi = \eta = 1.0$ which is the cut-on frequency for the second mode. Baumeister (ref. 35) has found that for short liners (low L/H values) the front liner for both two- and three-segment optimum liners tend toward low resistance; his data, however, is for $\eta = 1.0$. As noted previously, the single segment liner also tends toward low resistance at $\eta = 1.0$. This repeated tendency is apparently due to the ease with which energy is transferred from the plane wave to the second mode. It thus appears that near $\eta = 1.0$ there is some reflection taking place in addition to modal redistribution.)

The final configuration of Case A in Table 3 was used as a starting point in a second optimization run. This run was made with different step sizes to determine whether the final configuration of Case A could be improved upon. As shown in Table 4, a new three-segment plane wave liner was found which out performed the Case A liner. Optimum configurations for other modal input values are also shown.

Table 3 shows that when segment lengths were allowed to vary, several local optimums were found. The specific optimized liner parameters, liner lengths and impedances, depended on starting values and step sizes used in the search. A distinct global optimum configuration could be found only when the segment lengths were held constant. While these local optimum configurations have nearly identical total attenuation at the design frequency, they have different sensitivities to incident modal content and different frequency bandwidth characteristics. Because of these properties, it may be possible to design a multisegment optimum lining to be relative insensitive to both the modal structure of the acoustic field and the tolerances of panel materials.

TABLE 3
LOCAL OPTIMUM THREE-SEGMENT LINING CONFIGURATIONS FOR PLANE WAVE, M = 0.

RUN IDENTIFICATION		INITIAL CONFIGURATION			FINAL CONFIGURATION		
		IMPEDANCE	LENGTH L/H	ATTENUATION	IMPEDANCE	LENGTH L/H	ATTENUATION
A	Liner 1	.35 - .85i	0.5		.917 - .981i	.470	
	Liner 2	.87 - 1.77i	2.0		1.579 - 2.205i	1.959	
	Liner 3	.35 - .85i	0.5	9.97	.601 - .497i	.571	50.4
B	Liner 1	2.0 - .85i	0.5		1.957 - .911i	.516	
	Liner 2	.87 - 1.77i	2.0		1.371 - 2.265i	1.954	
	Liner 3	.35 - .85i	0.5	12.4	.594 - .514i	.530	50.9
C	Liner 1	.35 - .85i	0.5		.406 - .893i	.479	
	Liner 2	2.0 - 1.77i	2.0		1.764 - 1.588i	2.941	
	Liner 3	.35 - .85i	0.5	21.5	.534 - .559i	.580	52.5
D	Liner 1	.35 - .85i	0.5		.804 - 1.228i	.368	
	Liner 2	.87 - 1.77i	2.0		1.492 - 2.110i	1.940	
	Liner 3	.05 - .85i	0.5	8.8	.703 - 534i	.692	52.6
E	Liner 1	.35 - .1i	0.5		.571 - .513i	.503	
	Liner 2	.87 - 1.77i	2.0		1.787 - 2.467i	1.946	
	Liner 3	.35 - .85i	0.5	9.4	.635 - .514i	.551	50.9
F	Liner 1	.35 - .85i	0.5		.048 - 1.419i	.728	
	Liner 2	.87 - .1i	2.0		1.869 - .744i	1.980	
	Liner 3	.35 - .85i	0.5	7.0	.501 - .852i	.292	36.6

TABLE 4
OPTIMUM THREE-SEGMENT LINING CONFIGURATIONS, M = 0

	AMPLITUDE OF FIRST MODE	AMPLITUDE OF SECOND MODE	SPECIFIC IMPEDANCE	SEGMENT LENGTH L/H	TOTAL ATTENUATION
PLANE WAVE	1.0 + 0.0i	0.0 + 0.0i	.982 - .977i 1.571 - 2.203i .613 - .503i	.465 1.951 .584	52.7
EQUAL AMPLITUDE	1.0 + 0.0i	1.0 + 0.0i	.997 - .932i 1.833 - 2.278i .641 - .520i	.463 1.944 .594	53.1
LARGE SECOND MODE CONTENT	1.0 + 0.0i	5.0 + 0.0i	.866 - .730i 1.986 - 2.375i .588 - .522i	.536 1.969 .495	56.2
EQUAL ENERGY	1.0 + 0.0	1.6034 + 0.0i	.970 - .895i 1.907 - 2.316i .643 - .493i	.484 1.943 .573	52.8
EQUAL ENERGY 90° OUT OF PHASE	1.0 + 0.01	0.0 + 1.6034i	1.407 - 2.265i 1.471 - .981i .981 - .630i	.491 1.972 .537	52.0

EXPERIMENTAL PROGRAM

Description of Test Facilities

In the design and subsequent testing of the single and multiple segment lining configurations two separate facilities of the acoustic laboratory were utilized. The flow resistance properties of facing sheet material were determined in the flow resistance test facility. From the results of these tests, facing sheet material was selected for fabrication of the six test panel configurations. The panels were then tested in the grazing flow duct facility which provides acoustic data for lining configurations in controlled acoustic and flow environmental conditions.

Flow Resistance Test Facility

The specific flow resistance test bench, shown on Figure 12, was designed to provide a reliable method of determining the steady-state flow resistance of acoustic panel facing sheet materials. The components of the specific flow resistance test bench include a device for control of airflow, an instrument for measurement of airflow rate, a sealed air duct of known area capable of forcing the air through the area of material tested, and an instrument for determining the difference in air pressure between the upstream and downstream sides of the material. Output from this instrumentation is input to the VARIAN 620L computer which determines values of flow resistance in cgs Rayls and calculated values of particle velocity for specified flow rates.

The accuracy of measurements is estimated to be 5 percent of the measured value in cgs Rayls. This estimate is based on the summation of inaccuracies of measuring instrumentation and of effective cross-sectional area of the specimen tested. Repeatability is within 2 percent of the determined cgs Rayl value.

Grazing Flow Duct Test Facility

The grazing flow acoustic impedance test device, schematically shown on Figure 13, consists of an air plenum, a sound source, test section, and an aerodynamic/acoustic diffuser. With this device, acoustic sound pressure level (SPL) and phase data are measured as a function of distance along the test section lining length for a selected combination of excitation SPL and frequency and air flow rate.

The air plenum consists of a 121.9-cm (48-inch) diameter cylindrical steel shell lined with acoustic insulation to minimize airflow noise. The sound source is provided by an electropneumatic sound generator (Figure 14). This generator is coupled to the test section by a fiberglass exponential horn (Figure 15) that provides a transition from the circular cross-sectional geometry of the driver to the square test section. Sinusoidal noise levels were measured in the test section for frequencies up to 6000 Hz. These measurements indicate that the sound generator is capable of producing 130 dB for Mach numbers up to 0.4. The test section has a 5-cm (2-inch) square cross section with a bellmouth input from the plenum (Figure 15). The top of the test section (Figure 16) can accommodate either a hard-walled plate or an acoustic liner. The opposite wall has two flush mounted microphones, one fixed at the start of the test section and the other on a traversing device (see Figure 17) that moves along the 40.6-cm (16-inch) length of the test section. The bottom and side walls of the test section are rigid and acoustically hard. Consequently, the test configuration may be modeled as a symmetric duct with total height, H = 10.2-cm (4-inch). Axial flush mounted microphone measurements thus correspond to analytical predictions of symmetric duct centerline pressures.

SILICONE RUBBER ADAPTER
FOR TEST SAMPLE

SUPPORT TABLE FOR
TEST SAMPLE

AIR SUPPLY

Figure 12.   Steady-State Flow Resistance Test Bench
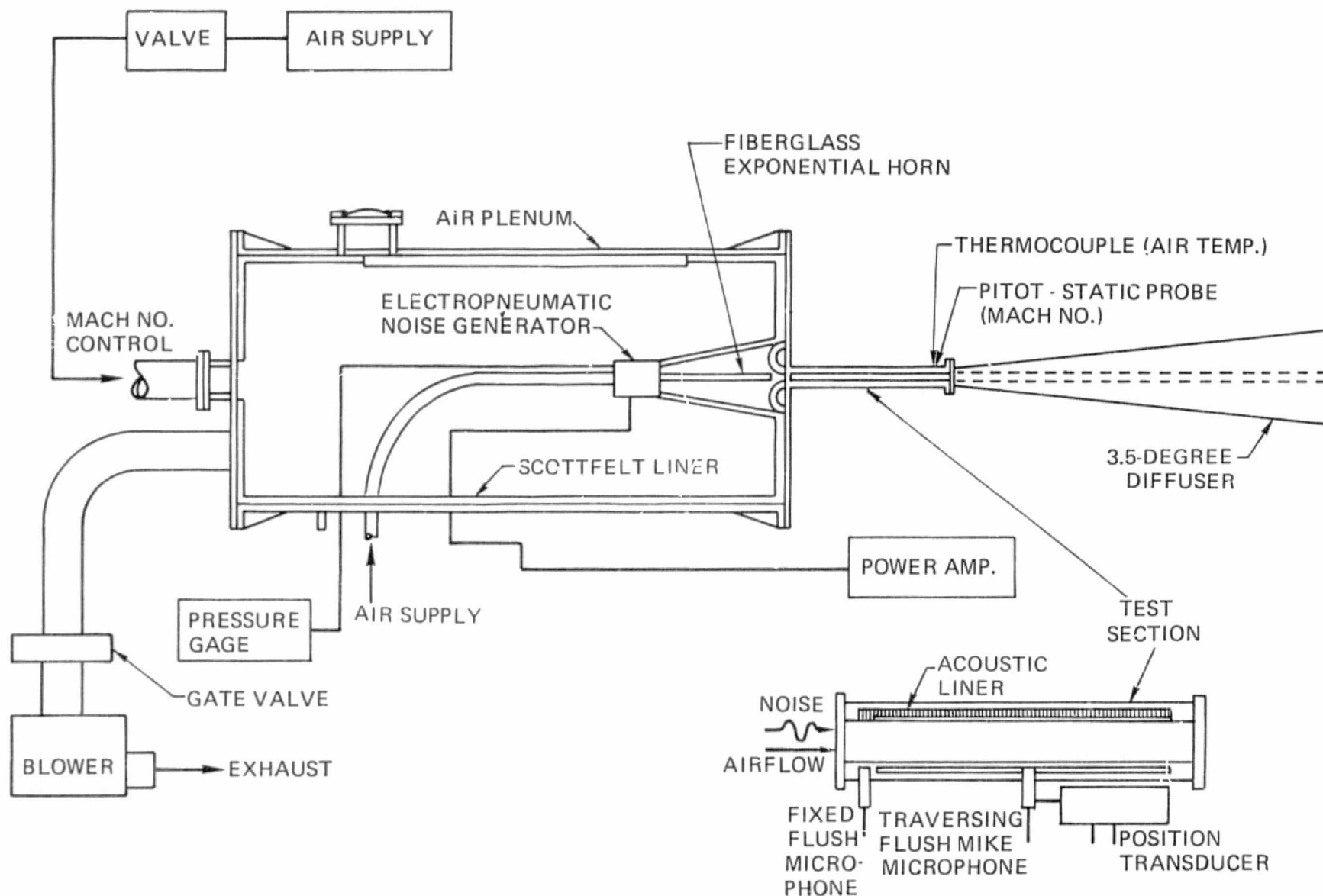
Figure 13. Schematic Diagram of Grazing Flow Duct Test Facility
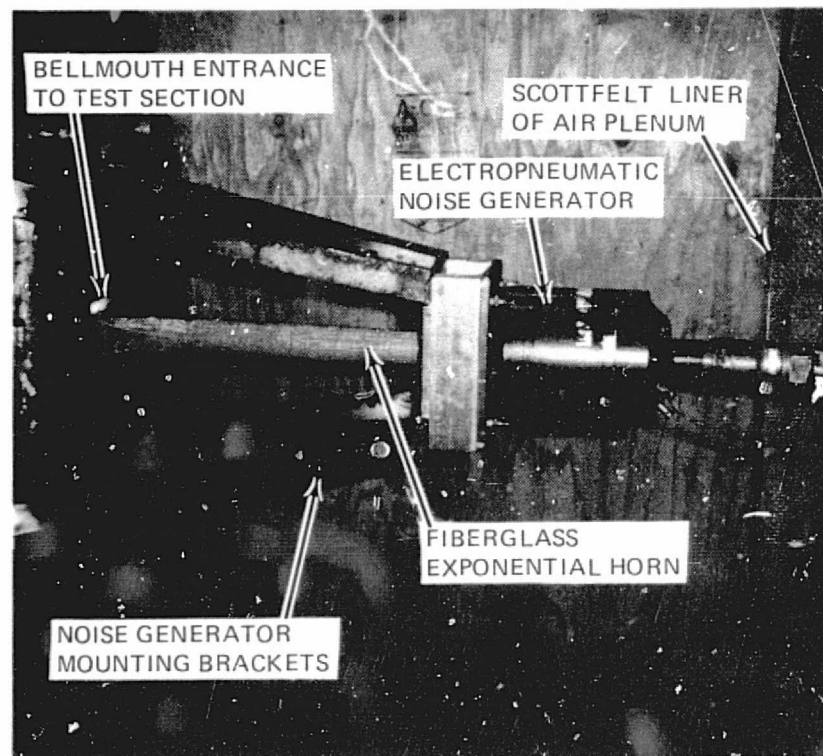
Figure 14. Installation of the Electropneumatic Sound Generator
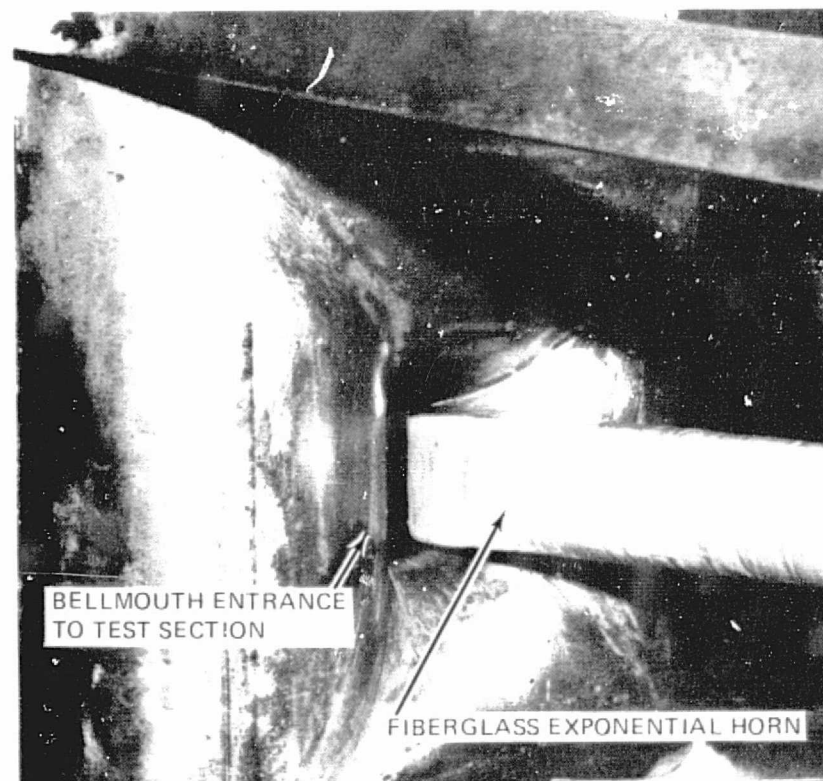
Figure 15. Coupling of the Exponential Horn and Test Section
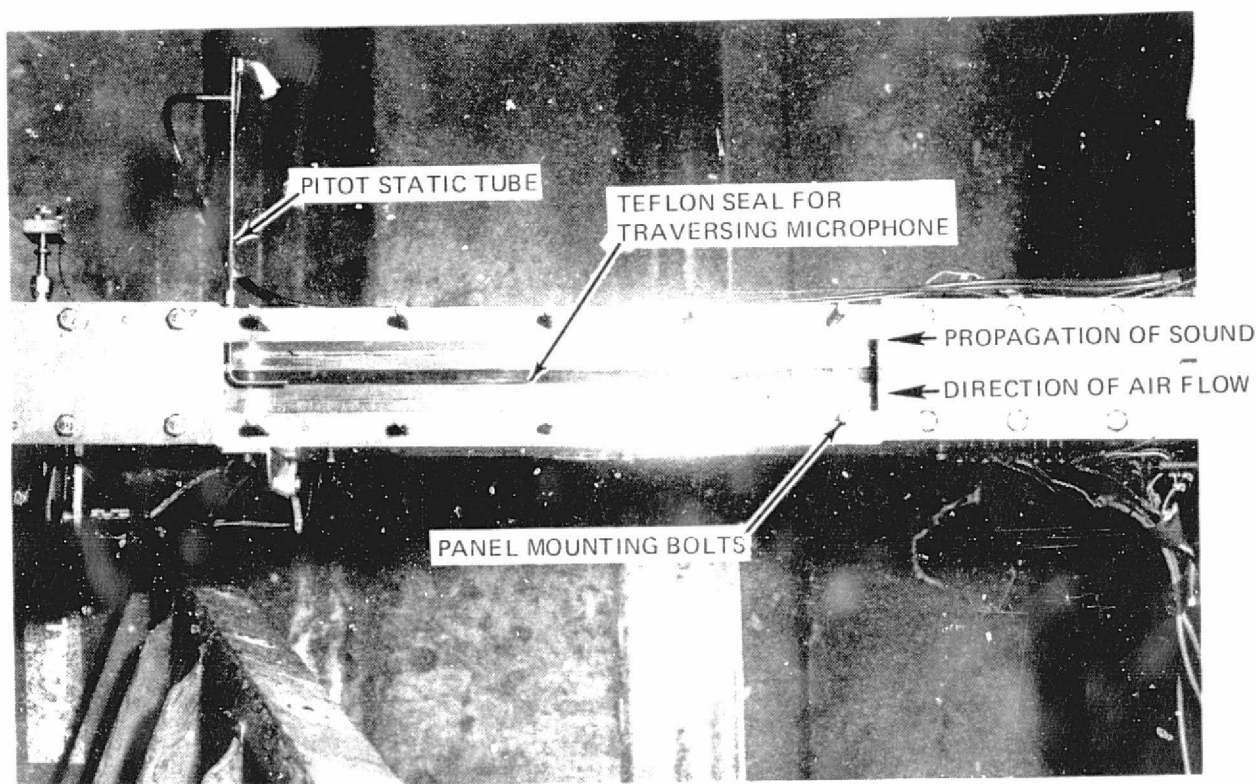
Figure 16. Plan View of Test Section
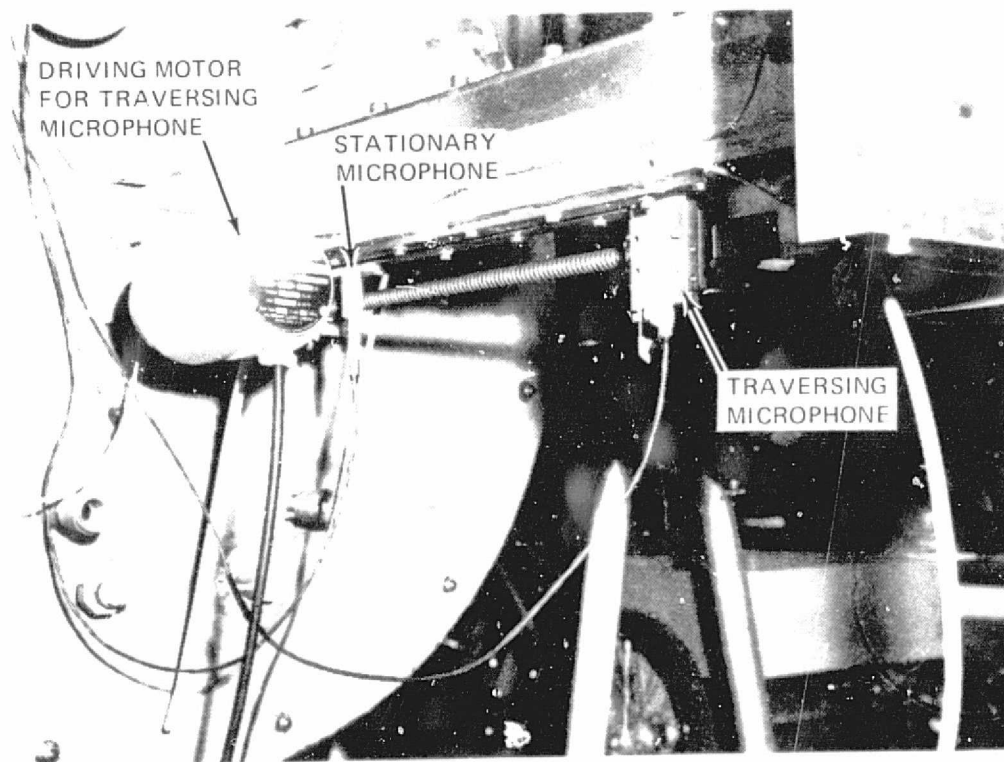
Figure 17. Reference and Traversing Microphones

An aerodynamic/acoustic diffuser (Figure 18) is attached to the end of the test section. This diffuser with a 3.5-degree diverging angle is designed to allow expansion of the flow field without separation. Geometrically, the 5- by 5-cm (2- by 2-inch) cross section expands to a 5- x 34.9-cm (2- x 13.75-inch) cross section. The sidewalls are lined with a 50 percent open area perforated sheet. The backing space which varies linearly from 0 to 15.2 cm (6 inches) is filled with a bulk material acoustic absorber to minimize reflections from the diffuser and provide an anechoic termination.

A picture of the test operation console is shown on Figure 19. From this console, the acoustic and flow environment of the test section are controlled and acoustic and boundary layer data are acquired and displayed. The spectral definition, power level, and excitation frequency of the excitation system output are controlled by the monitor and control network. The Mach number of the test section is regulated by controlling the static pressure of the plenum.

<center>Design of Test Panel Configurations</center>

Lining Configurations

In defining the test panel configurations, it was necessary to design multisegment lining configurations which would out-perform single segment linings both for the plane wave and for other modal combinations. This behavior was important to the demonstration of the phased lining concept since the modal content of the acoustic environment in the grazing flow duct cannot be controlled.

The six test panel configurations are identified and their design conditions specified in Table 5. Configurations 1-3 and configurations 4-6 are designed for flow velocities of M = 0.0 and M = 0.4, respectively. Configuration 1, a uniform liner, is the single-segment optimum for L/H = 3, and a plane wave input for a reduced frequency of kH = 10. For this frequency, (approximately 5K Hz in the test section of the grazing flow duct), it is shown on Figure 4 that a low resistance liner placed in front of a dissipative liner altered the modal content of sound incident on the dissipative liner, thereby making the dissipative liner more effective. This two-segment liner, configuration 3, also was selected for the test program. As previously shown, this configuration was a constrained optimum; relaxation of the constraints allowed more attenuation to be obtained by subsequent two-segment designs. This liner was chosen over the others since a very detailed study of its performance had been made. Design parameters for this configuration were determined for M = 0 by solving equation (23) for facing sheet resistance and backing depth. These parameters are also given in Table 5.

Since the modal content of the grazing flow duct acoustic field was not known at the design frequency, the performance of this two-segment liner was calculated for various combinations of the first and second modes. The variation with frequency of the attenuation performance of this lining configuration was calculated for M = 0.0 by the multisegment duct analysis program.

Figure 20 depicts the attenuation performance of the two-segment liner. Attenuations for four modal combinations are plotted versus excitation reduced frequency, kH. The two-segment liner is quite sensitive to the modal content of the sound. The attenuation performances of the single-segment optimum lining for a length of 30.5 cm (12 inches) (L/H = 3) are also plotted on this figure for the same modal combinations. The two-segment liner yields more attenuation than the uniform liner only for the case when the plane wave is the only mode present. If there is any significant second mode component present in the source field, configuration 3 will not generally outperform the single segment liner.

<center>28</center>

PERFORATED PLATE
FACING SHEET MATERIAL

3.5° DIVERGING ANGLE
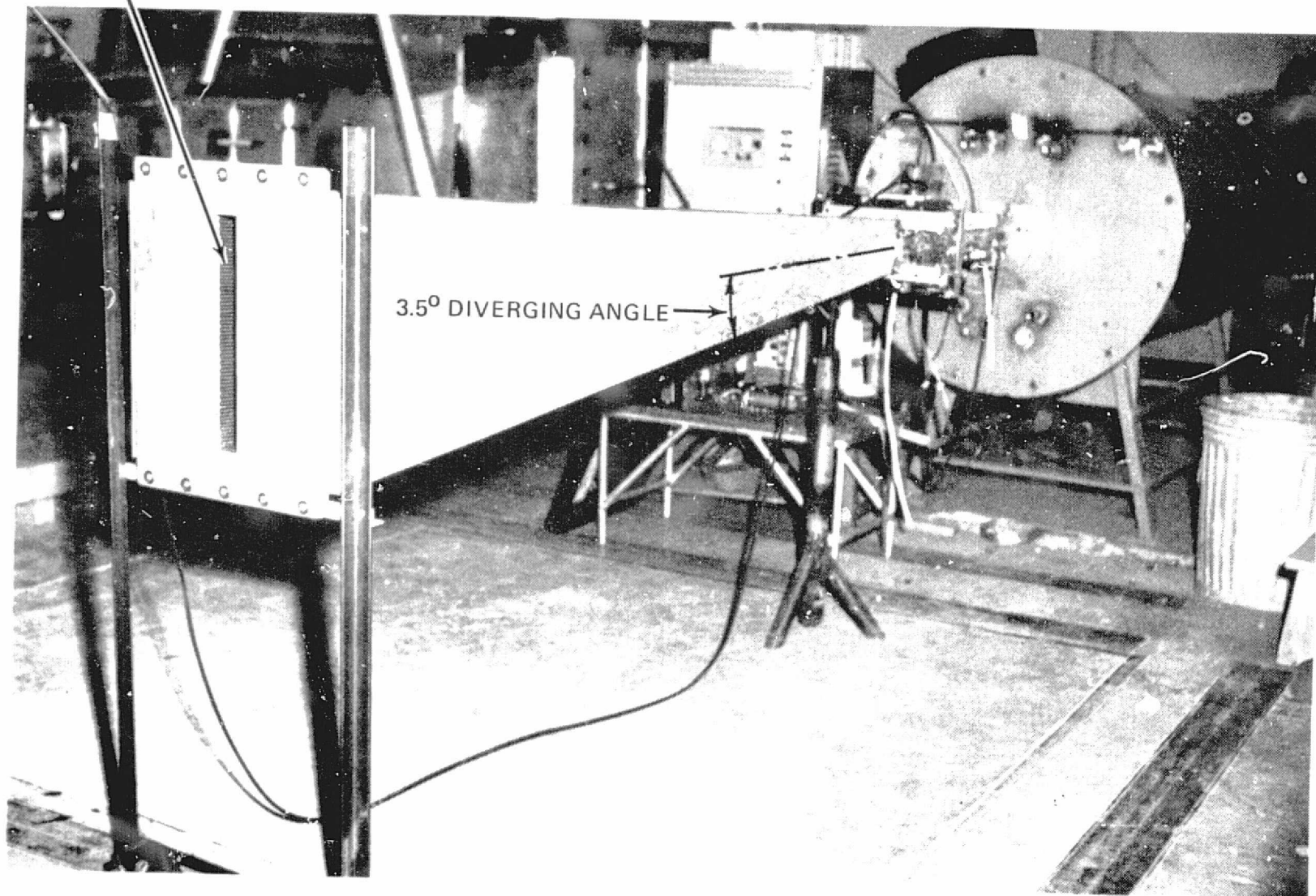
Figure 18:   Aerodynamic/Acoustic Diffuser

29

ANALOG PLOTTER FOR
ACOUSTIC DATA DISPLAY
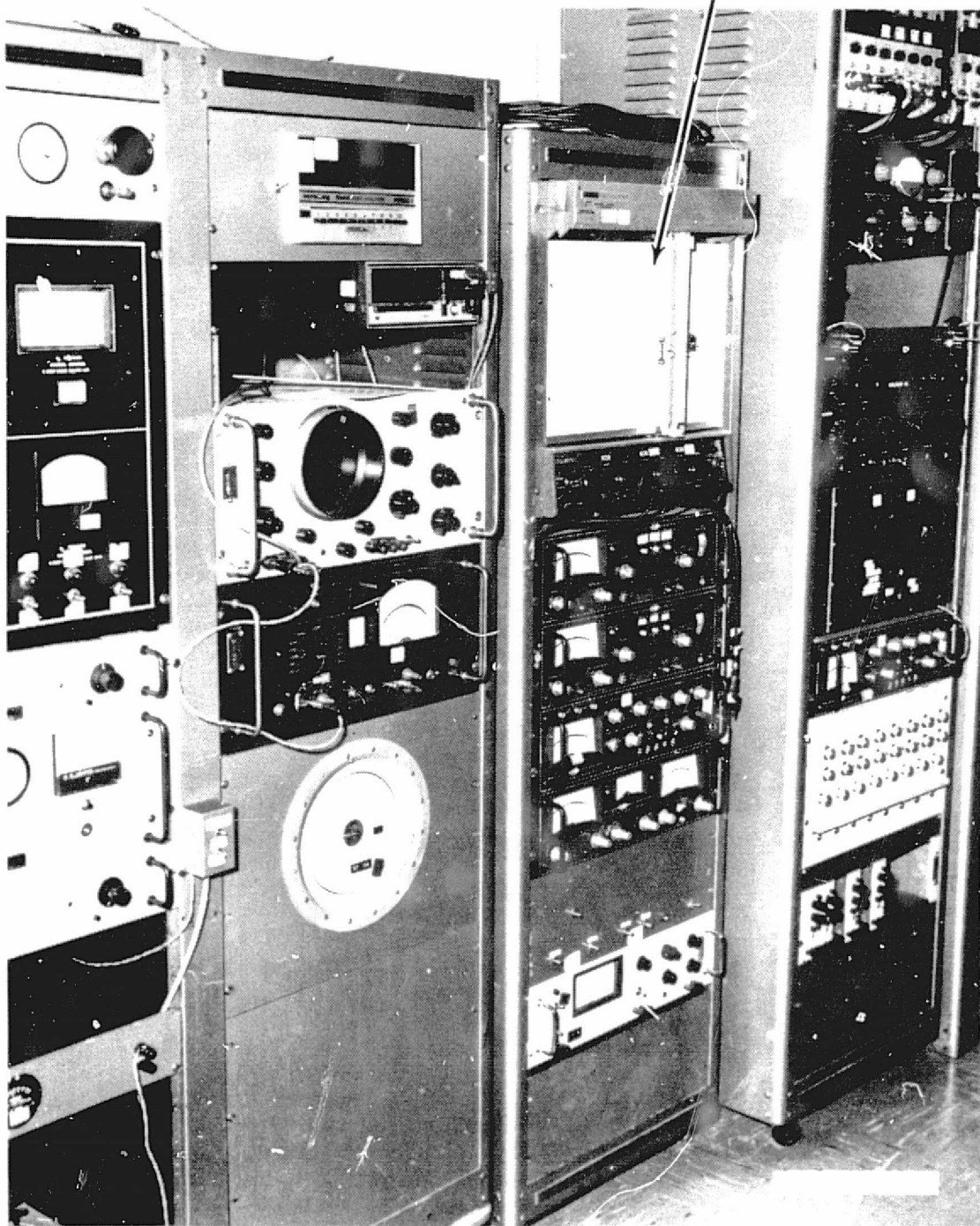
Figure 19. Test Operations Console for Grazing Flow Duct Facility

TABLE 5
TEST PANEL CONFIGURATIONS

CONFIG-URATION I.D.	DESIGN CONDITION		PANEL I.D.	PANEL LENGTH		PANEL		FACING SHEET FLOW RESISTANCE			BACKING DEPTH	
	kH	M		cm	in	SPECIFIC IMPEDANCE	RESISTANCE* Re PANELS	SHEET I.D.	SAMPLE NO.	Re** RAYLS	cm	in
1	10.0	0.0	FO-1	30.5	12.0	1.30 — 1.85i	46	8	1&3	45	0.41	0.16
2	10.0	0.0	DF-1	4.8	1.88	.977 — .981i	35	7	4&6	41	0.66	0.26
			DF-2	19.9	7.84	1.58 — 2.21i	56	9	3&5	55	0.36	0.14
			DF-3	5.8	2.28	.601 — .497i	21	5	1&2	22	0.97	0.38
3	10.0	0.0	RF-1	5.3	2.10	.079 — 1.40i	3	1	6	2	0.61	0.24
			DF-4	25.1	9.90	1.581 — 1.34i	56	9	4&6	55	0.48	0.19
4	10.0	0.4	FO-1F	30.5	12.0	.663 — .994i	24	6	5&6	23	0.71	0.28
5	10.0	0.4	RF-1F	5.6	2.22	.048 — .674i	2	1	5	2	0.99	0.39
			DF-4F	24.8	9.78	.852 — .763i	30	6	2	30	0.76	0.30
6	10.0	0.4	DF-1F	5.3	2.07	.619 — 0.454i	22	5	6	23	0.99	0.37
			DF-2F	20.3	7.99	.809 — 1.12i	29	6	1	27	0.64	0.25
			DF-3F	5.0	1.94	.433 — .202i	15	4	2	22	1.27	0.50

*RESISTANCE VALUES BASED ON $\rho c = 39.5$ cgs RAYLS AND REDUCED BY 10 PERCENT TO ACCOUNT FOR CORE AND ADHESIVE BLOCKAGE
**ESTIMATED VALUES BASED ON FLOW RESISTANCE DATA
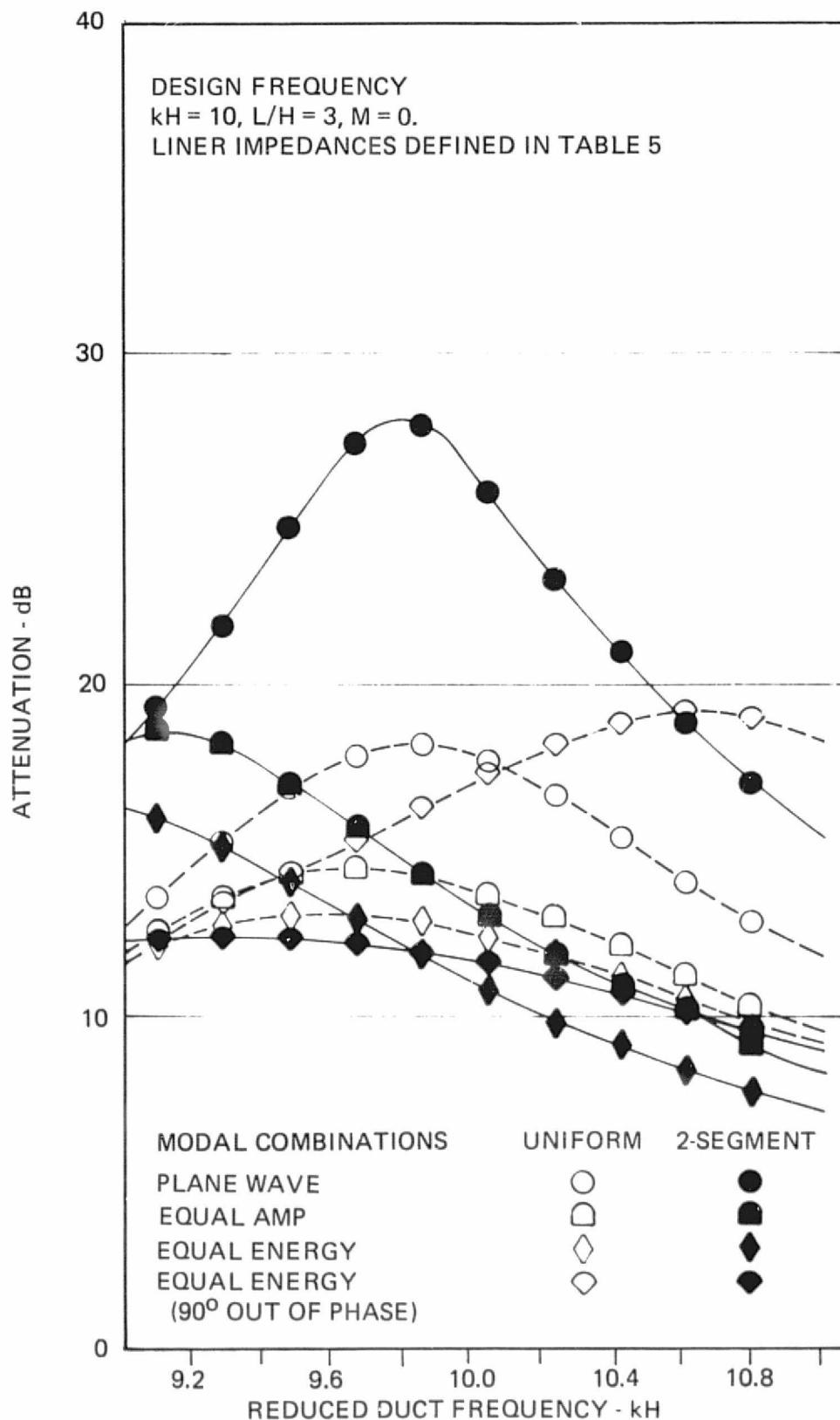
Figure 20. Sound Power Level Attenuation Performance of Configuration 1 and Three Liners as Function of Modal Input and Frequency for M = 0.

32

Obviously, there was a risk of not demonstrating the phased lining concept if the modally sensitive two-segment liner were to fail to outperform the single-segment liner due to the presence of the second mode in the grazing flow duct. Consequently, the search was continued for a multisegment liner that would meet the test objective and would be less sensitive to modal content. A three-segment configuration was studied to determine whether the additional segment could reduce this sensitivity. In conducting the optimization studies, optimum single-segment liners for the lengths $L_1/H = L_3/H = .5$ and $L_2/H = 2.0$, and M = 0 were used as initial values.

Figure 21 summarizes the attenuation performance of a three-segment configuration as compared with the single-segment optimum. A detailed investigation was conducted to determine the mechanism by which the three-segment liner was able to outperform the uniform liner for all four modal combinations over the entire frequency range under study. Attenuations for each liner segment were calculated for each incident modal combination. For a plane wave input, the attenuations of liners 1 and 2 were nearly the same as their optimum single segment attenuation values. The attenuation of the third liner is nearly ten times the single segment value of 2.2 dB. Thus, in this case, the first two liners accounted for only 5 percent and 29 percent of the total attenuation, respectively, but they apparently altered the modal content such that the third dissipative liner performed more efficiently (66 percent). Similar behavior can be noted for the case with both the first two modes incident at equal pressure amplitudes and equal energies, respectively. For these cases, liner 3 accounted for at least 60 percent of the total attenuation. For the case with the second mode 90 degrees out of phase with the first (equal energy in both modes), the second liner accounted for 53 percent of the total attenuation. It appears that the reason this liner performs so well for the various modal inputs is that the function each segment performs, either conditioning the modal content or attenuating the principal portion of the sound, depends on modal content; the segments change roles for different modal inputs. This three-segment liner which was found to perform better than the optimum single-segment liner for the plane wave and for other selected combinations of duct modes was chosen to be the last M = 0 test configuration.

Configurations 4 through 6 were designed by using the optimization program in conjunction with the uniform mean flow theory. Plane wave optimum multisegment lining configurations were determined by using optimum single-segment liners for M = 0.4 as initial values. Final parameter values are presented in Table 8. Some of these impedance values are closely approximated by applying the $\frac{1}{(1 + M)^2}$ factor (ref. 33) to the impedance values of configurations 1 through 3.

The total length of each panel configuration was 30.48 cm (12.0 inches). Since the moving microphone traverses 40.0 cm (15.75 inches), the pressure field can be measured beyond the boundaries of the acoustic liners. Configurations 1 through 3 were fabricated with a hard-wall section, 10.16 cm (4 inches) in length, in front of the linings to provide measured data across the initial hard-wall/soft-wall interface. This arrangement was modified for configurations 4 through 6. Hard-walled sections, 5.08 cm (2.0 inches) long, were placed in front of and behind the linings to provide measured data across both the initial and final hard-wall/soft-wall interfaces. Schematic diagrams illustrating the location of the lining configurations and giving the identification number for each liner are shown on Figures 22 and 23. Liner segment lengths are presented in Table 5.

Panel Construction

The test panels are of conventional sandwich type construction. Arrays of normally reacting Helmholtz resonators are provided by small cavities sandwiched between a porous face sheet and impervious backing.
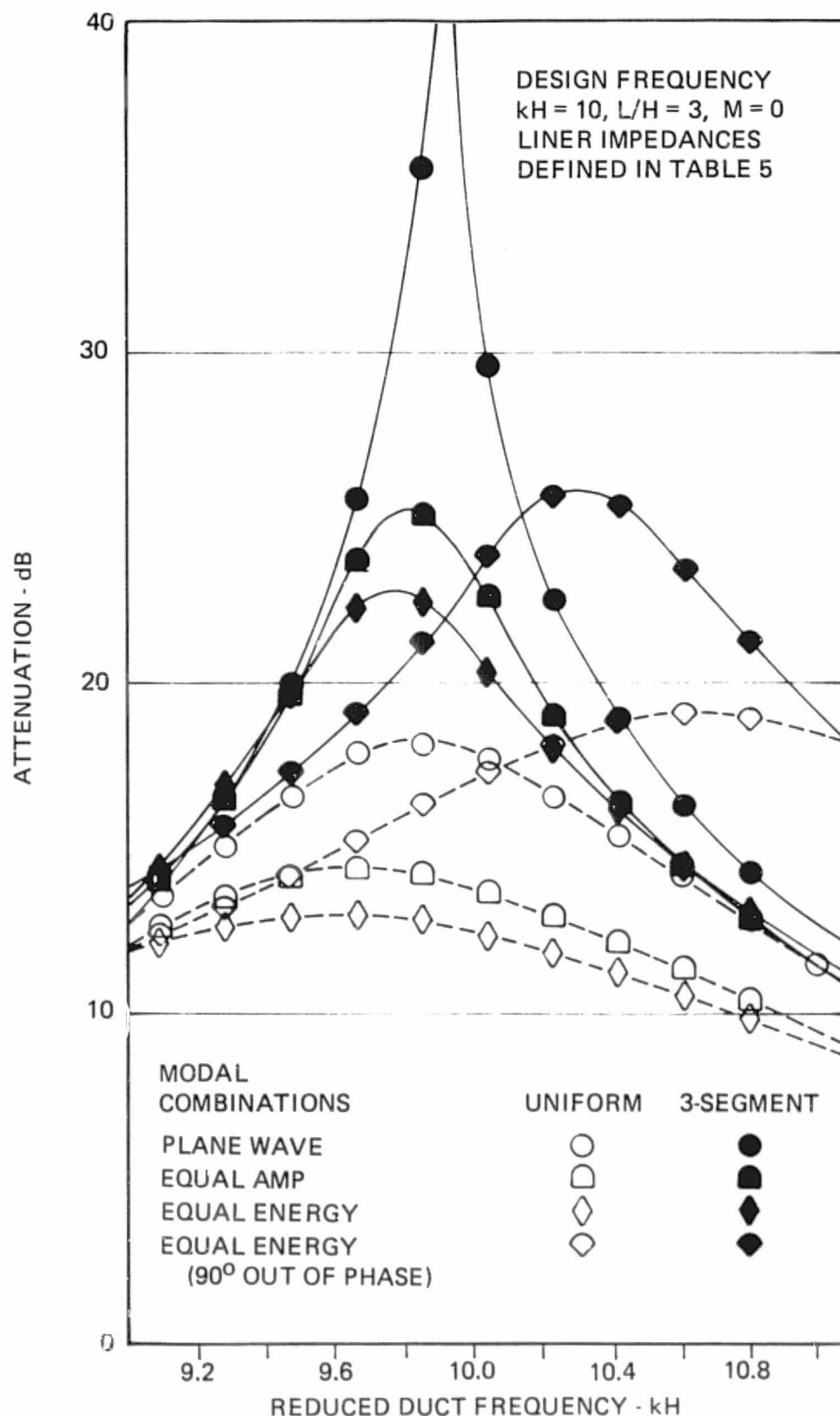
Figure 21. Sound Power Level Attenuation Performance of Configuration 1 and Two Liners as Functions of Modal Input and Frequency for M = 0.
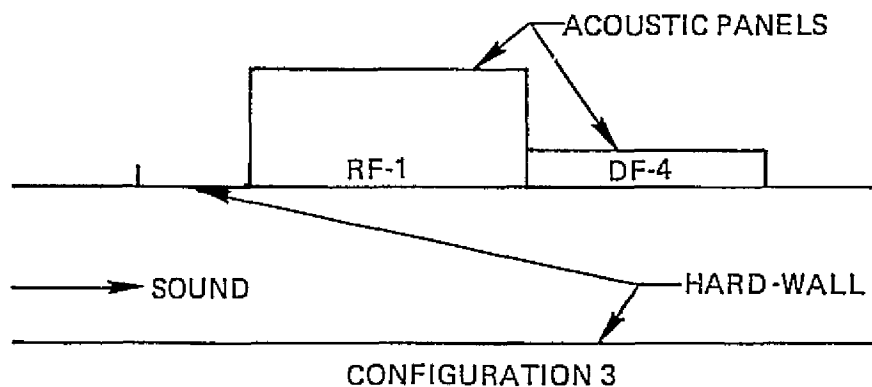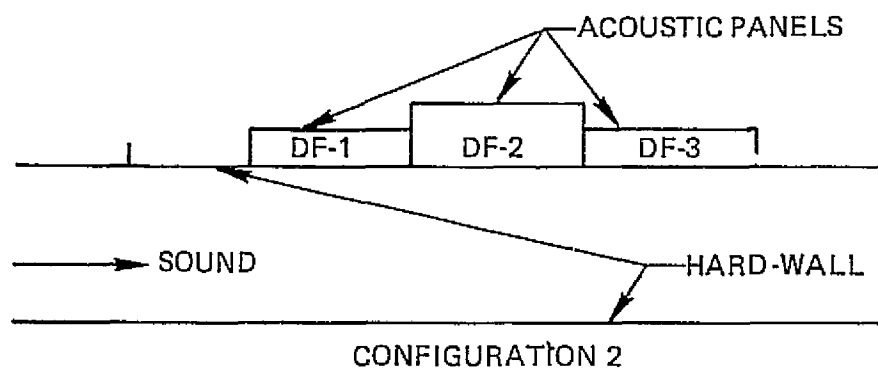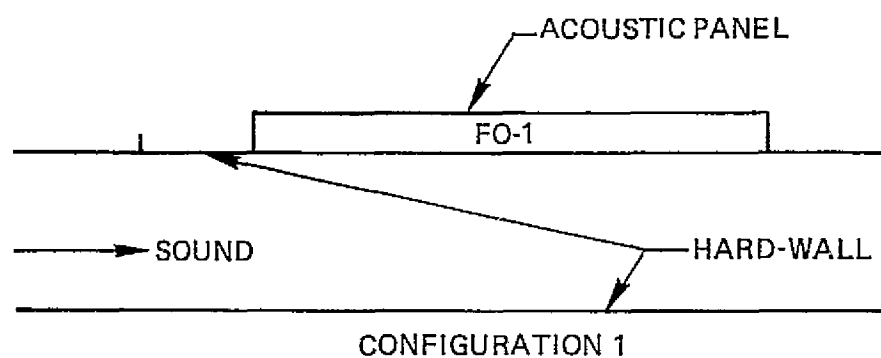
34

Figure 22. Schematic Diagram of Test Panel Configurations Defined in Table 5 for M = 0.
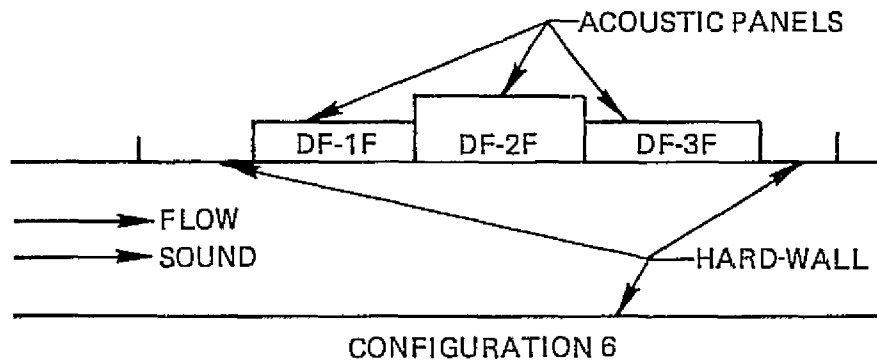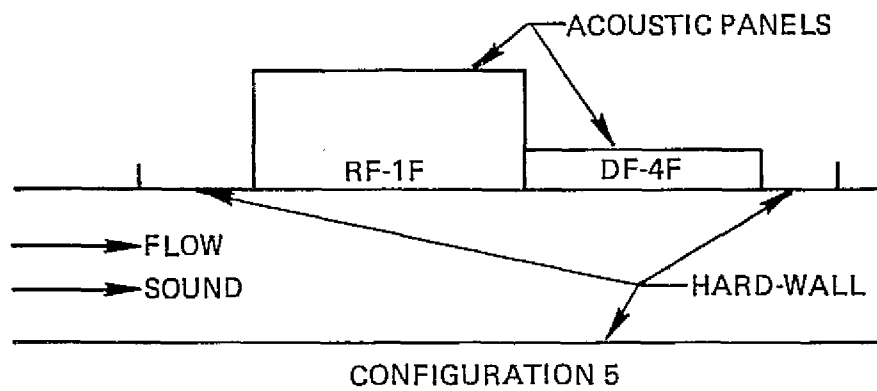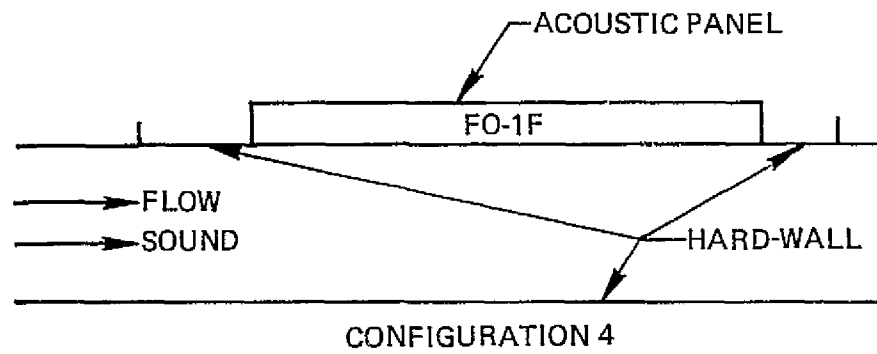
Figure 23. Schematic Diagram of Test Panel Configurations Defined in Table 5 For M = 0.4.

A fiber metal type of facing sheet was chosen because its flow resistance properties are relatively independent of frequency and induced particle velocity. The material used, Brunscoustic plate, consists of a stainless steel Brunsmet web that is sinter bonded to a .051-cm (.020-inch) thick stainless steel perforated sheet with a 32 percent open area. All test panels were fabricated from existing stock of 25.4-cm (10-inch) by 61-cm (24-inch) Brunscoustic plate. The resonator cavities were fabricated from phenolic honeycomb with a .953-cm (3/8-inch) cell size. This core material was bonded to the facing sheet with a nonflowing roll-on adhesive to minimize adhesive fillet blockage of the Brunscoustic plate.

Selection of Panel Facing Sheets

To obtain the required flow resistance characteristics, the specific resistance of each panel had to be converted into a criterion for the selection of facing sheet material. Panel resistance was calculated by multiplying the specific resistance by the value of characteristic impedance of air (39.5 cgs Rayls). This value was adjusted to account for the blockage (estimated to be 10 percent) of the core and bonding adhesive. This value was used to select the facing sheet material for panel fabrication.

Figure 24 depicts steady-state flow resistance data for a typical facing sheet material. Steady-state flow resistance values in cgs Rayls are plotted against calculated values of particle velocity. This data illustrates the linear behavior of the fiber metal. The small slope of the flow resistance versus particle velocity curve allows grazing flow effects to be neglected. Liner impedances are assumed to be independent of Mach number. The approximate location of the test areas and the approximate locations of the areas that were used for panel fabrication are shown. Each of the other six sheets was tested to provide an estimate of its flow resistance properties. Required values of flow resistance and the corresponding measured values for the panel liners are given in Table 5. Figures 25 and 26 are photographs of the fabricated lining configurations.

Calculation of Panel Backing Depth

The backing depth of the resonator cores were explicitly determined from the crossover frequency impedance model

$$\frac{Z}{\rho c} = \frac{R_e}{\rho c} + i \frac{R_e (kH)}{\rho c F_c H} - i \cot \left[(kH)(d/H) \right] \tag{23}$$

in terms of the face sheet resistance, R_e, characteristic impedance of air ρc and crossover frequency (frequency at which the face sheet reactance equals its resistance) of $F_c = 2\pi f_c / c$. Unpublished impedance tube test data for fiber metal facing sheet materials showed that the reactance of the facing sheet varies linearly with frequency. This behavior validates the use of the crossover frequency model. Based on these data, a value of crossover frequency $f_c = 15,000$ Hz was used in this investigation as a representative value for the Brunscoustic face sheet.

Analysis of Test Data

The objective of the test program was to experimentally verify the analytical techniques developed to predict liner performance. Duct centerline rms pressure magnitude and phase were calculated

37
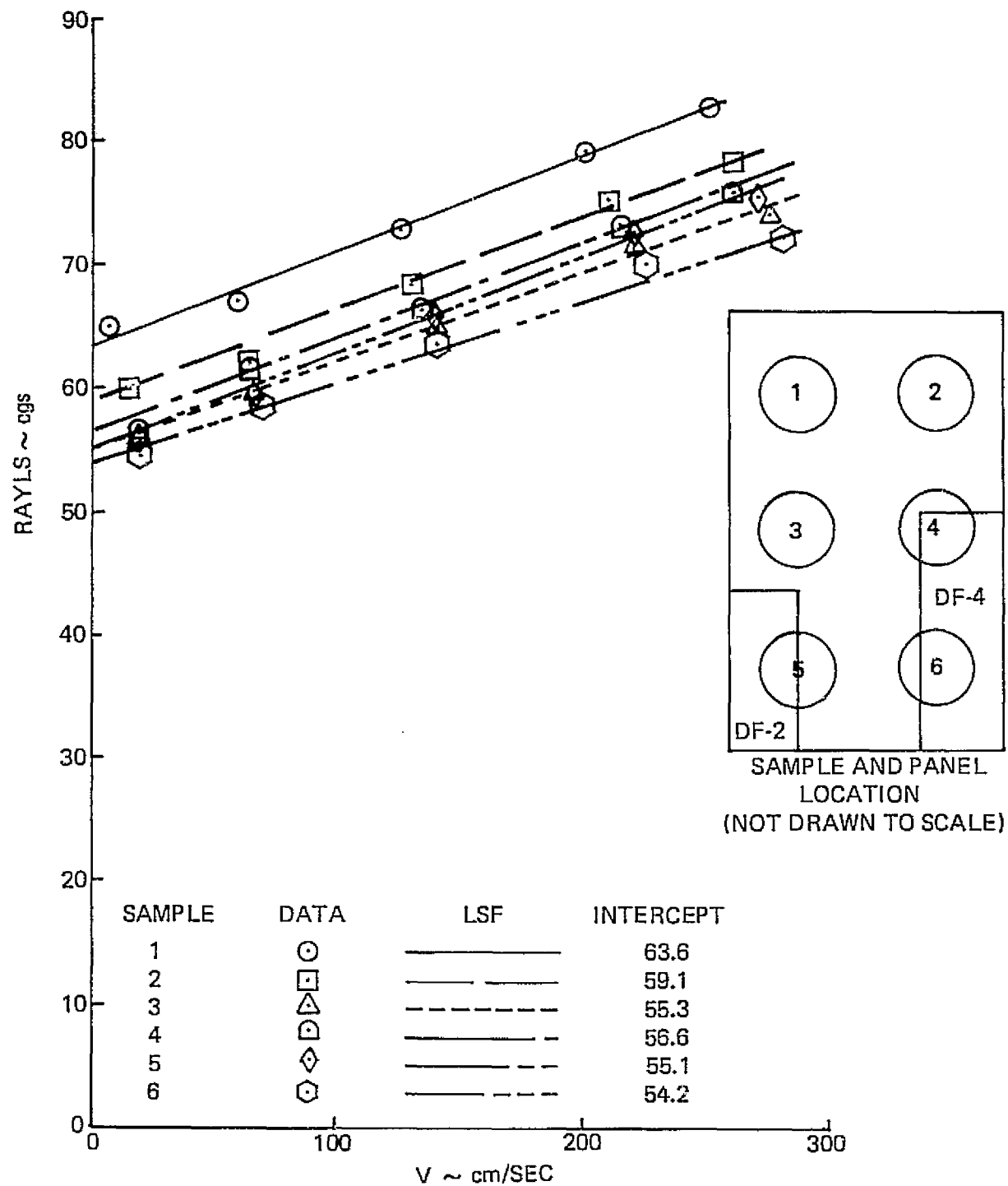
Figure 24. Typical Bench Test Steady-State Flow Resistance Data
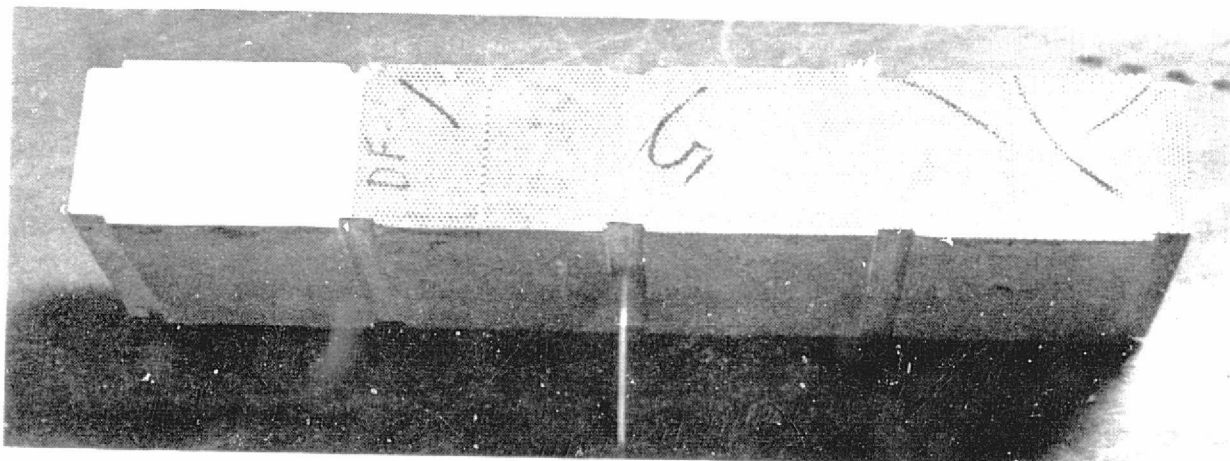
CONFIGURATION 1

CONFIGURATION 2
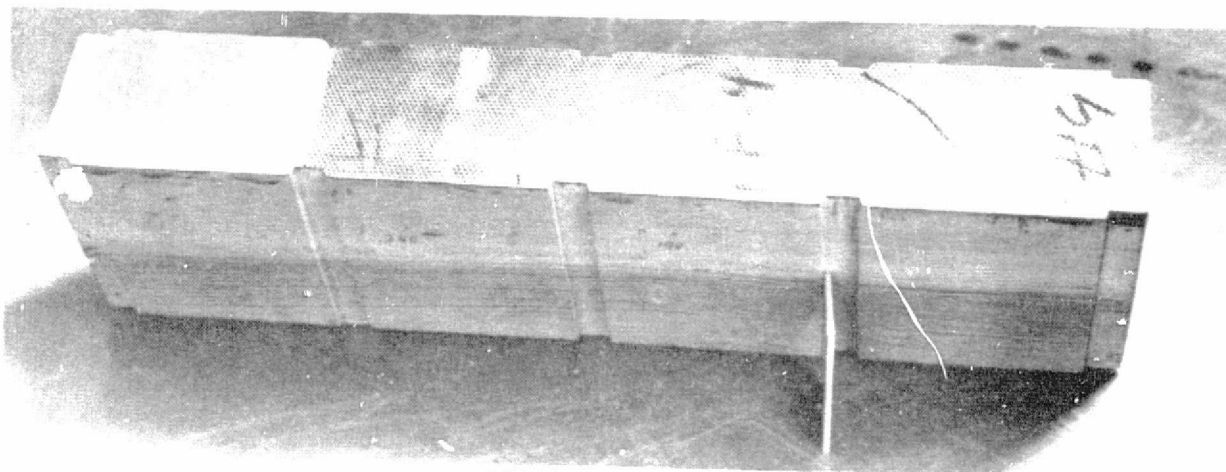
CONFIGURATION 3

Figure 25. Test Panel Configurations for M = 0.0.
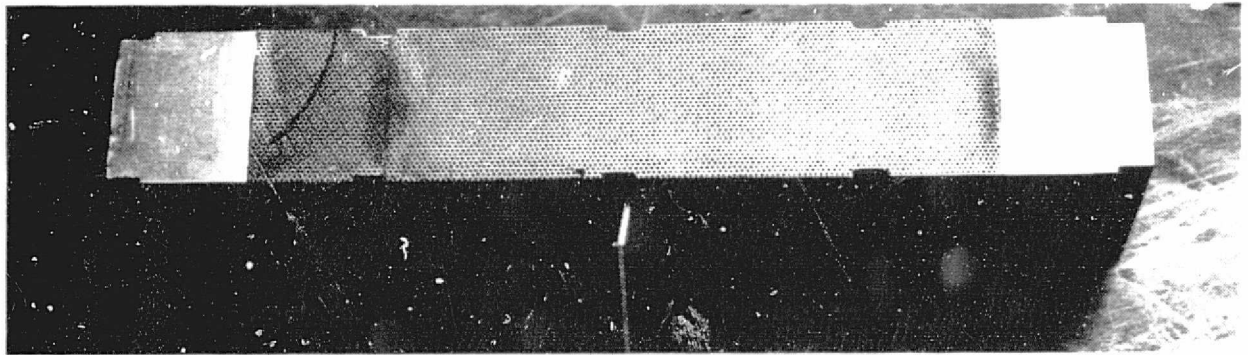
CONFIGURATION 4

CONFIGURATION 5
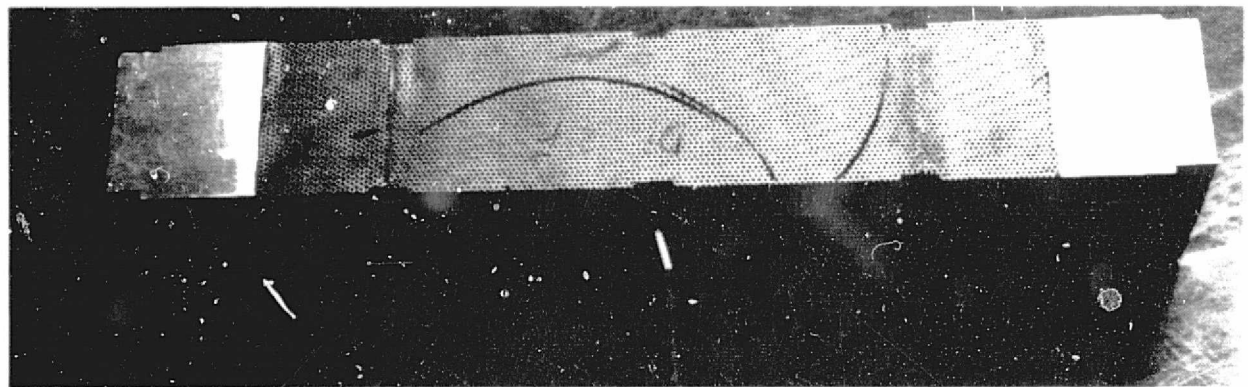
CONFIGURATION 6

Figure 26. Test Panel Configurations for M = 0.4.

using the mathematical model with either a hard-walled or soft-walled panel configuration, and these predictions were correlated with test results. Attenuation performance of each test configuration was determined by comparing energy flux before and after the lining. Although generally good correlation between theory and experiment was obtained, some portions of the test data were not accurately represented by the predictions. To assess the relative level of errors in the analytical model and test data, a series of parameter variations and curve fit studies were made for the measured data.

Data Acquisition

Space correlated measurements of acoustic pressure were made in the grazing flow duct facility for each of the single and multisegment lining configurations and a hard-walled test section. These data consisted of measuring the amplitude and phase of a moving microphone, relative to a fixed microphone, along the test section centerline in one of two test procedures:

- Frequency Scan

  The separation distance between microphones is fixed and frequency is varied

- Microphone Traverse

  The separation distance is varied for a constant discrete frequency

An extensive test program was conducted and all frequency scan and axial traverse data are presented in ref. 37.

A complete set of acoustic and flow environmental parameters was measured and recorded for each test condition. The temperature of the air supply for the flow duct test section varied with ambient conditions. To establish the desired value of reduced frequency, kH, excitation frequency was adjusted for each test condition to compensate for temperature changes. To estimate the modal content of the acoustic field in the test section for the lining configurations, traverse data was measured for a hard-walled test section prior to each of the panel test conditions.

Frequency scans were made for each panel configuration to experimentally determine the frequency of maximum attenuation. Although the panels were designed for a reduced frequency of kH = 10 tolerances of the facing sheet material caused some detuning of the liners. To ensure that the test panels were tested over a range of frequencies that included their peak attenuations, the limits of this range were determined by examination of the frequency scan data. These limits, kH = 9.6 and 10.16, were then established as the two test frequencies for all panel configurations.

Determination of Modal Content

The incident modal content of the duct acoustic field for each test condition was determined by analyzing the traverse data for a hard-walled test section. It was assumed that this modal content of the incident sound field would not be significantly altered by the presence of the liners. The validity of this assumption will be discussed later. The interactions of incident and reflected modes was interpreted with the aid of an analytical expression for the quantity pp* which is a measure of the rms pressure. From the expansion for pressure given by equation (9), pp* is:

41

$$pp^* = \sum_{n=0}^{N-1}\left\{\left|a_n\right|^2 + \left|b_n\right|^2\right\} + \sum_{n=0}^{N-1}\sum_{m\neq n}^{N-1} a_n a_m^* e^{-i(\overrightarrow{\lambda}_n - \overrightarrow{\lambda}_m^*)z}$$

$$+\sum_{n=0}^{N-1}\sum_{m\neq n}^{N-1} b_n b_m^* e^{-i(\overleftarrow{\lambda}_n - \overleftarrow{\lambda}_m^*)(L-z)} + \sum_{n=0}^{N-1}\sum_{m\neq n}^{N-1} a_n b_m^* e^{-i(\overrightarrow{\lambda}_n + \overleftarrow{\lambda}_m^*)z}\, e^{i\overleftarrow{\lambda}_m^* L} \qquad (24)$$

$$+\sum_{n=0}^{N-1}\sum_{n\neq m}^{N-1} b_n a_m^* e^{-i(\overleftarrow{\lambda}_n + \overrightarrow{\lambda}_m^*)z}\, e^{i\overrightarrow{\lambda}_m^* L}$$

This expression shows that the rms pressure is a combination of terms which are grouped as either interactions of incident modes with themselves and reflected modes with themselves, or interactions between incident and reflected modes. The axial variation of pp* is dependent upon differences of propagation constants for the terms that contain the interactions of incident modes with themselves or the interaction of reflected modes with themselves. The terms that contain the contributions of the ir   ions between incident and reflected modes are a function of the sum of the modal p   constants. An effective wavelength for each of these two types of interaction terms can L   d by dividing 2π by either Real $(\overrightarrow{\lambda}_n - \overrightarrow{\lambda}_m^*)$ or Real $(\overrightarrow{\lambda}_n + \overleftarrow{\lambda}_m^*)$. This indicates that the axial variation for self-interaction has a long wavelength while the axial variation for cross-interaction has a short wavelength.

To illustrate the use of equation (24) it is applied to the case of two propagating modes in a hard-walled infinite length duct with M = 0 where reflections are neglected.

$$pp^* = \left|a_0\right|^2 + \left|a_1\right|^2 + a_0 a_1^* e^{-i(\lambda_0 - \lambda_1^*)z} + a_1 a_0^* e^{-i(\lambda_1 - \lambda_0^*)z}$$

Calculated axial distributions of rms pressure magnitude are shown on Figures 27 through 29 for various combinations of fundamental and second incident modes. The axial variation of pressure magnitude is quite sensitive to differences in magnitude and phase of the modal content. Recalling that $\mu_n = 2n\pi/H$ for a duct with hard-walls, for a frequency parameter of kH = 10.16 and H = 10.16 cm (4 inches), the propagation constants become

λ_0 = 1.000/cm (2.54/inch)

λ_1 = .786/cm (2.00/inch)

The effective wavelength for the interaction of the first and second incident modes is 29.5 cm (11.6 inches) which correlates well with the oscillations in the rms pressure evident in these plots.
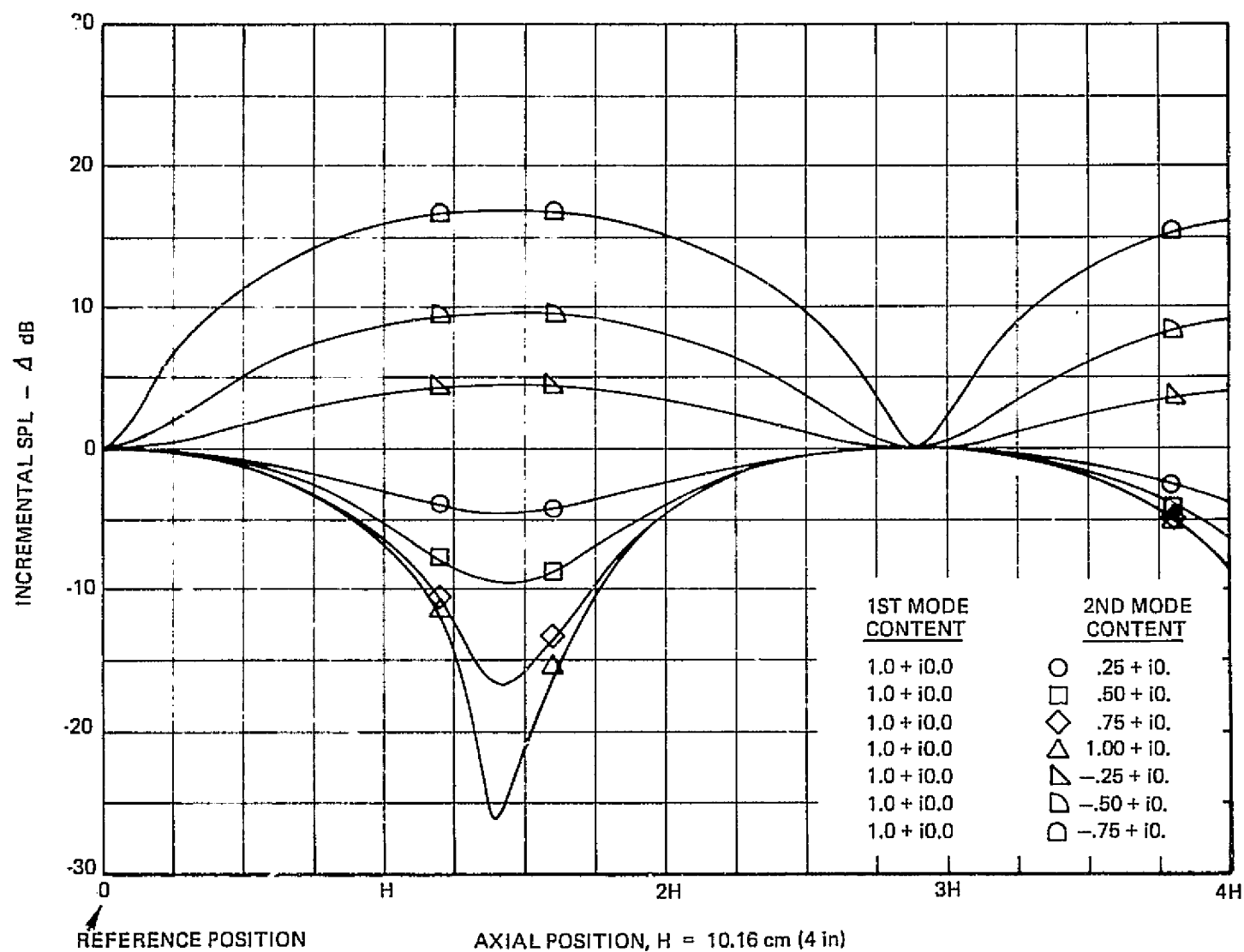
Figure 27. Typical Computed Hard-Wall (Centerline) Pressure Distributions, kH = 10.16, M = 0.
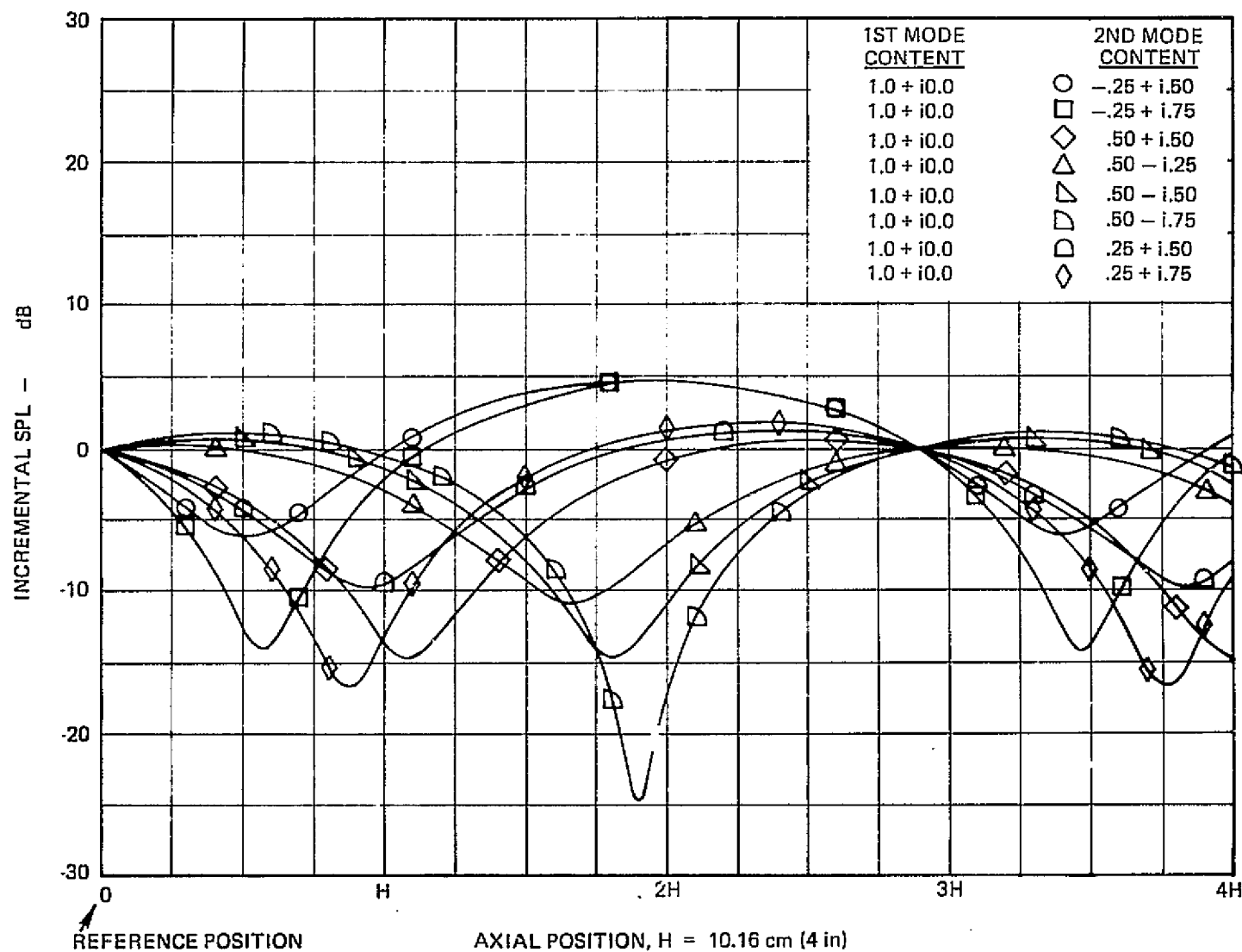
Figure 28. Typical Hard-Wall (Centerline) Pressure Distribution, kH = 10.16, M = 0.

44
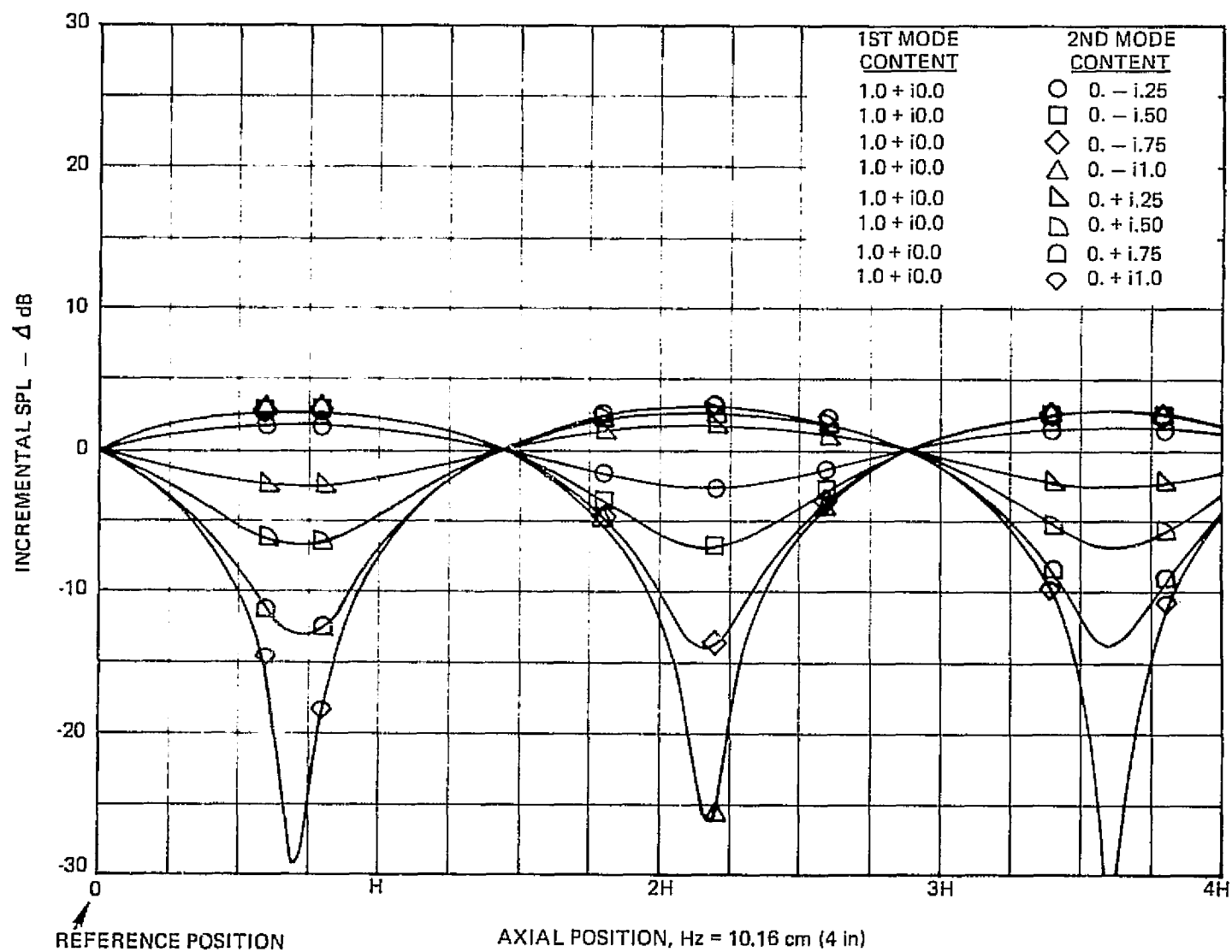
Figure 29. Typical Hard-Wall (Centerline) Pressure Distributions, kH = 10.16, M = 0.

The chart legend reads:

1ST MODE CONTENT	2ND MODE CONTENT	
1.0 + i0.0	○	0. − i.25
1.0 + i0.0	□	0. − i.50
1.0 + i0.0	◇	0. − i.75
1.0 + i0.0	△	0. − i1.0
1.0 + i0.0	◁	0. + i.25
1.0 + i0.0	◖	0. + i.50
1.0 + i0.0	◗	0. + i.75
1.0 + i0.0	◇	0. + i1.0

Y-axis: INCREMENTAL SPL — Δ dB

X-axis: AXIAL POSITION, Hz = 10.16 cm (4 in)

REFERENCE POSITION

45

Similar reasoning was used to study the interaction between the first and second modes which is evident in the measured hard-wall traverses. Measured pressure magnitude (rms) and phase (with respect to the fixed microphone) for two typical hard-walled test conditions are plotted versus microphone separation on Figures 30 and 31 for frequency parameters of kH = 9.6 and 10.16 respectively. In addition to the interaction of the first and second incident modes, interaction between incident and reflected modes can be seen to be present for kH = 9.6 as indicated by the small amplitude, short wavelength variations superimposed on the larger amplitude long wavelength variations. The wavelength of the shortwave is approximately 3.56/cm (1.4/inch). The effective wavelength for the three possible incident and reflected modal combinations are:

Modal Interaction	Effective Wavelength
$a_0 b_0$	3.15/cm (1.24/inch)
$a_1 b_1$	3.99/cm (1.57/inch)
$a_0 b_1$	3.51/cm (1.38/inch)

These wavelengths indicate that the most probable interaction is between the fundamental incident mode and the second reflected mode. Modal reflection is from the impedance discontinuity at the junction of the test section and the flow diffuser.

Modal coefficients for the first and second modes were determined by fitting the traverse data with centerline pressure calculated by the multisegment analysis. The analytical predictions are shown on Figures 30 and 31 by broken lines. Since the multiple segment analysis does not account for reflections at the end of the hard-wall portion of the test section, the analytical predictions do not have the small amplitude, short wavelength variation seen in the test data, but overall correlation is good.

The set of modal coefficients determined from the six sets of measured hard-wall data is given in Table 6. The magnitudes of these coefficients are nearly the same, while the phase was changed to fit the traverse data for the individual tests.

Figure 32 depicts a typical traverse measurement for a hard-walled test section with uniform flow, M = 0.4. Analyses similar to those performed for the M = 0 case were also conducted for uniform flow. Very little second mode content was found to be present in the sound field. Therefore, all M = 0.4 test data were evaluated on the assumption that only the plane wave was incident.

Analytical/Experimental Correlations

Measured liner traverse data were correlated with corresponding analytical predictions to validate the improved suppression performance of phased liners. Modal coefficients determined by the hard-wall traverse data analyses and liner impedance values based on measured flow resistance data were input to the multisegment duct analysis to predict the pressure magnitude and phase along the duct centerline for configurations 1 through 6. The use of hard-walled modal coefficients is based on the assumption that the presence of a liner does not alter the modal structure of the test section. Liner impedances (Tables 7 and 8) for the test frequencies at kH values of 9.6 and 10.16 were calculated from measured flow resistance data and the values of characteristic impedance of air, ρc, which are given for each test condition in Table 9.
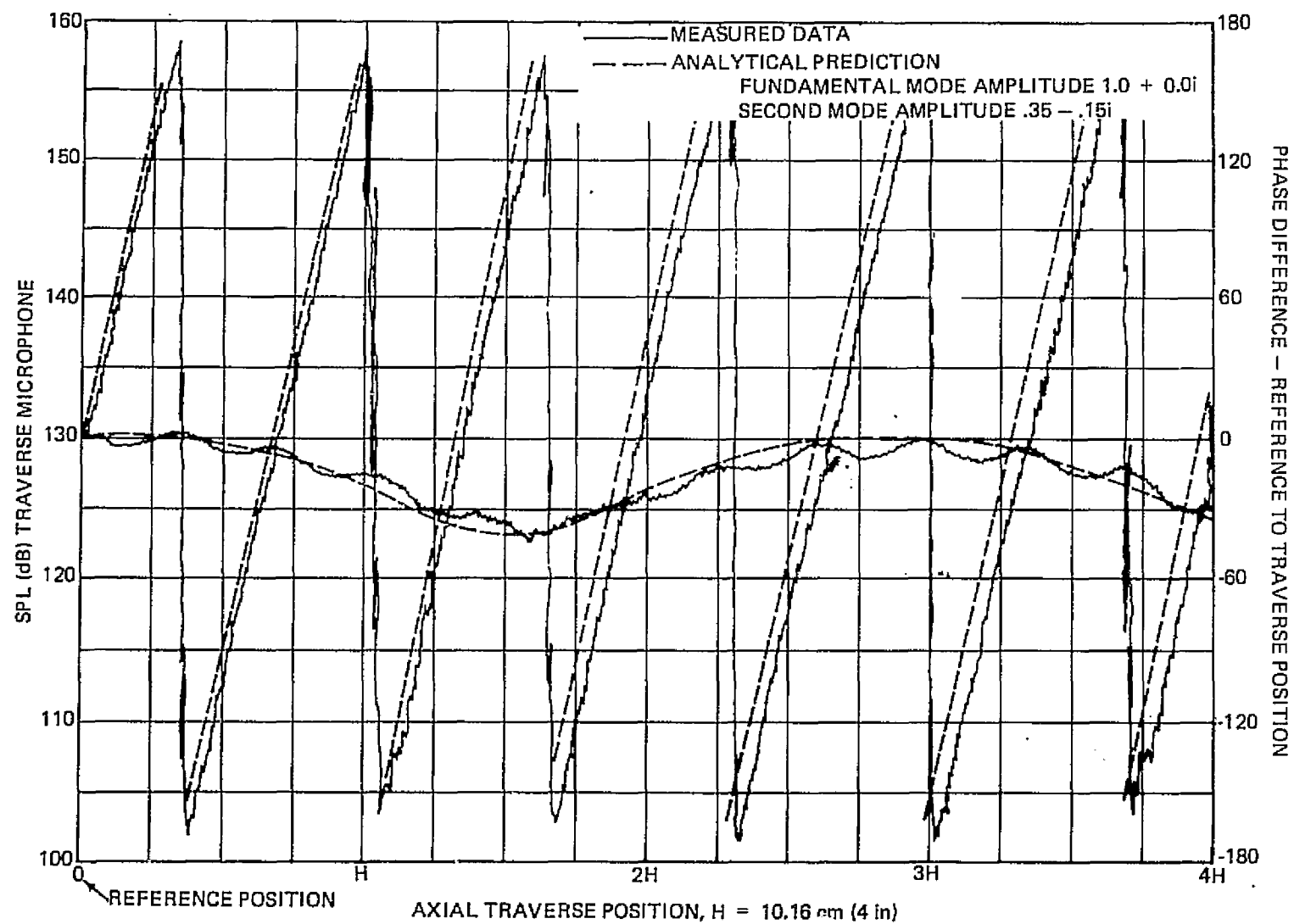
Figure 30. Comparison of Measured and Predicted Centerline Variations of Pressure Magnitude and Phase for a Hard-Wall Test Section, kH = 9.6, M = 0.

47
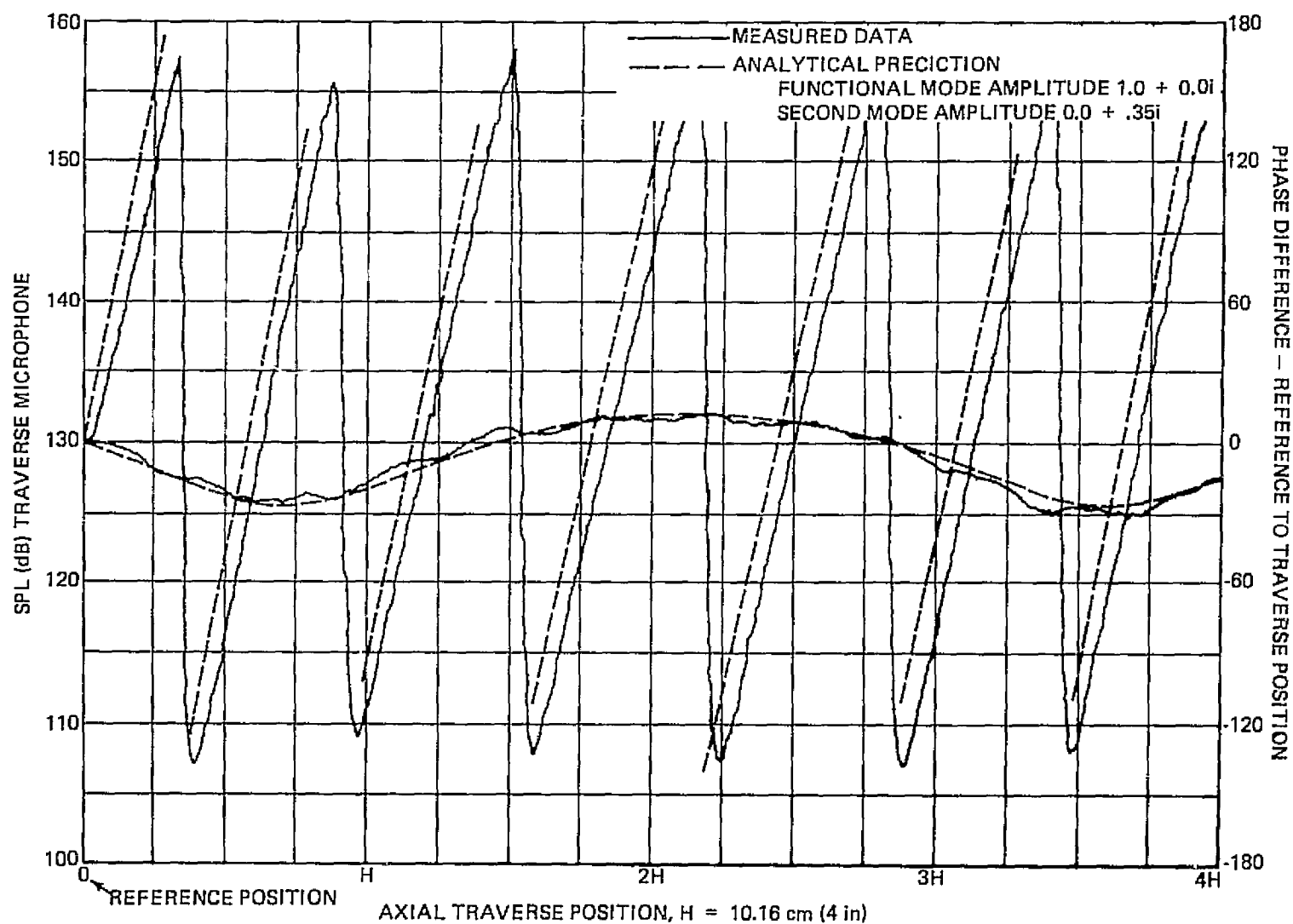
Figure 31. Comparison of Measured and Predicted Centerline Variations of Pressure Magnitude and Phase for a Hard-Walled Test Section, kH = 10.16, M = 0.

48

TABLE 6
MODAL COEFFICIENTS FOR HARD-WALLED TEST SECTION, M = 0.

PANEL I.D.	REDUCED FREQUENCY (KH)	COEFFICIENTS	
		MODE 1	MODE 2
1	9.6	1.0 + 0.0i	0.30 - 0.25i
2	9.6	1.0 + 0.0i	0.35 - 0.15i
3	9.6	1.0 + 0.0i	0.35 - 0.15i
1	10.16	1.0 + 0.0i	0.10 + 0.30i
2	10.16	1.0 + 0.0i	0.00 + 0.35i
3	10.16	1.0 + 0.0i	0.20 + .025i
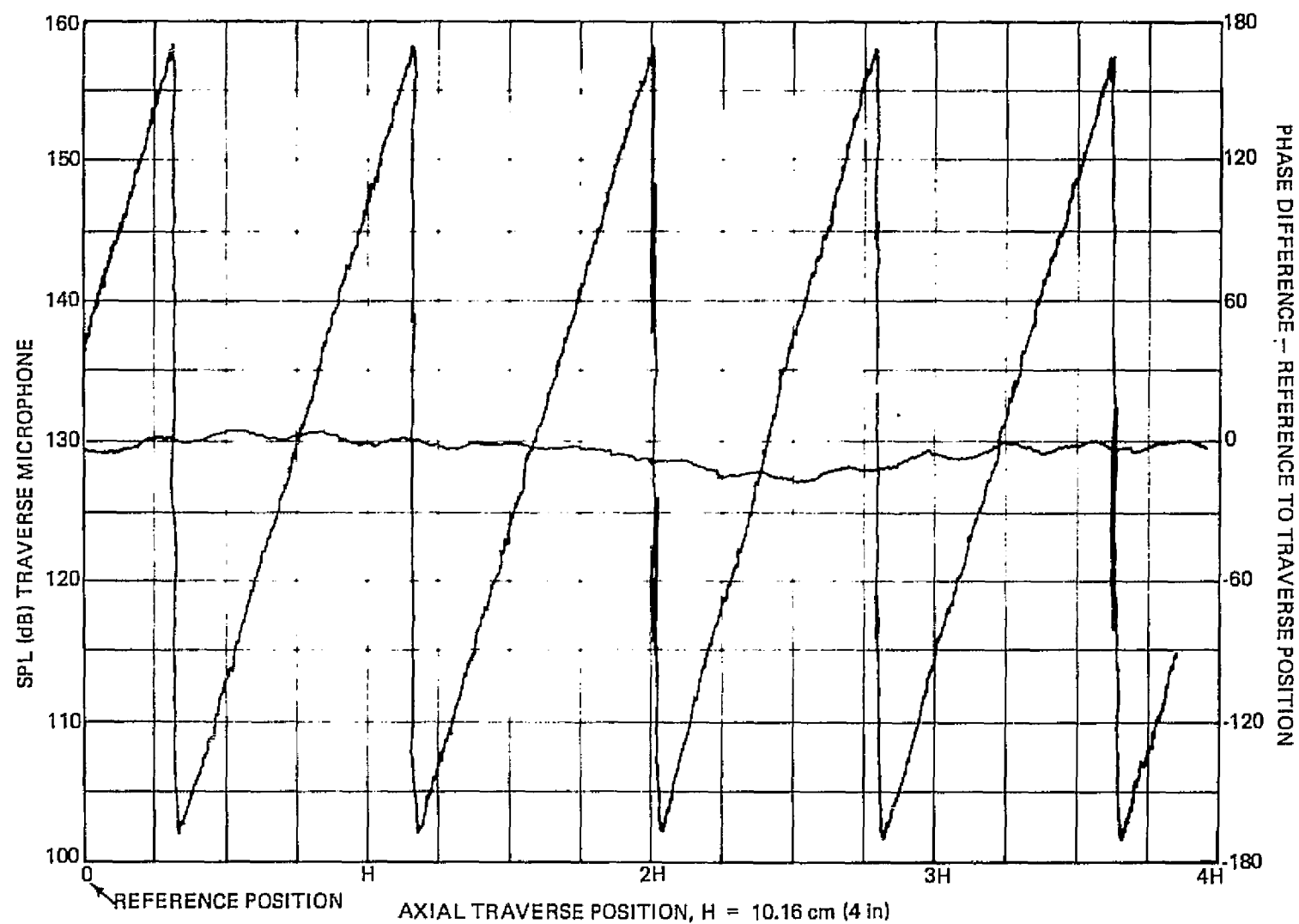
Figure 32. Measured Centerline Variations of Pressure Magnitude and Phase for a Hard-Wall Test Section, kH = 10.16, M = 0.4.

TABLE 7
SOUND POWER LEVEL (PWL) ATTENUATIONS FOR ANALYTICAL/EXPERIMENTAL CORRELATIONS OF
TEST PANEL CONFIGURATIONS 1 THROUGH 3, M = 0.0.

LINER CONFIGURATION	kH	MODAL CONTENT* SECOND MODE	SPECIFIC IMPEDANCE OF EACH PANEL SEGMENT	ATTENUATION SOUND POWER LEVEL Δ dB
UNIFORM CONFIGURATION 1	9.6	.30 — .25i	1.30 — 2.03i	17.9
	10.16	.10 + .30i	1.30 — 1.85i	17.0
THREE-SEGMENT CONFIGURATION 2	9.6	.35 — .15i	1.20 — 0.97i 1.57 — 2.32i 0.63 — 0.56i	21.0
	10.16	0.0 + .35i	1.32 — 0.93i 1.73 — 2.27i 0.69 — 0.54i	23.4
TWO-SEGMENT CONFIGURATION 3	9.6	.35 — 15i	0.05 — 1.52i 1.58 — 1.49i	19.0
	10.16	0.0 + .35i	0.05 — 1.41i 1.58 — 1.33i	21.6

*FUNDAMENTAL MODE AMPLITUDE = 1.0 + 0.0i

TABLE 8
SOUND POWER LEVEL (PWL) ATTENUATIONS FOR ANALYTICAL/EXPERIMENTAL CORRELATIONS OF
TEST PANEL CONFIGURATIONS 4 THROUGH 6, M = 0.4.

LINER CONFIGURATION	kH	MODEL CONTENT* SECOND MODE	SPECIFIC IMPEDANCE OF EACH PANEL SEGMENT	ATTENUATION SOUND POWER LEVEL Δ dB
UNIFORM CONFIGURATION 4	9.6	0.0 + 0.0i	.640 — 1.036i	15.1
	10.16	0.0 + 0.0i	.640 — .927i	16.5
TWO-SEGMENT CONFIGURATION 5	9.6	0.0 + 0.0i	.046 — .721i .815 — .858i	21.3
	10.16	0.0 + 0.0i	.046 — .639i .815 — .750i	22.5
THREE-SEGMENT CONFIGURATION 6	9.6	0.0 + 0.0i	.595 — .531i .778 — 1.193i .416 — .245i	20.4
	10.16	0.0 + 0.0i	.595 — .438i .778 — 1.072i .416 — .158i	26.5

*FUNDAMENTAL MODE AMPLITUDE = 1.0 + 0.0i

TABLE 9
ENVIRONMENTAL AND PANEL CHARACTERISTICS
FOR EXPERIMENTAL/ANALYTICAL CORRELATIONS

CONFIGURATION I.D. NO.	CHARACTERISTIC IMPEDANCE OF AIR* cgs RAYLS	PANEL		BACKING DEPTH	
		I.D. NO.	FLOW RESISTANCE** cgs RAYLS	cm	in
1	38.5	FO-1	50.0	0.41	0.16
2	38.8	DF-1	46.5	0.66	0.26
		DF-2	61.0	0.36	0.14
		DF-3	24.4	0.97	0.38
3	38.6	RF-1	1.8	0.61	0.24
		DF-4	61.0	0.48	0.19
4	36.9	FO-1F	23.6	0.71	0.28
5	37.2	RF-1F	1.7	0.99	0.39
		DF-4F	30.3	0.76	0.30
6	37.0	DF-1F	22.0	0.99	0.39
		DF-2F	28.8	0.64	0.25
		DF-3F	15.4	1.27	0.50

*BASED ON MEASURED TEMPERATURE AND PRESSURE
**BASED ON NOMINAL VALUES OF TEST DATA AND INCREASED 10 PERCENT TO ACCOUNT FOR CORE AND
ADHESIVE BLOCKAGE

Measured traverse data for configurations 1 and 4 and the corresponding analytical predictions are shown on Figures 33 and 34 for a reduced frequency kH = 9.6 and Figures 35 and 36 for kH = 10.16. The correlation of pressure magnitude is very good for the kH = 10.16 case. A slight difference in phase exists between measured and predicted values near the end of the traverse. The measured interactions between incident and reflected waves in the bounding hard-wall sections were accurately predicted by the analysis. The correlation for the 9.6 value of kH is generally poor, although the incident/reflected standing wave patterns for the hard-wall sections in front of both configurations were accurately predicted. Configuration 4 analytical pressure distributions do not agree well with measured data but do exhibit trends similiar to the measured data. The magnitude and phase of the predicted axial pressure distribution agree with measured data for configuration 1 for the first 25.4 cm (10 inches) of traverse distance. However, the measured and analytically predicted pressure variations are in poor agreement for the last 12.7 cm (5 inches) of lining length. An investigation of possible reasons for this poor agreement is presented later in an evaluation of the analytical model.

Figures 37 through 40 present comparisons of analytical predictions and measured traverse data for configurations 3 and 5. The large pressure excursions in the 12.2-cm (4-inch) hard-wall section for configuration 3 were accurately predicted for both test frequencies. These excursions are due to interaction of the right moving fundamental mode and the left moving fundamental mode that is reflected from the low resistance liner. While the amplitude fluctuations are large, little energy was reflected from the interface. Analytical predictions for configuration 5 with an incident plane wave do not correlate well with measured data, which would indicate that some second mode is present in this test data. In a study to be discussed later, better agreement with the test data was obtained by including the second mode in the analytical predictions.

Experimental/analytical correlations for configurations 2 and 6 are shown on Figures 41 and 42, for kH = 9.6 and 43 and 44 for kH = 10.16. These correlations are quite good considering the complex structure of standing waves in the three dissipative panels. Reflected wave patterns established in the hard-wall sections in front of the lining configurations are predicted very well for each corresponding set of hard-wall coefficier.ts. These data illustrate modal conditioning in the first two liners and attenuation in the last liner, as was predicted during design of the three-segment configuration. The poorest agreement exists for configuration 2 for kH = 9.6. For this case, the analysis poorly predicts the behavior of both the phase and magnitude of the measured data in the last 12.2 cm (4 inches) of the liner.

Evaluation of Liner Performance

While it may be overly optimistic to say that excellent correlation is obtained, it is noted that the essential features of the measured data are predicted. This good agreement between theory and experimental data indicates that the crossover frequency model is a realistic mathematical model for the impedance properties of the test panels and that the modal coefficients determined by analyzing traverse data for a hard-walled test section usually provide a reasonable estimate of the modal content of the acoustic field for the test section with a soft-wall. In addition, these correlations validate the analysis technique and verify that the previously identified physical mechanisms do enable phased linings to provide improved attenuation performance.

It must be emphasized that the measured axial centerline pressure distribution is not a measure of suppression performance of the lining. Sound pressure level attenuation measured for an axial traverse indicates duct sound power attenuation only when there is but one soft-wall mode

54

Figure 33. Analytical-Experimental Correlation. Comparison of Measured and Predicted Axial Distribution of Centerline Pressure Magnitude and Phase for Liner Configuration No. 1, kH = 9.6, M = 0. Incident Modal Coefficients were Determined from Analysis of Hard-Wall Data. Panel Impedances are Specified in Table 7.

55

Figure 34. Analytical-Experimental Correlation. Comparison of Measured and Predicted Axial Distribution of Centerline Pressure Magnitude and Phase for Liner Configuration No. 4, kH = 9.6, M = 0.4. Incident Modal Coefficients were Determined from Analysis of Hard-Wall Data. Panel Impedances are Specified in Table 8.

Figure 35. Analytical-Experimental Correlation. Comparison of Measured and Predicted Axial Distribution of Centerline Pressure Magnitude and Phase for Liner Configuration No. 1, kH = 10.16, M = 0.0. Incident Modal Coefficients were Determined from Analysis of Hard-Wall Data. Panel Impedances are Specified in Table 7.

Figure 36. Analytical-Experimental Correlation. Comparison of Measured and Predicted Axial Distribution of Centerline Pressure Magnitude and Phase for Liner Configuration No. 4, kH = 10.16, M = 0.4. Incident Modal Coefficients were Determined from Analysis of Hard-Wall Data. Panel Impedances are Specified in Table 8.
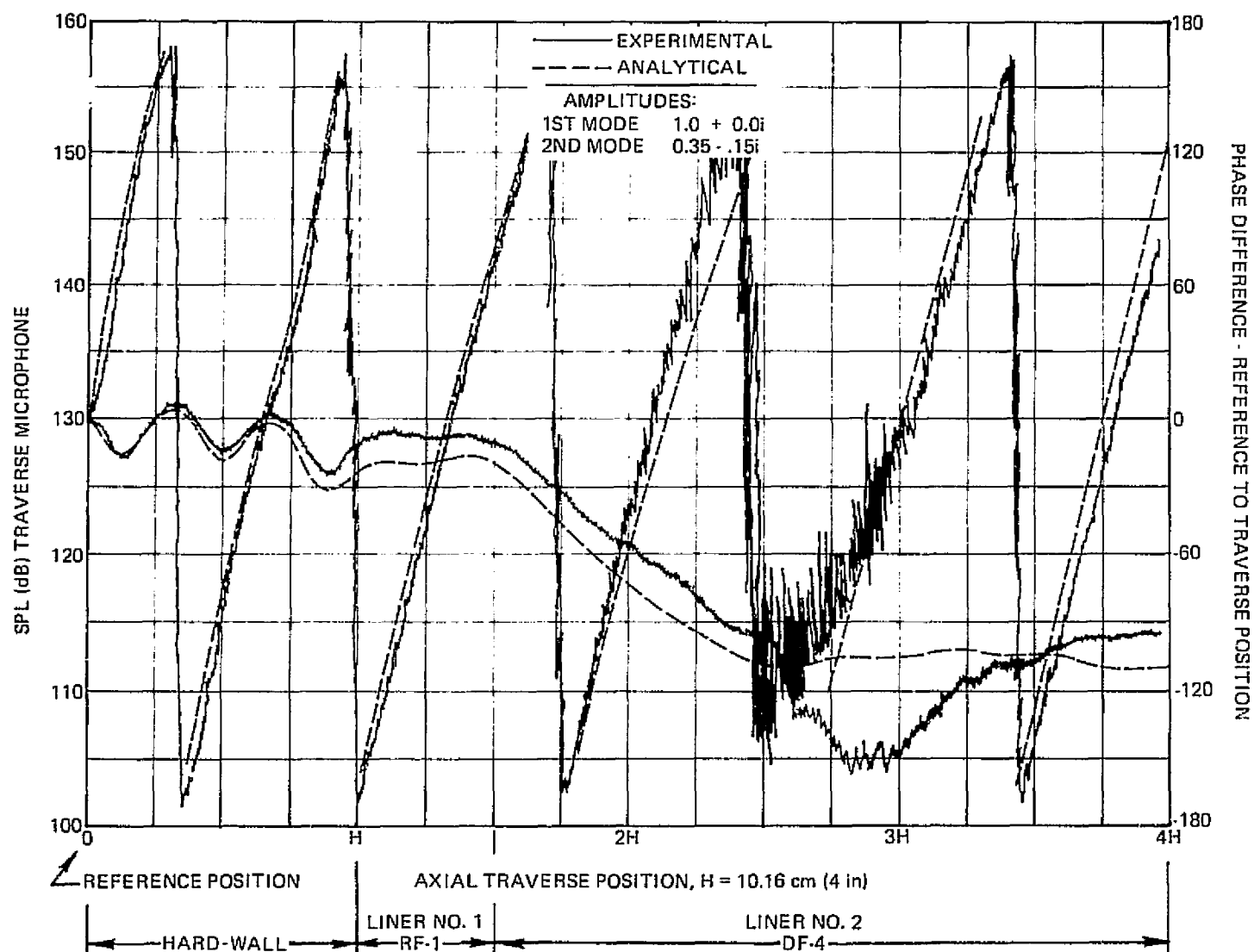
Figure 37. Analytical-Experimental Correlation. Comparison of Measured and Predicted Axial Distribution of Centerline Pressure Magnitude and Phase for Liner Configuration No. 3, kH = 9.6, M = 0.0. Incident Modal Coefficients were Determined from Analysis of Hard-Wall Data. Panel Impedances are Specified in Table 7.

Figure 38. Analytical-Experimental Correlation. Comparison of Measured and Predicted Axial Distribution of Centerline Pressure Magnitude and Phase for Liner Configuration No. 5, kH = 9.6, M = 0.4. Incident Modal Coefficients were Determined from Analysis of Hard-Wall Data. Panel Impedances are Specified in Table 8.

Figure 39. Analytical-Experimental Correlation. Comparison of Measured and Predicted Axial Distribution of Centerline Pressure Magnitude and Phase for Liner Configuration No. 3, kH = 10.16, M = 0.0. Incident Modal Coefficients were Determined from Analysis of Hard-Wall Data. Panel Impedances are Specified in Table 7.

Figure 40. Analytical-Experimental Correlation. Comparison of Measured and Predicted Axial Distribution of Centerline Pressure Magnitude and Phase for Liner Configuration No. 5, kH = 10.16, M = 0.4. Incident Modal Coefficients were Determined from Analysis of Hard-Wall Data. Panel Impedances are Specified in Table 8.

Figure 41. Analytical-Experimental Correlation. Comparison of Measured and Predicted Axial Distribution of Centerline Pressure Magnitude and Phase for Liner Configuration No. 2, kH = 9.6, M = 0.0. Incident Modal Coefficients were Determined from Analysis of Hard-Wall Data. Panel Impedances are Specified in Table 7.

Figure 42. Analytical-Experimental Correlation. Comparison of Measured and Predicted Axial Distribution of Centerline Pressure Magnitude and Phase for Liner Configuration No. 6, kH = 9.6, M = 0.4. Incident Modal Coefficients were Determined from Analysis of Hard-Wall Data. Panel Impedances are Specified in Table 8.

Figure 43. Analytical-Experimental Correlation. Comparison of Measured and Predicted Axial Distribution of Centerline Pressure Magnitude and Phase for Liner Configuration No. 2, kH = 10.16, M = 0.0. Incident Modal Coefficients were Determined from Analysis of Hard-Wall Data. Panel Impedances are Specified in Table 7.
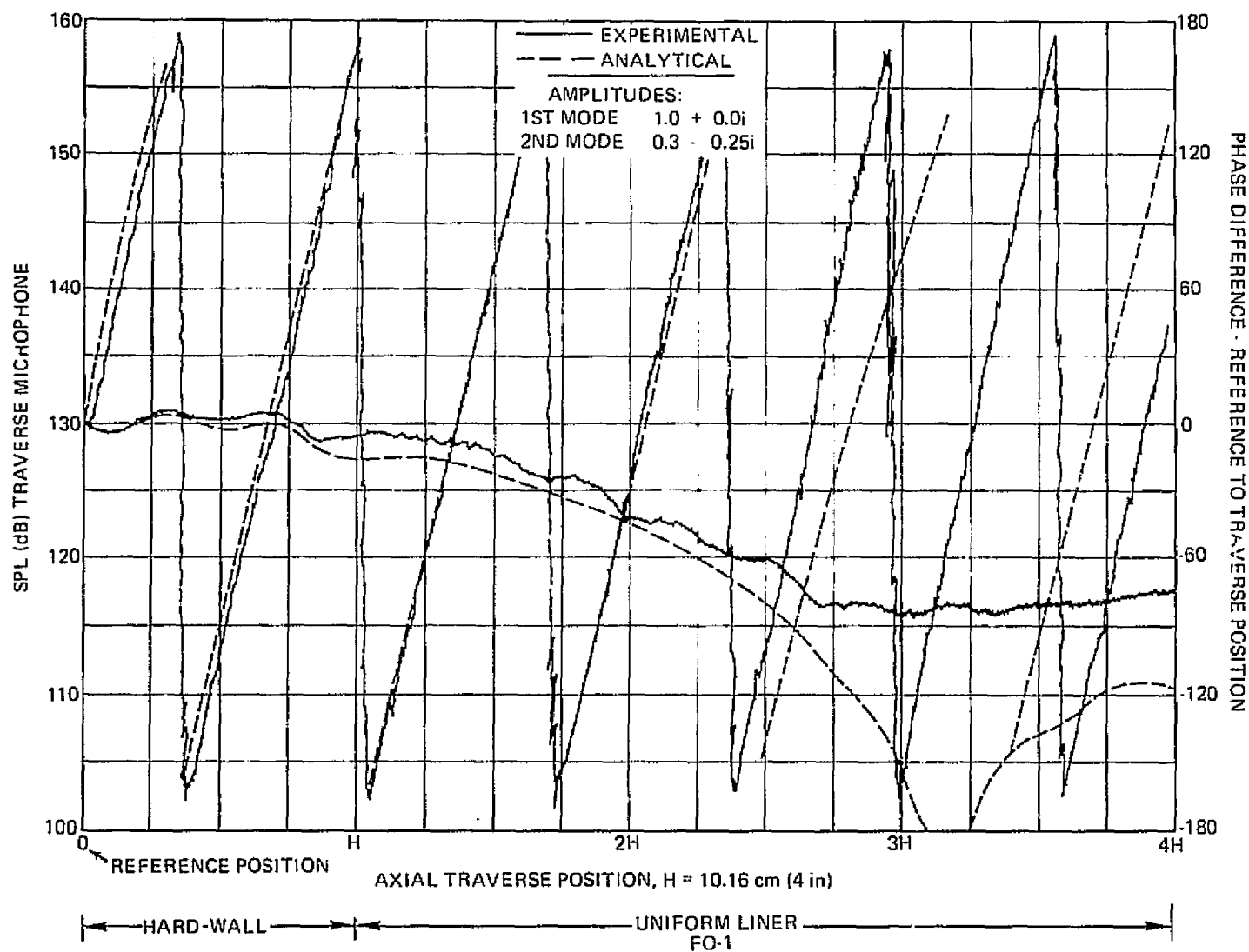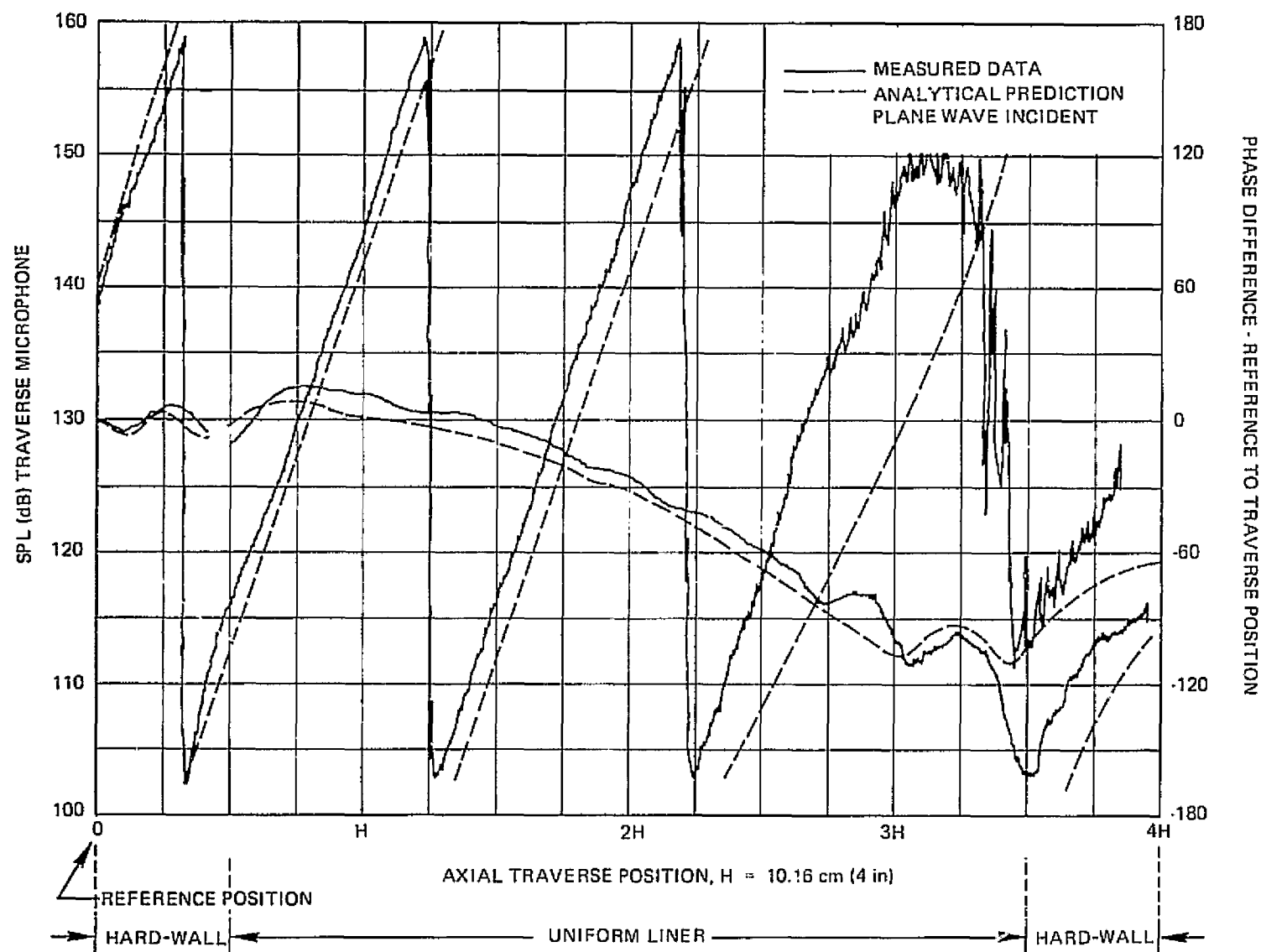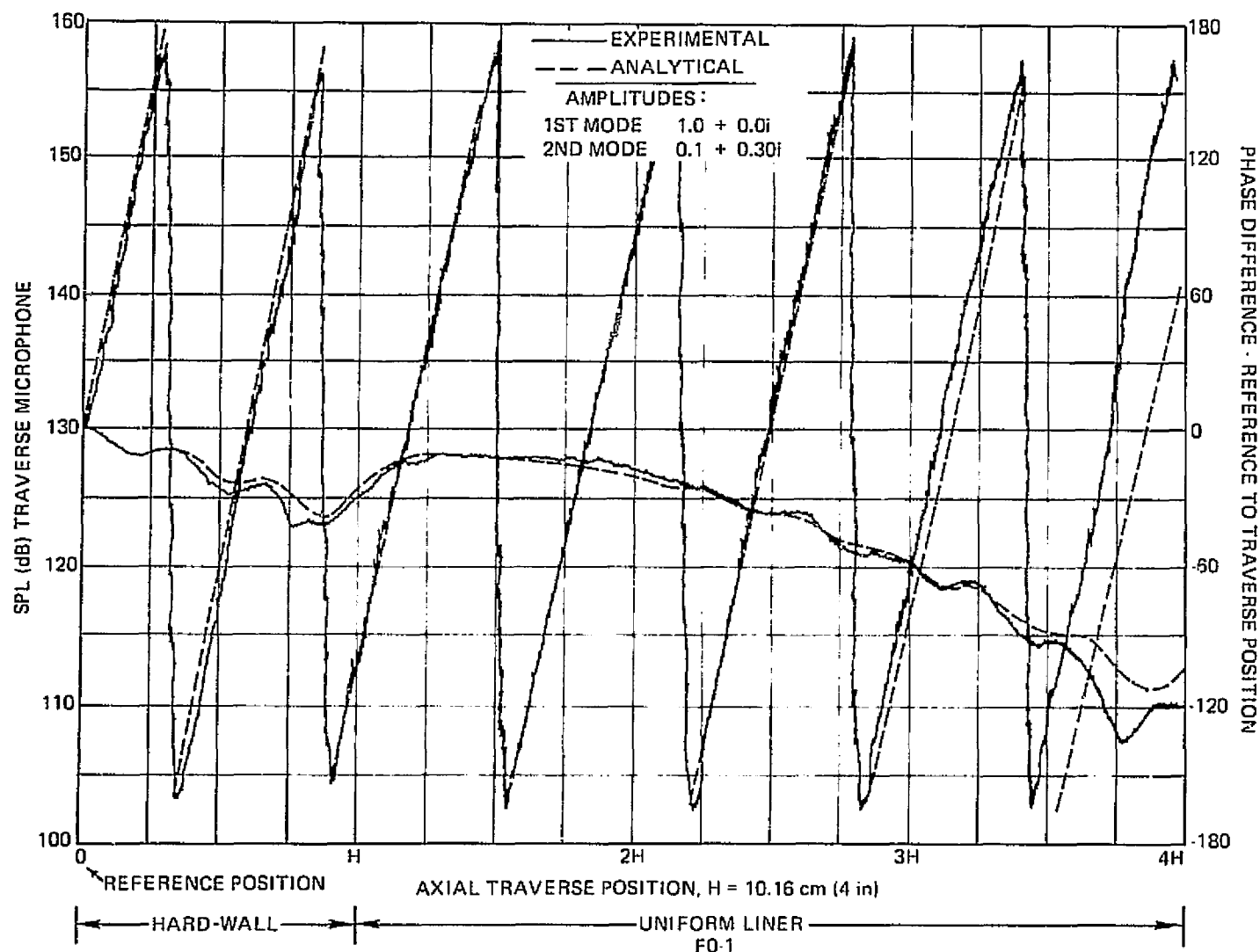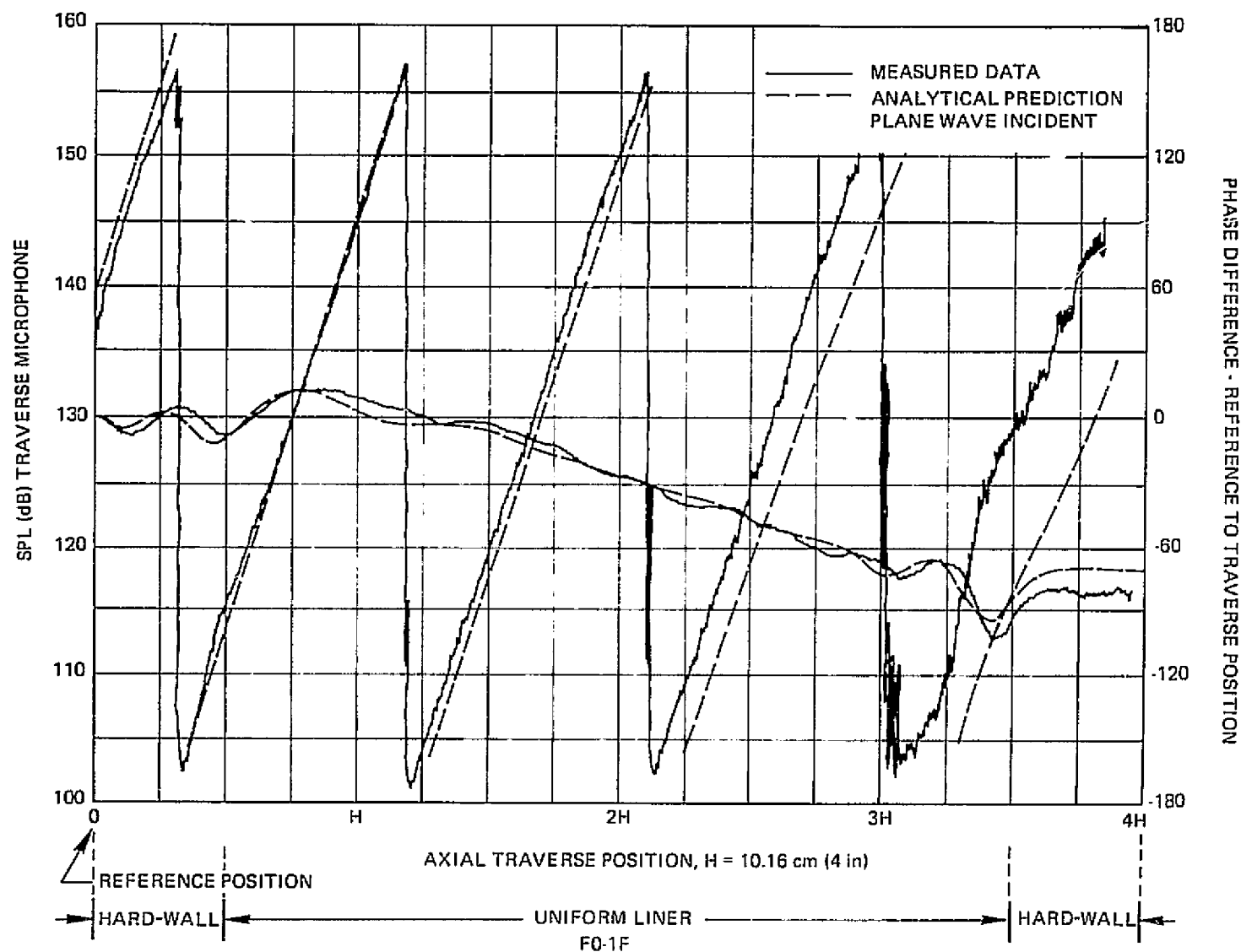
Figure 44. Analytical-Experimental Correlation. Comparison of Measured and Predicted Axial Distribution of Centerline Pressure Magnitude and Phase for Liner Configuration No. 6, kH = 10.16, M = 0.4. Incident Modal Coefficients were Determined from Analysis of Hard-Wall Data. Panel Impedances are Specified in Table 8.

propagating. More than one mode can propagate for the test frequencies; consequently, the axial standing wave pattern provides a means of correlating analysis and experiment. However, the attenuation performance of the lining configurations must be determined by comparing axial energy flux before and after the lining. Figure 45 depicts the axial variation of sound power attenuation for configuration 4 at a kH = 10.16. A comparison of this distribution of PWL with Figure 36 shows that the standing waves present in the SPL distribution would cause attenuation estimates based on SPL rather than on PWL to be in error.

Since limitations of the test facility did not allow measurement of transverse distributions of sound pressure level, sound power attenuations were computed for the test conditions. Modal coefficients which were determined from the hard-wall data were input to the segmented duct program to compute the energy flux values for the liner. If the capability to measure transverse profiles had existed, the energy flux could have been estimated by measuring transverse pressure magnitude and phase before and after the liner.* The profile data could have been used to determine modal coefficients for the hard-walled sections or to compute the integral of the rms pressure across the duct cross section. (Attenuation performance predicted by this quantity has been found to correlate well with the attenuations predicted by the energy flux expression.)

The sound power attenuations computed for each of the test conditions are presented in Tables 7 and 8. These calculated values are based on modal coefficients and impedance values obtained from test data. Comparisons of the sound power level attenuations of configurations 2 and 3 with configuration 1 are shown on Figures 46 and 47. Sound power level attenuations calculated for both test conditions are plotted versus reduced frequency, kH. Differences between configuration 1 (open symbols) and configurations 2 or 3 (closed symbols) illustrate the attenuation improvement of phased linings. These plots also show that these attenuations fall near to or within the attenuation envelope for the modal combinations used in the design studies (Figures 20 and 21).

For the zero Mach number tests at kH = 10.16, the two- and three-segment liners produced 4.6 and 6.4 dB more sound power attenuation respectively than the single-segment liner. The two- and three-segment liners produced 6.0 and 10.0 dB more attenuation than the single-segment optimum for M = 0.4 and kH = 10.16. These attenuation improvements are significant in view of the design constraints of the liners.

Evaluation of Theoretical and Experimental Methods

Although generally quite good correlation was obtained between theory and experiment, there were some portions of the test data which were not accurately represented by predictions. Some of the factors which may have contributed to this lack of correlation include the following:

- The analysis was based on a two-dimensional model while the experimental configuration involved a square duct.

*Several measurements of transverse SPL distribution for hard-wall conditions were made in the final phases of the program in an attempt to further substantiate the modal identification procedure. Unfortunately, this limited capability was obtained too late in the program to allow application to PWL determination.
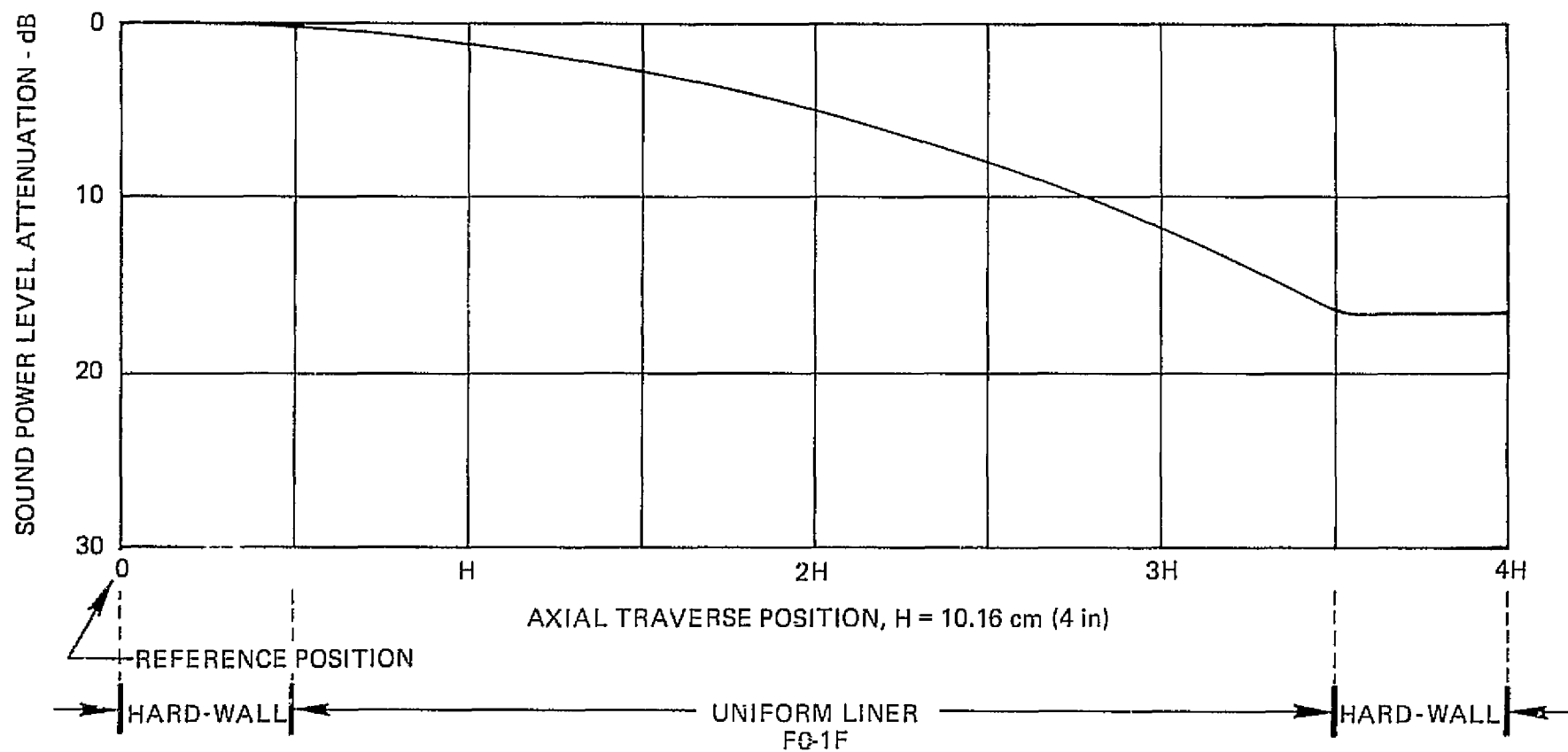
Figure 45. Calculated Axial Variation of Sound Power Attenuation for Liner Configuration No. 4, kH = 10.16, M = 0.4.
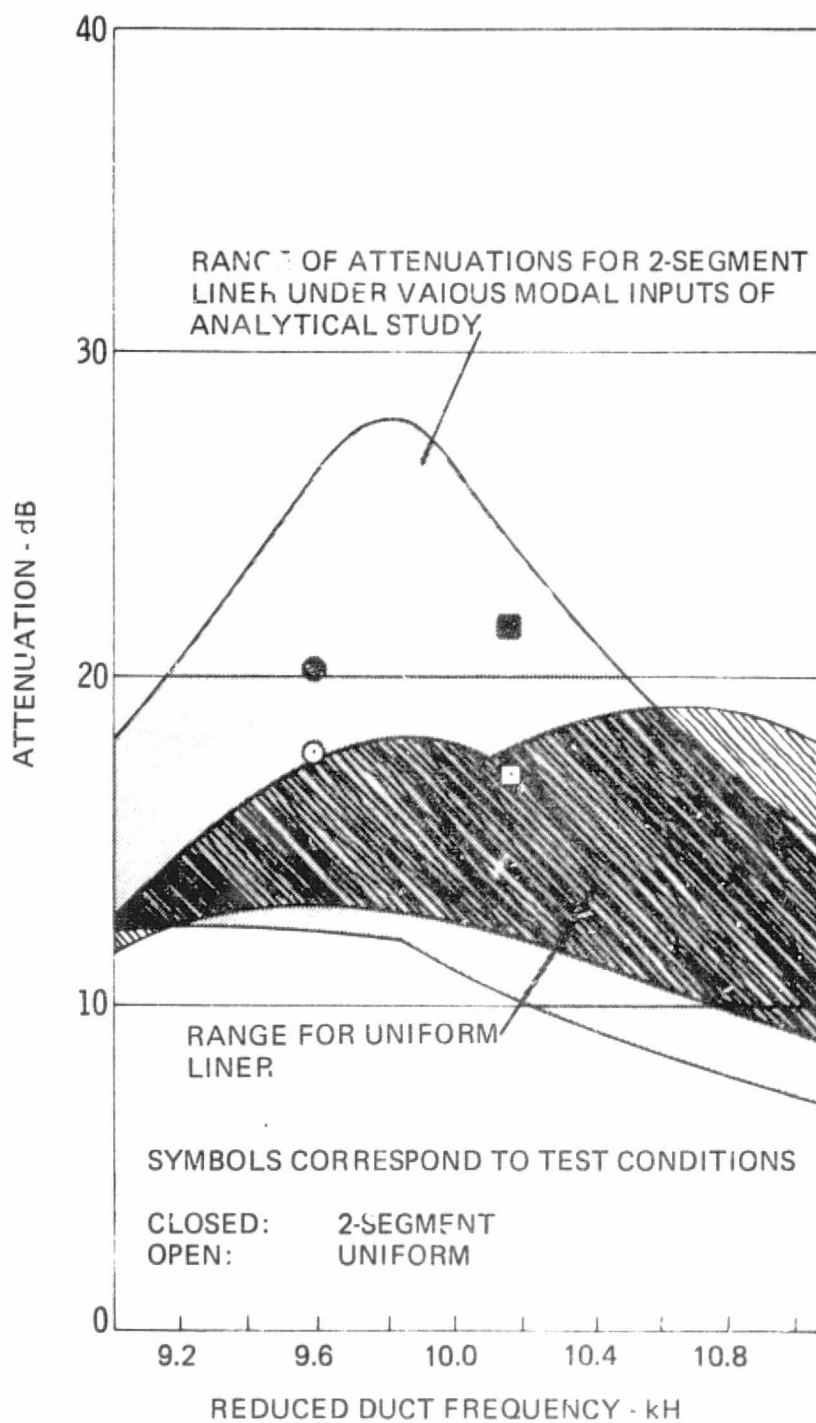
Figure 46. Analytical Evaluation of Configuration 2 Attenuation Performance at Test Frequencies.
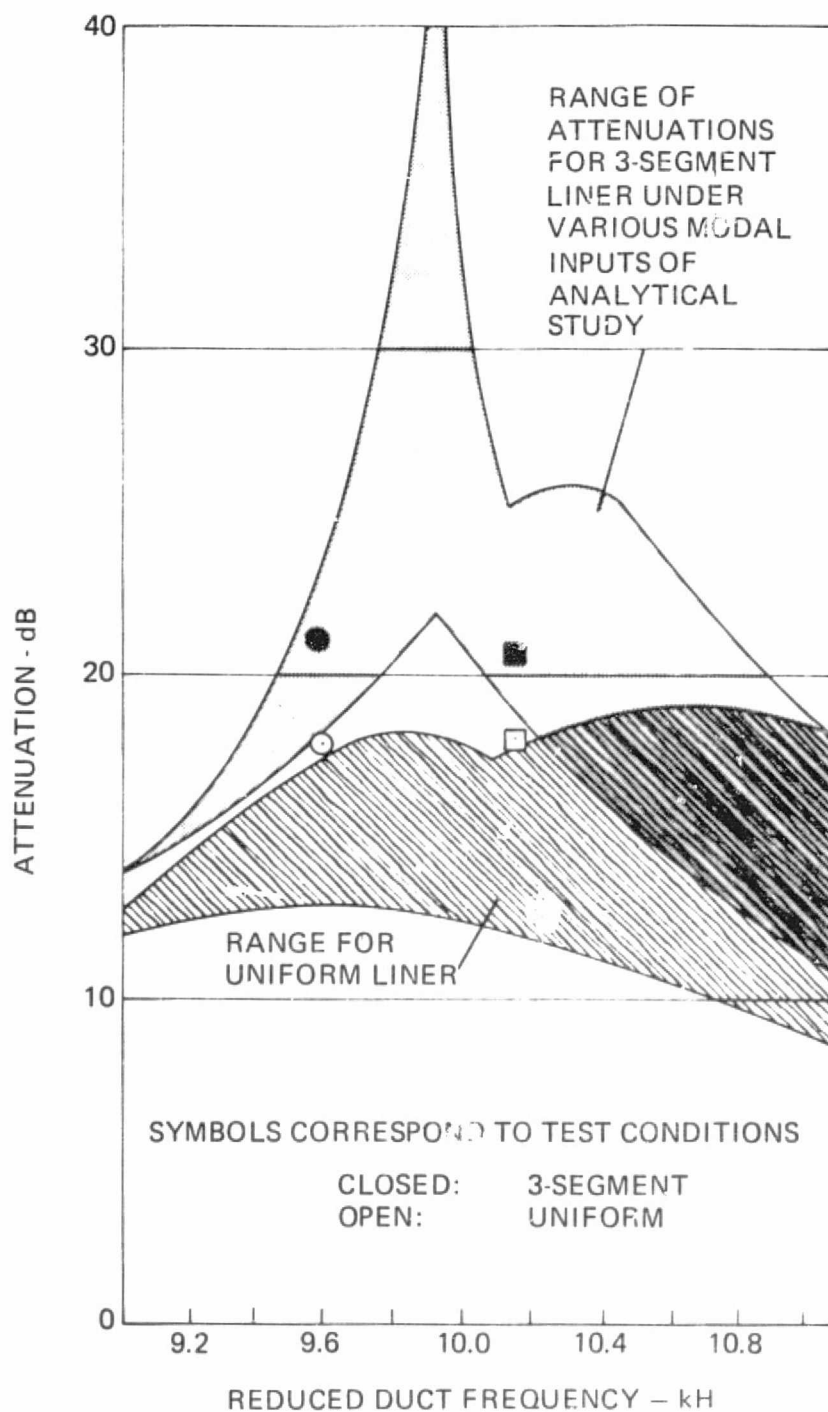
Figure 47. Analytical Evaluation of Configuration 3 Attenuation Performance
at Test Frequencies

- Incident modal content varied between tests and with the presence or absence of liners.

- It was not possible to determine exact values of liner impedance due to nonuniformity in facing sheet resistance, blockage effects, and uncertainty regarding the value of crossover frequency.

- The flow duct termination was not anechoic in the frequency regime of the tests.

Impedance effects were studied by arbitrarily changing the resistance by ± 10 percent for the M = 0 configurations. These results indicate that while agreement is improved by changes in resistance, in some instances initial estimates of resistance were adequate.

Another trend study shown on previous comparisons was the variation of modal content. This was accomplished by trial and error in the early stages of the program and indicated that modal content was variant not only from test to test but in the presence of the liner. Insight was gained into the actual model content in the presence of the liner as well as into test duct termination effects and actual liner impedance values by adjusting these parameters so as to provide a better fit to the measured data. Several analytical techniques were developed to automatically and accurately curve fit the data. Of those considered, the conjugate gradient optimization method was the most successful and will be the only one presented.

The cost function for application of the conjugate gradient technique is the mean square difference between the measured and predicted axial variation of duct centerline pressure (see Appendix J). Initial values of incident modal coefficients, and soft-wall segment impedances were input to the program, which systematically varied these input parameters to minimize the cost function. Modeling of the duct terminating diffuser was accomplished by placing a soft-wall segment of uniform impedance between the semi-infinite hard-wall termination and the test section. Wall impedance for this duct segment was also used as an input parameter to the gradient search curve fit program.

Results of this optimum analysis for hard-wall data are shown on Figures 48 and 49. The variables for this optimization study were second mode content and termination impedance. Since the termination wall impedance did not change from the starting value of $Z = \rho c$, it was felt that this impedance was adequate and it was thus fixed during subsequent analyses. The experimental/analytical correlation obtained for the hard-wall data are well within measurement accuracies and clearly show the termination impedance trends discussed in previous sections.

The optimization technique was also applied to configurations 1, 3 and 5 to identify possible causes for the poor correlation in some portions of the test data. Application of this technique to the data for configuration 1 (Figure 33) was accomplished in two steps. First the data were evaluated by varying incident modal content. Little improvement was noted (Figure 50) so next the impedance was allowed to vary as well. Results are presented on Figure 51. Here excellent correlation has been obtained for both amplitude and phase. While modal content changed only slightly, a relatively large increase in impedance was required to yield the improved correlation. These changes in impedance are not within the variations of the facing sheet flow resistance data. When attempts were made to cut samples from the panel for standing wave impedance tube checks, the face sheet separated from the panel, indicating poor bonding of facing to core. Unfortunately, this separation

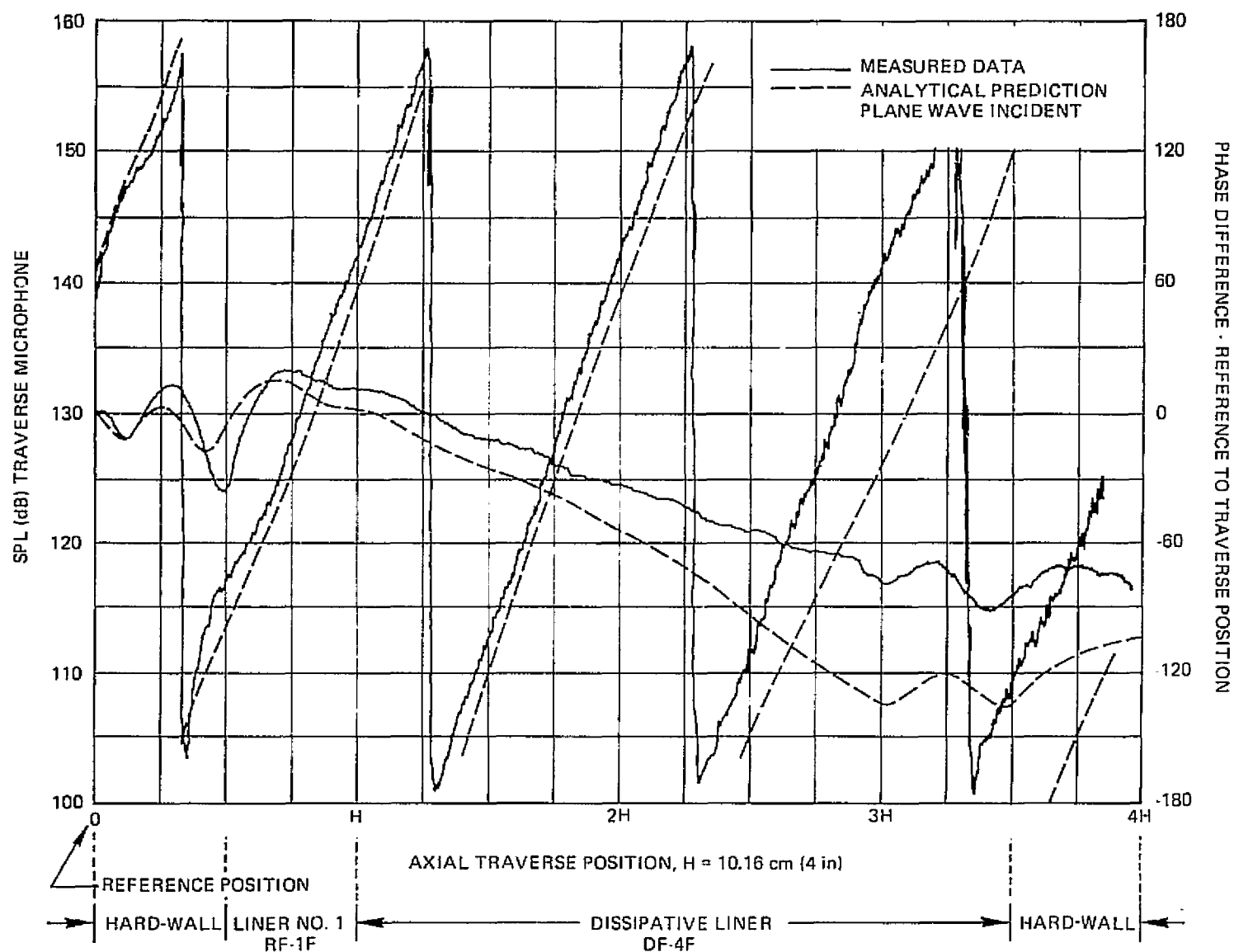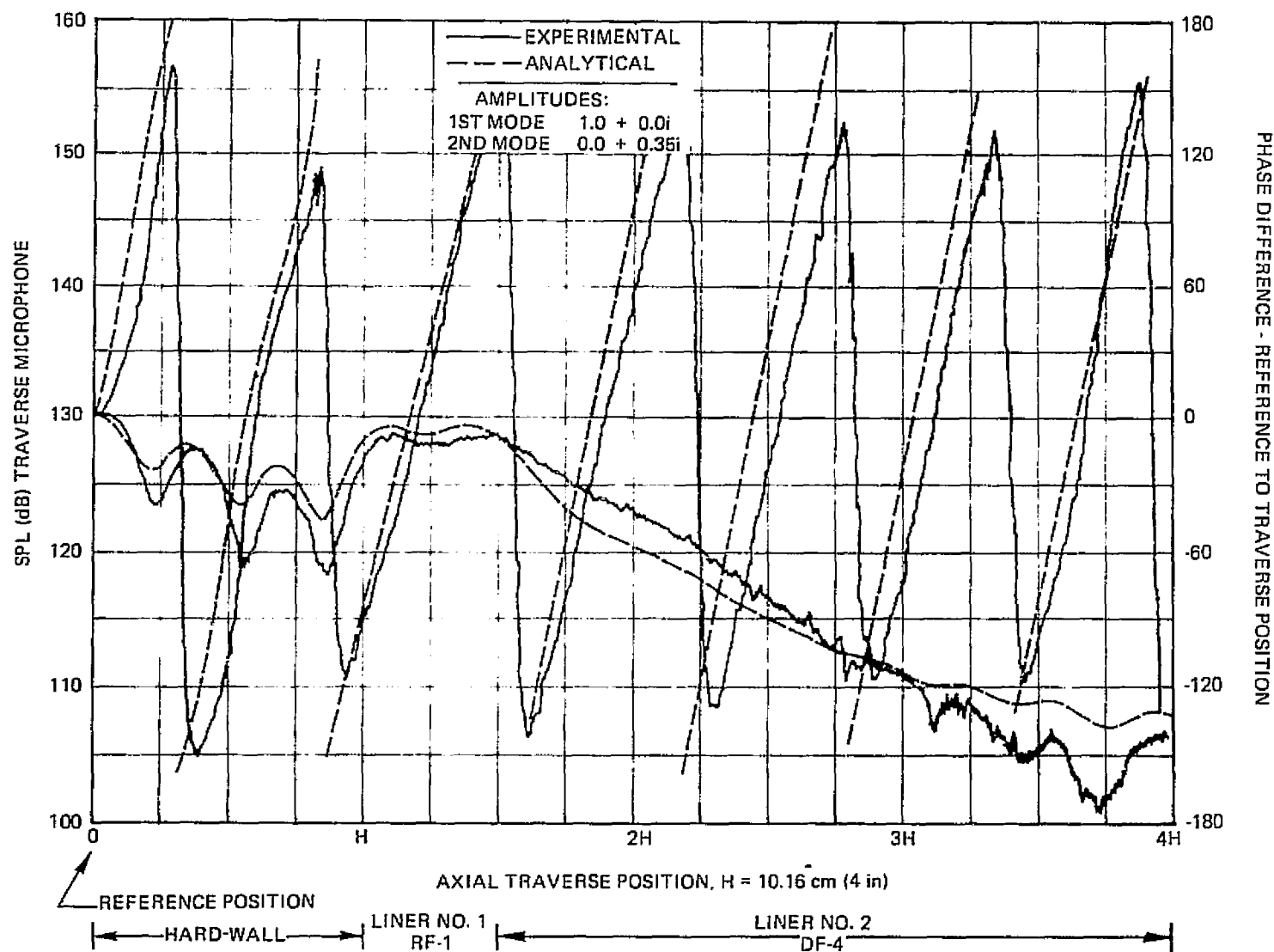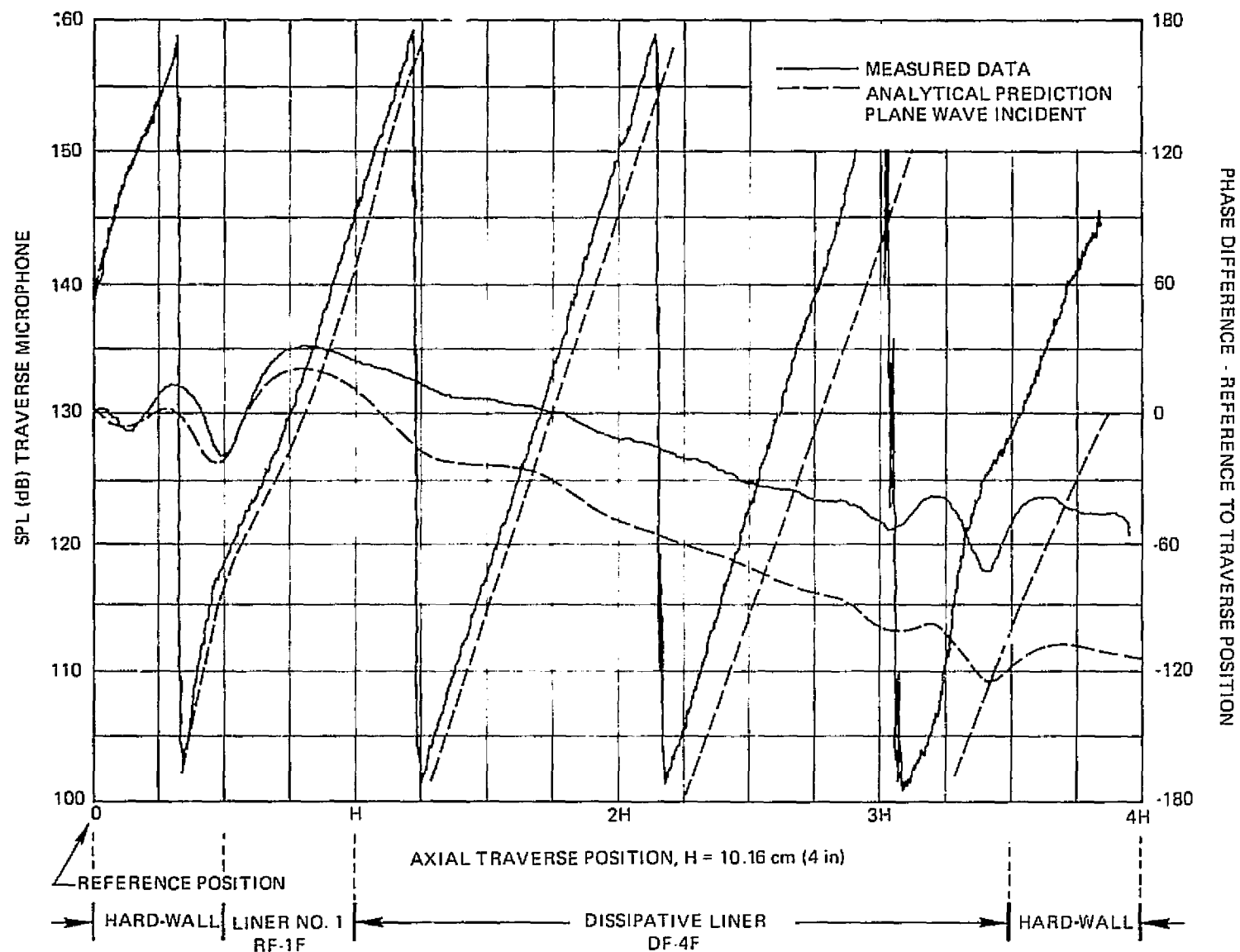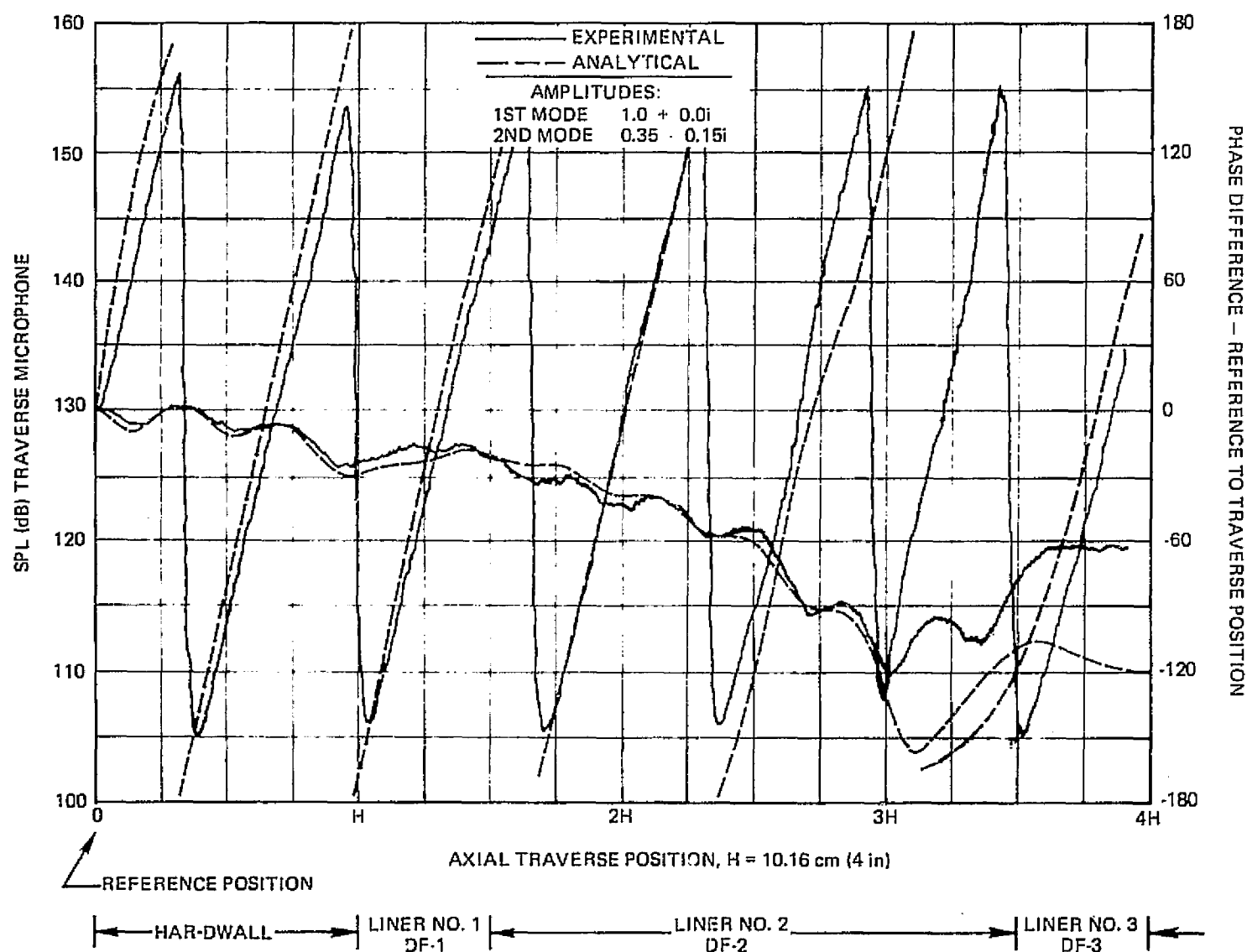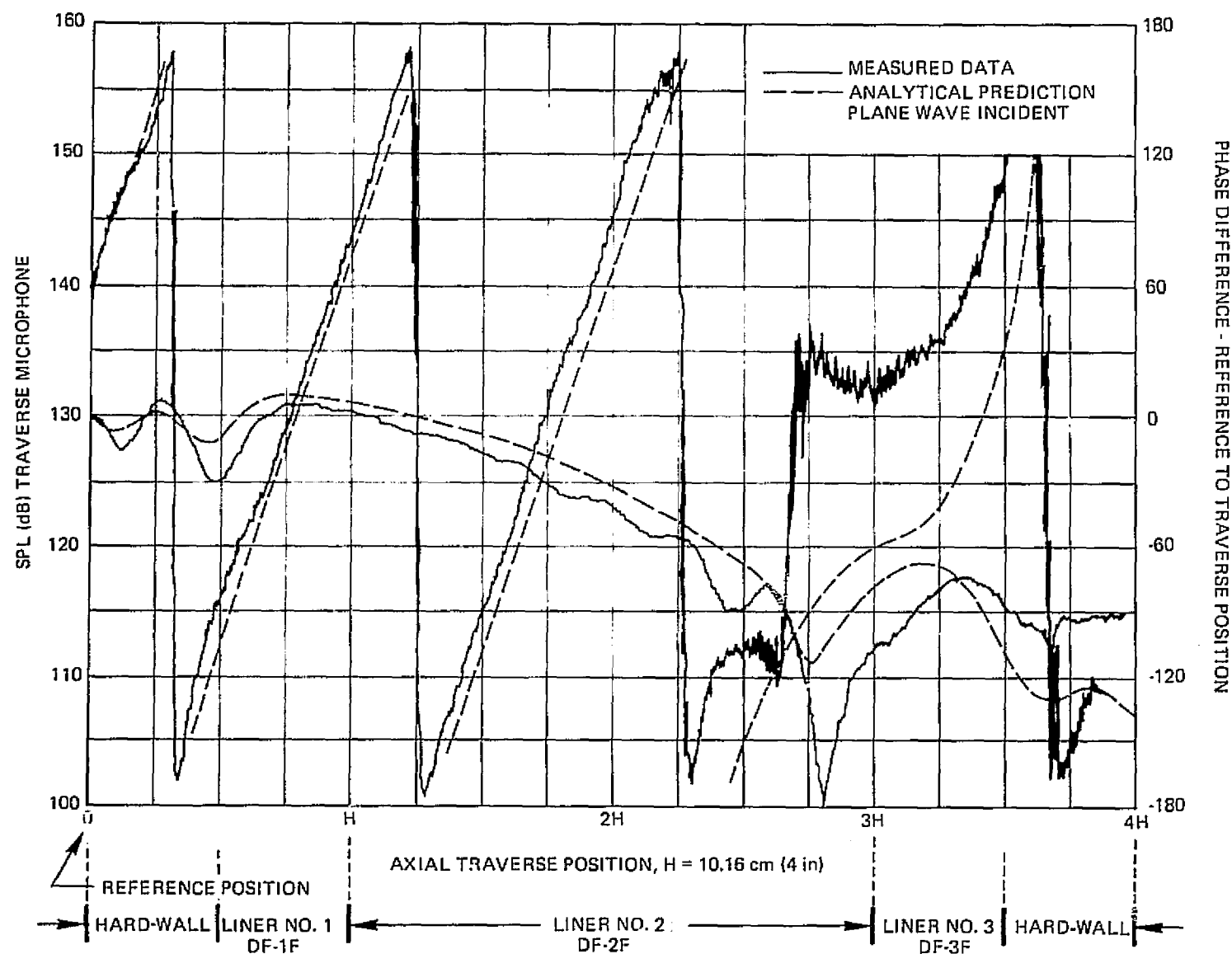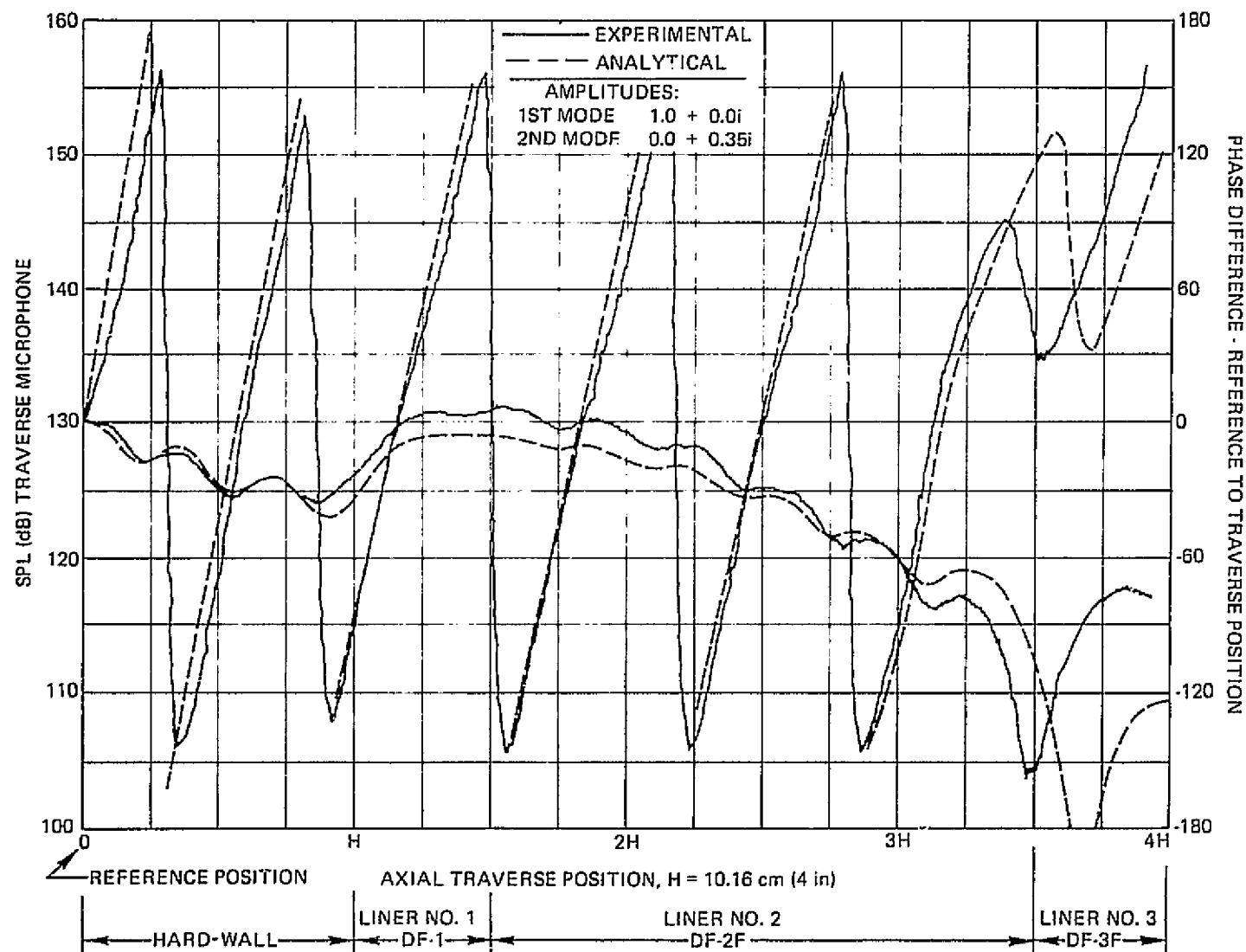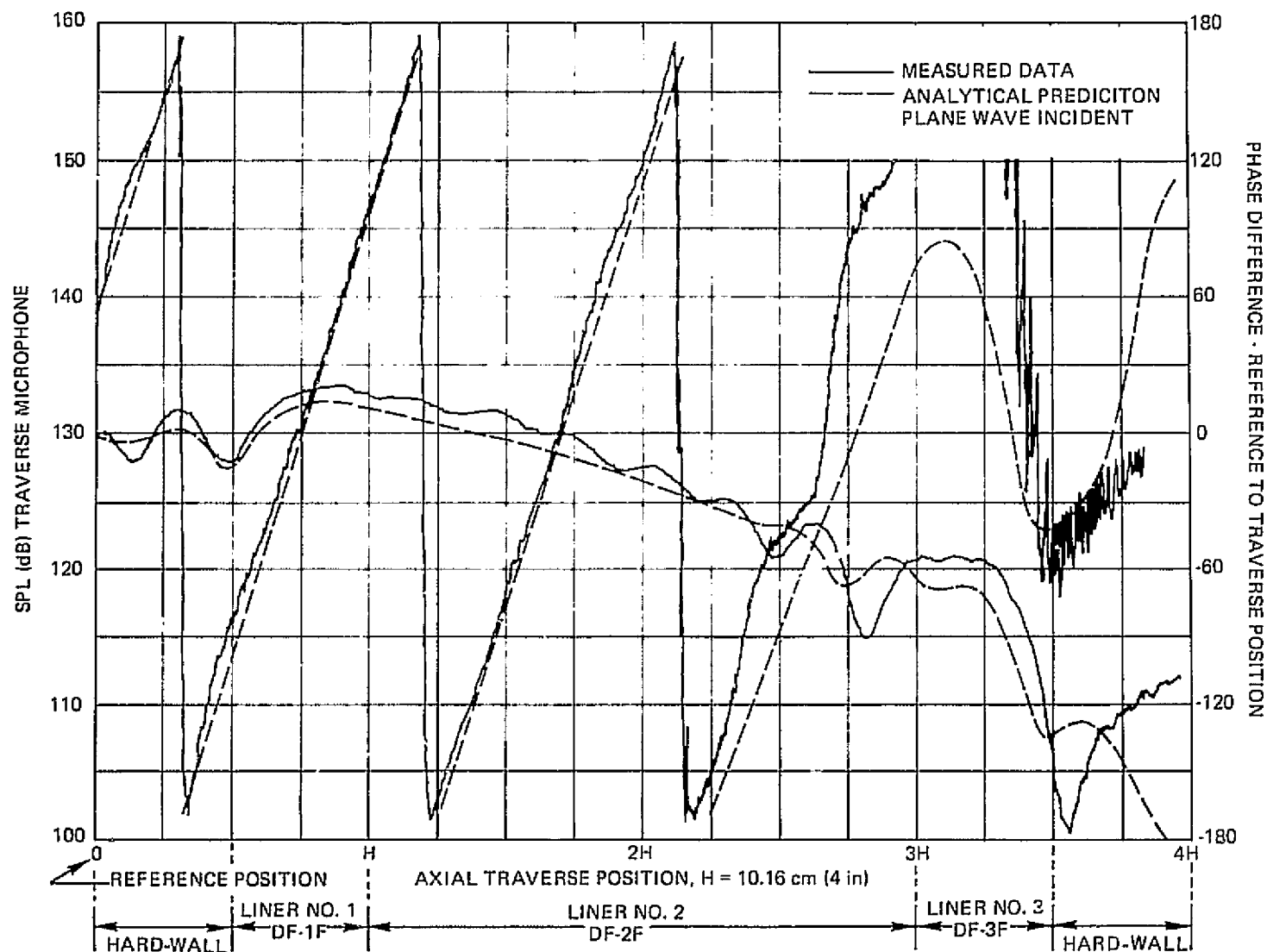Figure 48. Curve Fit to Experimental Data. Comparison of Measured and Predicted Axial Distribution of Centerline Pressure Magnitude and Phase for Hard-Wall Test Section, kH = 9.6, M = 0.4. Incident Modal Coefficients and/or Panel Impedance Varied to Give Best Correlation. Impedance of Soft-Walled Segment which Models Test Section Termination = ρ c.
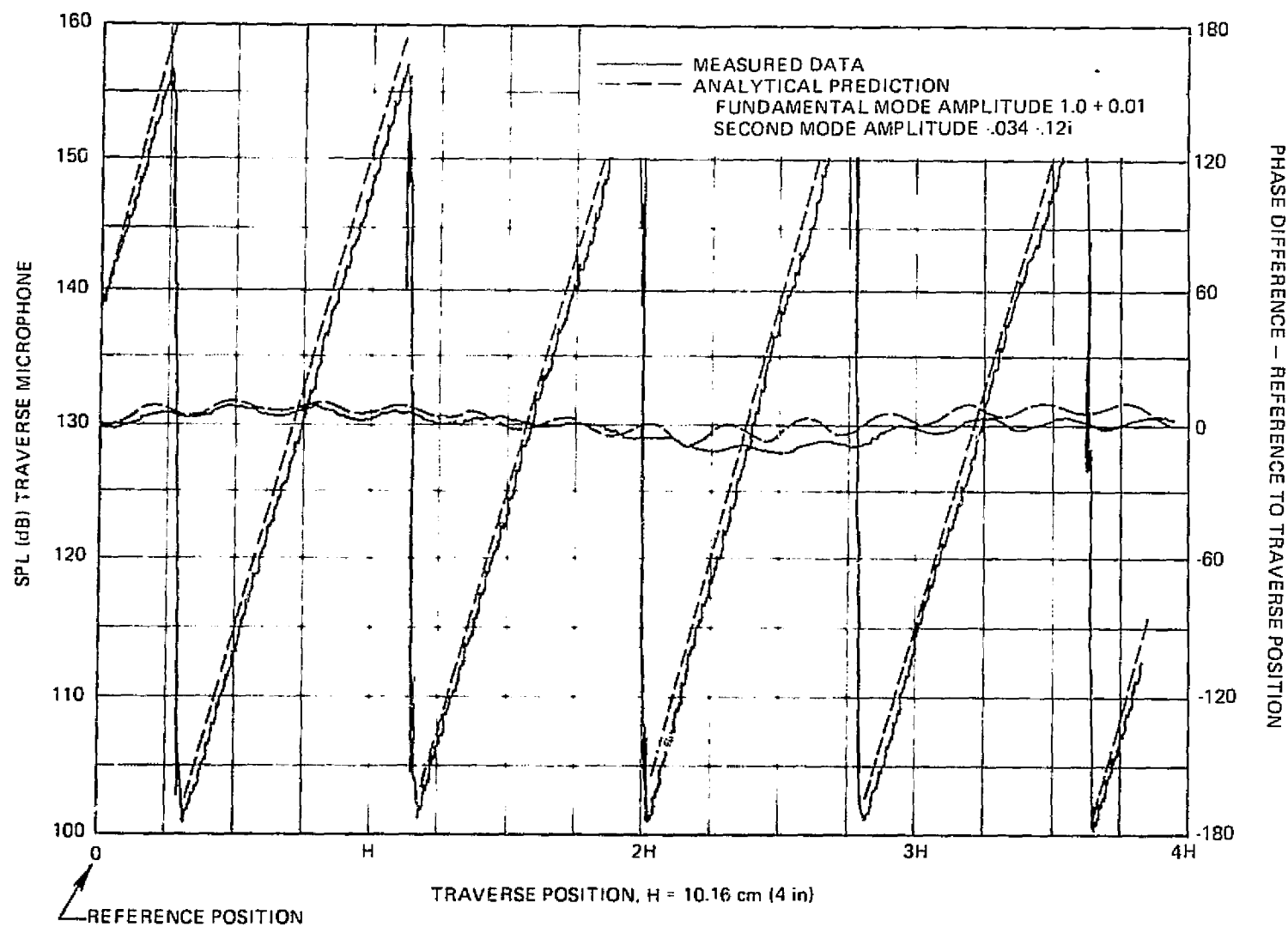
Figure 49. Curve to Experimental Data. Comparison of Measured and Predicted Axial Distribution of Centerline Pressure Magnitude and Phase for Hard-Walled Test Section, kH = 10.16, M = 0.4. Incident Modal Coefficients Varied to Give Best Correlation. Impedance of Soft-Walled Segment Which Models Test Section Termination = ρ c.
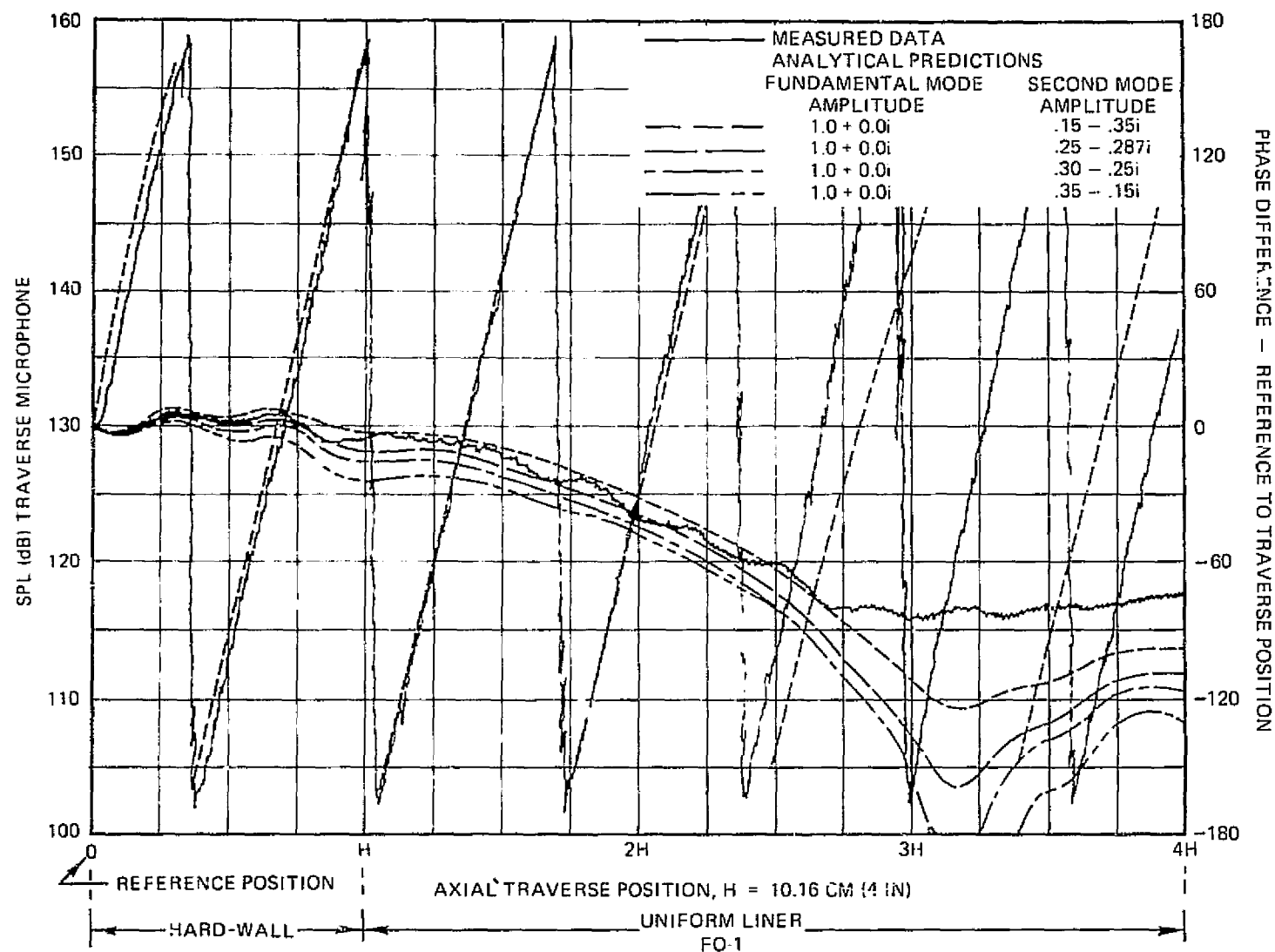
Figure 50: Curve Fit to Experimental Data. Comparison of Measured and Predicted Axial Distribution of Centerline Pressure Magnitude and Phase for Liner Configuration No. 1, kH = 9.6, M = 0.0. Incident Modal Coefficients Varied to Give Better Correlation. Panel Impedances are Specified in Table 8.
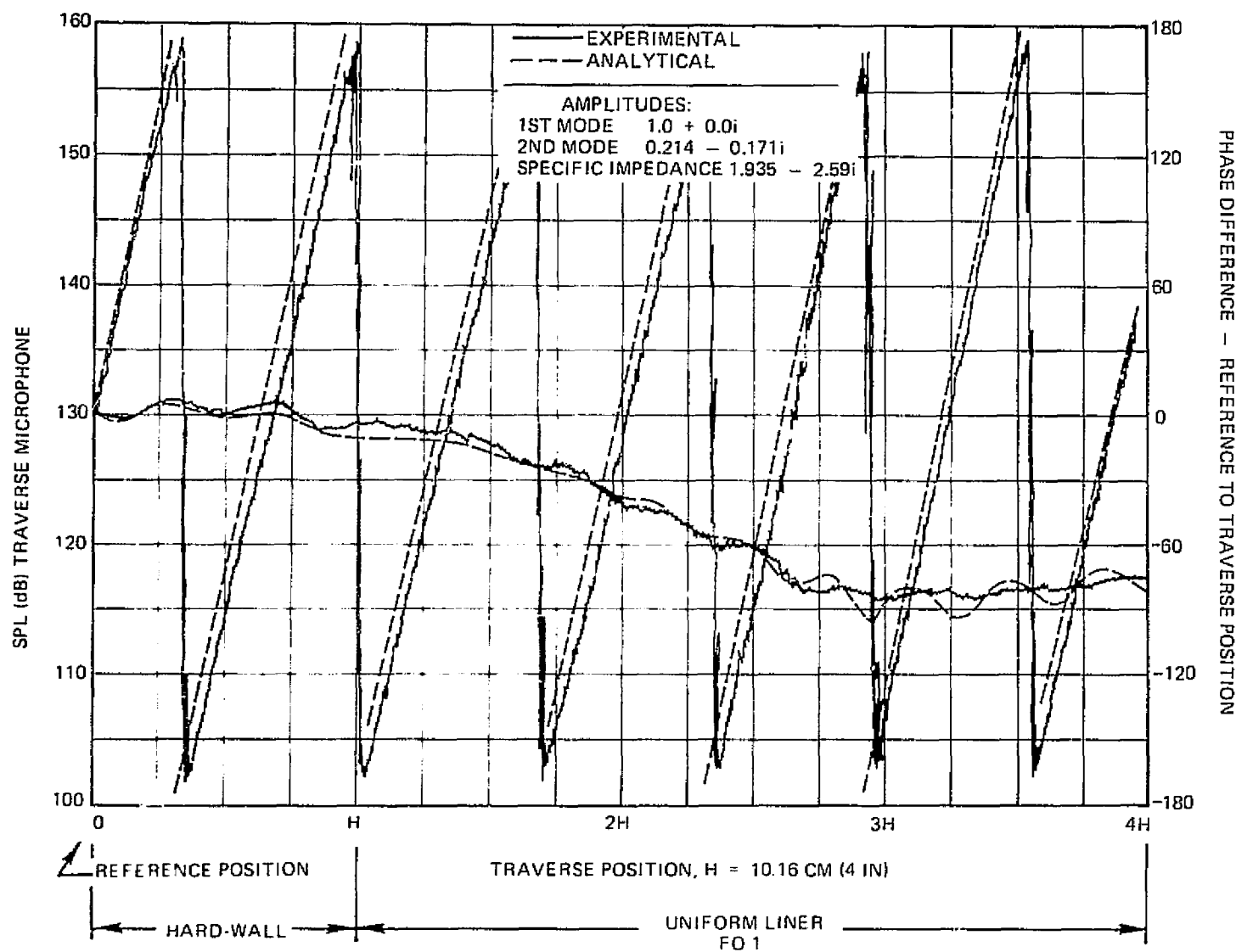
Figure 51: Curve Fit to Experimental Data. Comparison of Measured and Predicted Axial Distribution of Centerline Pressure Magnitude and Phase for Liner Configuration No. 1, kH = 9.6, M = 0.0. Incident Modal Coefficients and Panel Impedance Varied to Give Best Correlation. Impedance of Soft-Walled Segment which Models Test Section Termination = ρc.

precluded running the impedance tube tests, but the improper bonding could allow face sheet motion, which would likely cause an increase in both resistance and reactance. This might explain the larger impedance value required for correlation.

Configuration 3 was also studied by this technique for the kH = 9.6 case (Figure 37). To allow for the nonuniformity in flow resistance measured for the dissipative segment (Figure 24), the two-segment liner was modeled by a three-segment configuration. The resulting correlation is presented in Figure 52 and again is quite good. The impedance values and incident modal content are very reasonable and are well within feasible tolerances. Also, the sound power attenuation of 21.0 dB is the same as that calculated for configuration 3 in Table 7.

Configuration 5 was studied only for a kH of 10.16. Both incident mode content and segment impedance were allowed to vary. The resulting modal content and segment impedance (Table 10) are within reasonable estimates of experimental variations. Comparison with traverse data (Figure 53) shows excellent agreement when the second hard-wall mode is present in the analytical predictions. The change in modal amplitude from that measured in the hard-wall case can be explained by assuming that the presence of the liner in the test section reflects pressure waves toward the source. These waves interact with the source pressure wave patterns causing a change in incident mode content.

In light of excellent results obtained from the optimized modal contents and impedances and the other previously discussed correlations, it is felt that the two-dimensional duct analyses presented herein for the square grazing flow duct are appropriate.

TABLE 10
MODAL COEFFICIENTS AND LINER IMPEDANCES FROM AN OPTIMIZATION
CURVE FIT OF CONFIGURATION 5, kH = 10.16 TRANSVERSE DATA, FIGURE 53

FUNDAMENTAL MODE ALMPLITUDE	$1. + 0.i$
SECOND MODE AMPLITUDE	$-.18 - .11i$
IMPEDANCE FOR LINER NO. 1	$.209 - .822i$
IMPEDANCE FOR LINER NO. 2	$.713 - .561i$
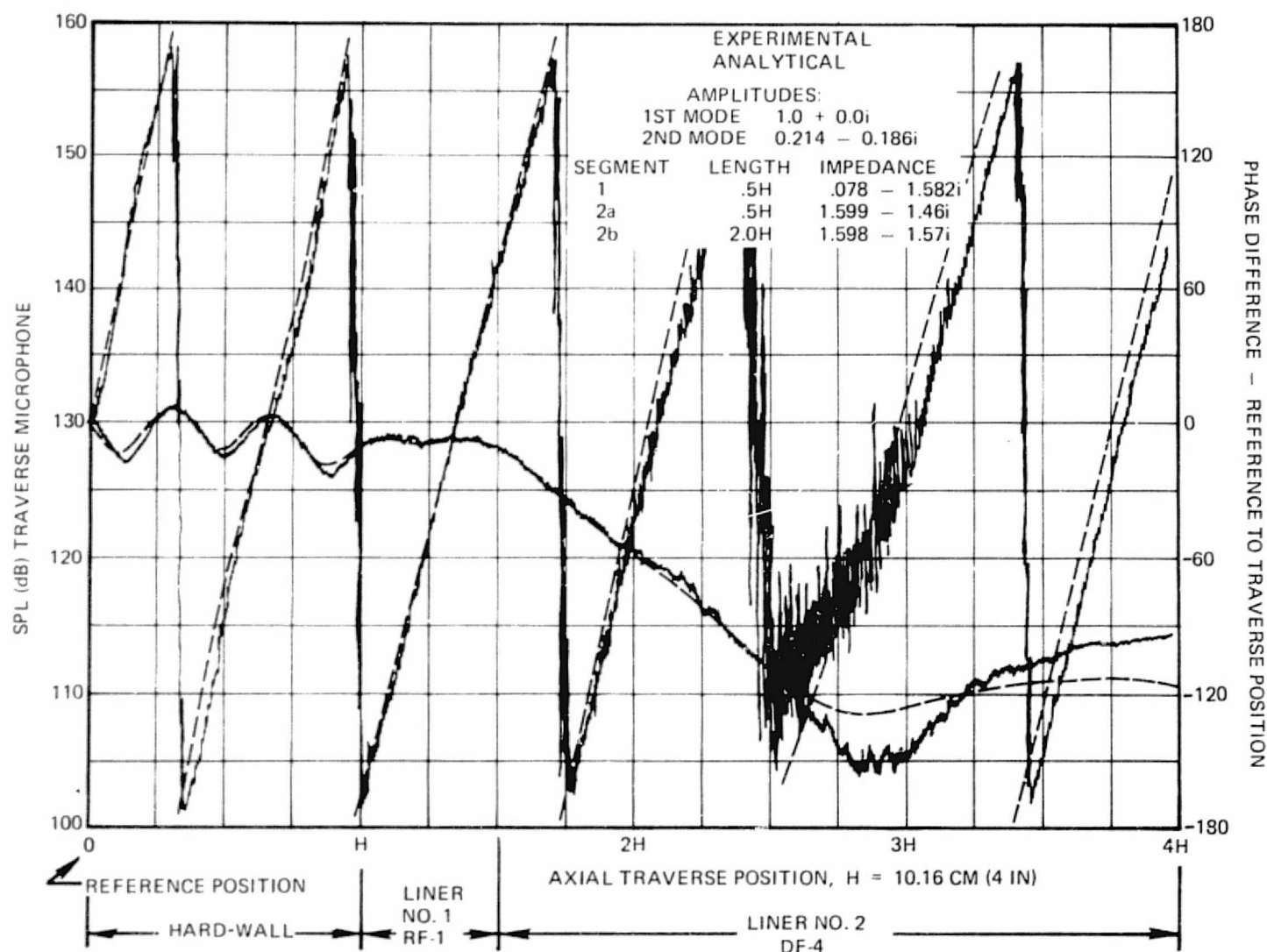
Figure 52: Curve Fit to Experimental Data. Comparison of Measured and Predicted Axial Distribution of Centerline Pressure Magnitude and Phase for Liner Configuration No. 3, kH = 9.6, M = 0.0. Incident Modal Coefficients and Panel Impedance Varied to Give Best Correlation. Impedance of Soft-Walled Segment which Models Test Section Termination = ρc.
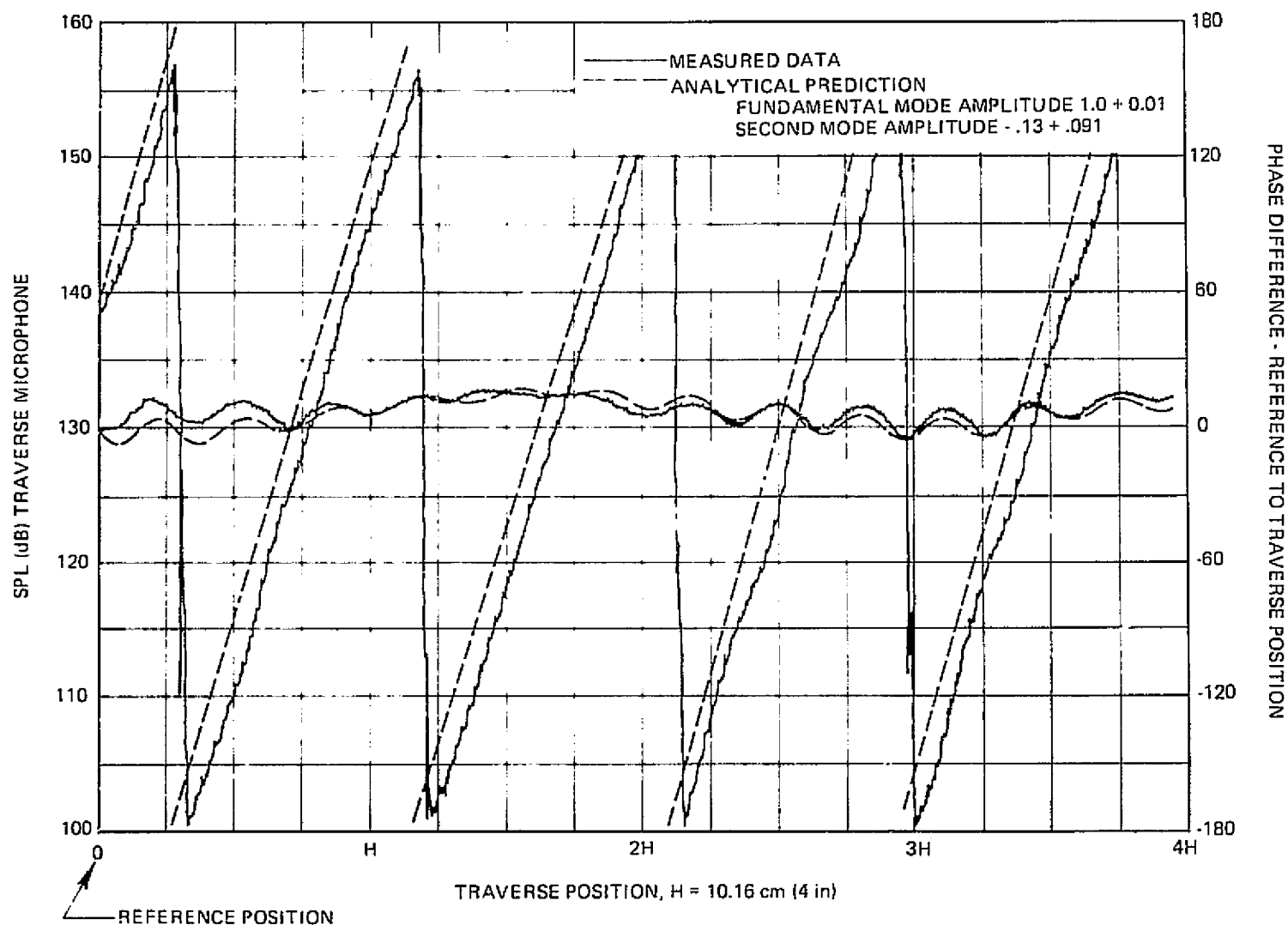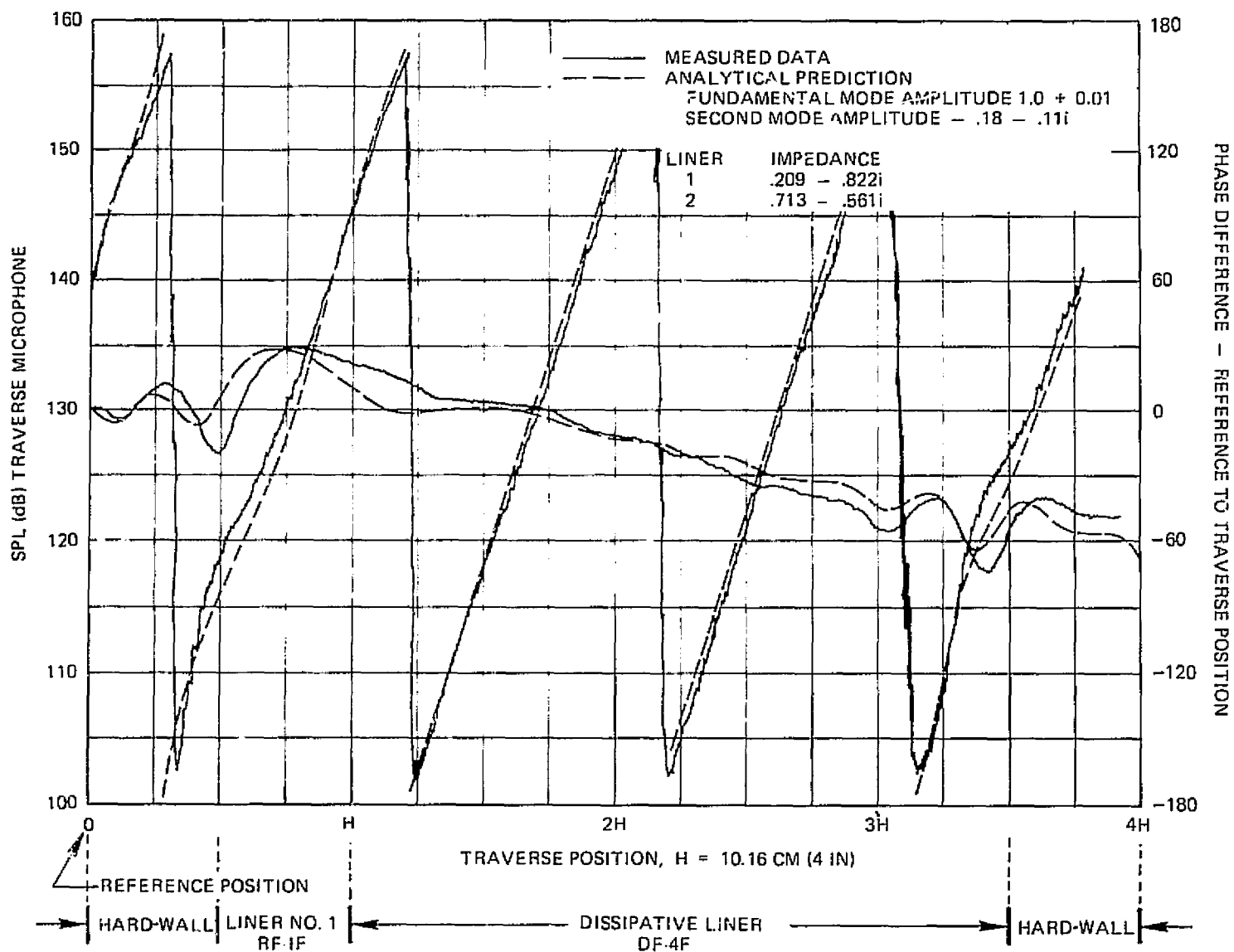
Figure 53: Curve Fit to Experimental Data. Comparison of Measured and Predicted Axial Distribution of Centerline Pressure Magnitude and Phase for Liner Configuration No. 5, kH = 10.16, M = 0.4. Incident Modal Coefficients and Panel Impedance Varied to Give Best Correlation. Impedance of Soft-Walled Segment which Models Test Section Termination = ρc.

CONCLUDING REMARKS

It has been shown that multisegment linings can be designed to yield substantially greater attenuation than is provided by single-segment liners of the same length. Also, although optimal lining configurations vary with the modal content of the incident sound, thus generally requiring accurate specification of the sound source, it was found possible to design a three-segment liner for a specific set of conditions which appeared relatively insensitive to modal content.

It has been found that multisegment liners have "modal conditioning" as their primary mechanism for increased attenuation; the incident sound is redistributed by the front liners into modes which are more readily absorbed by the remaining lining segments. These studies have not shown any significant reflection of sound energy from the multisegment liners (except at a frequency of kH/2 = π, which corresponds to the second hard-wall mode cut-on), even though the semi-infinite hard-walled duct on the input side of the segmented liner would readily allow such reflections. Other investigators [Baumeister (ref. 35), Quinn (ref. 36), Lester and Posey (ref. 38)] are in agreement with the major conclusion regarding the mechanism by which the multisegment liner performance is obtained, even though some of the mathematical models used were quite different from those used in this study.

In addition, a method has been demonstrated for determining duct modal content for cases with only a few modes present. The technique involves varying incident and reflected modal coefficients to fit measured axial pressure phase and magnitude information. The use of axial traverse data for modal identification in a uniform flow avoids the problems associated with the flow and acoustic interference of a transverse probe extended into the duct.

Of particular importance is the fact that it was possible to design, build, and demonstrate multisegment liners in the presence of such practical constraints as uncertainty regarding the details of the sound source modal structure and the requirement that liners be built up from materials in stock. (Note that these liners are thus constrained optimums and do not necessarily represent the overall optimum liner which might be produced if these constraints could be relaxed.)

The results of this investigation indicate that the present phased liner theory could be of immediate benefit in aircraft applications, particularly to problems of exhaust duct noise suppression. However, adaptation to the design of inlet liners will require that several remaining questions be answered. These include the following:

- Can practical phased liners be developed for cases in which large number of modes, including spinning modes, are present?

- How would the presence of sheared mean flow, which affects upstream and downstream moving modes differently, change the effectiveness and behavior of multisegment liners?

- Could the optimization procedure be improved by considering only right moving modes in longer, highly dissipative segments, and retaining both right and left moving systems in the short and low resistance segments?

- How well can broadband noise be attenuated? That is, can performance be optimized over a finite width frequency band, as well as over model content, liner length, etc.?

APPENDIX A

DEFINITION OF PROPAGATION CONSTANTS

The propagation constant is defined as

$$\lambda = -kM/(1 - M^2) \pm k \left[1 - (\mu/k)^2(1 - M^2)\right]^{1/2}/(1 - M^2) \tag{A1}$$

The appropriate sign on the square root term must be chosen to designate right and left moving modes.

Soft-Walled Duct (μ Complex)

For this case, since μ is complex, define

$$\left[1 - (\mu/k)^2 (1 - M^2)\right]^{1/2} = \alpha + i\beta, \quad \beta > 0 \tag{A2}$$

Then the axial dependence is obtained by use of (A1), (A2), and equation (5):

$$\exp\left[ikM/(1 - M^2) \mp i\alpha k/(1 - M^2) \pm \beta k/(1 - M^2)\right] \tag{A3}$$

To ensure attenuation of the soft-wall modes, take the minus sign for right moving modes and the plus sign for left moving modes.

Hard-Walled Duct (μ Real)

Suppose first that $(\mu/k)^2 > \dfrac{1}{1 - M^2}$. Then (A1) becomes

$$\lambda = -kM/(1 - M^2) \pm ik \left[(\mu/k)^2 (1 - M^2) - 1\right]^{1/2} \tag{A4}$$

and the axial dependence is

$$\exp\left\{ikM/(1 - M^2) \pm k \left[(\mu/k)^2 (1 - M^2) - 1\right]^{1/2}/(1 - M^2)\right\} \tag{A5}$$

Thus, for right and left moving waves, we choose the minus and plus signs, respectively, in order to obtain attenuation of the mode as it propagates away from the source.

For $(\mu/k)^2 < 1.0$, λ is real and the direction of propagation cannot be determined by attenuation direction. For this case,

$$\lambda = -kM(-M \pm \xi)/(1 - M^2) \tag{A6}$$

where $\xi = [1 - (\mu/k)^2 (1 - M^2)]^{1/2} > M$

Now $e^{i\omega t - i\lambda z} = e^{i\omega(t - z/V_{Phase})}$ and for wavelike behavior

$$V_{Phase} = \omega/\lambda = \begin{cases} (1 - M^2) c/(\xi - M) \\ -(1 - M^2) c/(\xi + M) \end{cases} \tag{A7}$$

Thus the plus sign corresponds to right moving and the minus sign to left moving propagation.

Finally, consider $1.0 \leq (\mu/k)^2 \leq \dfrac{1}{1 - M^2}$. For this case $0 < \xi^2 < M^2$ thus

$$\lambda = k(-M \pm \xi)/(1 - M^2) \qquad \text{where} \quad 0 < \xi < M \tag{A8}$$

This yields two negative phase speeds for $M > 0$

$$\lambda = -k(M \mp \xi)/(1 - M^2) \tag{A9}$$

and two positive phase speeds for $M < 0$

$$\lambda = k(|M| \pm \xi)/(1 - M^2) \tag{A10}$$

Eversman (Reference 39) has shown by energy considerations that the smallest absolute value of λ corresponds to downstream propagation and the largest to upstream transmission.

The resulting definitions of flow duct modal propagation constants are summarized in Table 2.

APPENDIX B

NUMERICAL INTEGRATION TECHNIQUE FOR EIGENVALUE COMPUTATION

This method or similar methods have been used by Rice (ref. 5) and Zorumski and Mason (ref. 4).

The eigenvalue equation for symmetric flow duct modes may be written

$$D = \mu H \sin(\mu H/2)/2 - ikH\overline{A} \cos(\mu H/2)/2 = 0 \tag{B1}$$

The total differential of D is

$$dD = (\partial D/\partial \mu) \, d\mu + (\partial D/\partial \overline{A}) \, d\overline{A} = 0 \tag{B2}$$

The total differential vanishes because D is identically zero. This equation may be solved for $d\mu/d\overline{A}$:

$$d\mu/d\overline{A} = (\partial D/\partial \overline{A})/(\partial D/\partial \mu) = f(\mu, \overline{A})$$

$$= ikH/[(1 + ikH\overline{A}) \tan(\mu H/2) + \mu H] \tag{B3}$$

This equation may be integrated from $\overline{A} = 0$ to the true softwall value of $\overline{A}$ using, for example, the Runge-Kutta integration procedure

$$\mu(\overline{A} + \delta\overline{A}) = \mu(\overline{A}) + [K_1 + 2(K_2 + K_3) + K_4]/6$$

$$K_1 = \delta\overline{A} \, f(\mu, \overline{A})$$

$$K_2 = \delta\overline{A} \, f(\mu + K_1/2, \overline{A} + \delta\overline{A}/2) \tag{B4}$$

$$K_3 = \delta\overline{A} \, f(\mu + K_2/2, \overline{A} + \delta\overline{A}/2)$$

$$K_4 = \delta\overline{A} \, f(\mu + K_3, \overline{A} + \delta\overline{A})$$

Note that for $\overline{A} = 0$, $\mu = 2n\pi/H$, n is an integer. For n = 0, the differential equation is singular. Thus, for the plane wave mode, the integration must be begun at $\mu(\delta\overline{A})$, which may be obtained by an asymptotic expansion of (B1) for small admittance or by Newton-Raphson iteration on (B1). It should also be noted that, at an optimum Cremer impedance, the quantity $\partial D/\partial \mu$ vanishes

(see Appendix D). This method would thus fail if the integration path was to pass through one of these singular points. This possibility could be taken into account in the computational algorithm, but would involve considerable program complexity. In experience to date with this program, it has been found that the chance of passing through a singular point is rather remote and so the program has not been modified.

APPENDIX C

RAYLEIGH-RITZ TECHNIQUE FOR EIGENVALUE COMPUTATION

The functional

$$I = \int_0^R \{(p_y{}^2 - [(1 - \lambda M_0)^2 - \lambda^2] \, p^2\} \, dy + i\overline{A}(1 - \lambda M_0)^2 \, p^2 \, (y = H/2) \tag{C1}$$

has stationary conditions

$$p_{yy} + [(1 - \lambda M_0)^2 - \lambda^2] \, P = 0$$

$$p_y \, (y = H/2) + iA \, (1 - \lambda M_0)^2 \, P \, (y = H/2) = 0 \tag{C2}$$

$$p_y \, (y = 0) = 0$$

By expanding p in terms of functions which have the capability of satisfying (C2), and requiring that I be stationary with respect to the undetermined expansion coefficients, a linear algebraic eigenvalue problem in λ^2 can be obtained:

$$\left[[-B]^{-1} \, [A] - \lambda^2 \, [I] \right] \quad \{a_n\} = \{0\} \tag{C3}$$

For an expansion $p = \sum_{m=0}^{N-1} a_n \cos(n\pi y/H)$, for example, the requirement that $\partial I / \partial a_\ell = 0$ for $\ell = 0, (1), N - 1$ leads to the following definitions for the matrices in (C3):

$$[A] = \left[\int_0^R (nm\pi^2/H^2) \sin(n\pi y/H) \sin(m\pi y/H) \, dy \right.$$

$$\left. - \int_0^R \cos(n\pi y/H) \cos(m\pi y/H) dy + i\overline{A} \cos(n\pi/2) \cos(m\pi/2) \right] \tag{C4}$$

$$[-B] = \left[- \int_0^R \cos(n\pi y/H) \cos(m\pi y/H) \, dy \right]$$

Equation (C3) can be solved by any standard eigenvalue package.

APPENDIX D

MULTIPLE EIGENVALUES AND CREMER OPTIMUM ADMITTANCES

Tester (ref. 3) and Zorumski and Mason (ref. 4) have presented extensive studies of the Cremer optimum liner and have shown that the optimum admittance for a given mode pair is that which causes the modes to coalesce. The conditions for multiplicity of the eigenvalues are:

$$D = \mu H \sin(\mu H/2) - ikH\overline{A}\cos(\mu H/2) = 0 \tag{D1}$$

$$\partial D/\partial\mu = (1 + ikH\overline{A}/2)\sin(\mu H/2) + \mu H\cos(\mu H/2)/2 = 0$$

or

$$\sin(\mu H) + \mu H = 0 \tag{D2}$$

Suppose $\mu = \alpha + i\beta$, then (D2) becomes

$$\alpha H + \sin(\alpha H)\cosh(\beta H) = 0 \tag{D3}$$

$$\beta H + \cos(\alpha H)\sinh(\beta H) = 0$$

Tester (ref. 3) has shown that for sufficiently high eigenvalues $\beta/\alpha \rightarrow 0$. Thus, for $\beta \gg \alpha$

$$\beta/\alpha = -\cot(\alpha H)\tanh(\beta H) \rightarrow 0 \tag{D4}$$

But since $\tanh(\beta H) \rightarrow 1.0$ for β large, (D4) becomes $-\cot(\alpha H) \rightarrow 0$ or
$$\alpha H = m\pi + \pi/2, \text{ m large integer} \tag{D5}$$

Note that $\sin(m\pi + \pi/2) = -1^m$ and thus (D3) becomes

$$m\pi + \pi/2 + (-1)^m\cosh(\beta H) = 0 \tag{D6}$$

But $\cosh > 0$ for all (βH) thus

$$m\pi + \pi/2 = -(-1)^m|\cosh(\beta H)| \tag{D7}$$

87

which implies that m must be odd, or $m = 2\ell + 1$, thus

$$\alpha H = 2\ell\pi + 3\pi/2 \tag{D8}$$

and

$$\beta H \quad = \quad \cosh^{-1}(2\ell\pi + 3\pi/2)$$

$$\equiv \quad \text{Log}_e \; [2\ell\pi + 3\pi/2 + \sqrt{(2\ell\pi - 3\pi/2)^2 - i}] \tag{D9}$$

$$\approx \quad \text{Log}_e \; [(2\ell\pi + 3\pi/2) \;\; + \;\; (2\ell\pi + 3\pi/2)]$$

for large ℓ

$$\therefore \; \mu H/2 = (\ell\pi + 3\pi/4) + i[\text{Log}_e(4\ell\pi + 3\pi)]/2 \tag{D10}$$

The optimum admittance is thus

$$\overline{A} \quad = \quad 2i\left\{\tfrac{1}{2} \mp \left[\tfrac{1}{4} - (\mu H/2)^2\right]^{\tfrac{1}{2}}\right\}/kH \tag{D11}$$

Where $\mp$ is chosen by the condition that $\text{Re}(\overline{A}) > 0$.

INTERFACE MATCHING EQUATIONS

Equations for the first interface:

Equal pressure

$$A_m b_m^0 - \sum_{n=0}^{N_1-1} a_n^1 \left[(1/2)\overrightarrow{\mu}_n^1 H^2 (-1)^m \sin(\overrightarrow{\mu}_n^1 H/2)\right] / \left[(\overrightarrow{\mu}_n^1)^2 - (m\pi)^2\right]$$

$$-\sum_{n=0}^{n_1-1} b_n^1 \left[(1/2)\overleftarrow{\mu}_n^1 H^2 (-1)^m \sin(\overleftarrow{\mu}_n^1 H/2)\right] e^{i\overleftarrow{\lambda}_n^1 L_1} / \left[(\overleftarrow{\mu}_n^1)^2 - (m\pi)^2\right] = -A_m a_m^0 , \tag{E1}$$

$$m=0, (1), N_0 - 1$$

Equal Velocity

$$\sum_{n=0}^{N_0-1} b_n^0 \overleftarrow{\lambda}_n^0 \left[(1/2)\overrightarrow{\mu}_m^1 H^2 (-1)^m \sin(\overrightarrow{\mu}_m^1 H/2)\right] / \left\{(1-\overleftarrow{\lambda}_n^0 M/k)\left[(\overrightarrow{\mu}_n^1)^2 - (n\pi)^2\right]\right\}$$

$$-\sum_{n=0}^{N_1-1} a_n^1 \overrightarrow{\lambda}_n^1 B_{mn} / (1-\overrightarrow{\lambda}_n^1 Mk)$$

$$-\sum_{n=0}^{N_1-1} b_n^1 \overleftarrow{\lambda}_n^1 e^{i\overleftarrow{\lambda}_n^1 L_1} \left[2\cos(\mu_n^1 H/2)\cos(\overrightarrow{\mu}_m^1 H/2)\right]\left[\overleftarrow{\mu}_m^1 \tan(\overleftarrow{\mu}_n^1 H/2)\right. \tag{E2}$$

$$\left. -\overrightarrow{\mu}_m^1 \tan(\overrightarrow{\mu}_m^1 H/2)\right] / \left\{1-\overleftarrow{\lambda}_n^1 M/k)\left[(\overleftarrow{\mu}_n^1)^2 - (\overrightarrow{\mu}_m^1)^2\right]\right\}$$

$$= -\sum^{N_0-1} a_n^0 \overrightarrow{\lambda}_n^0 \left[(1/2)\overrightarrow{\mu}_m^1 H^2 (-1)^n \sin(\overrightarrow{\mu}_m^1 H/2)\right] / \left\{(1-\overrightarrow{\lambda}_n^0 M/k)\left[(\overrightarrow{\mu}_m^1)^2 - (n\pi)^2\right]\right\},$$

$$m=0, (1), N_1 - 1$$

Where

$$A_m = \begin{cases} H, & m=0 \\ H/2, & m>0 \end{cases}$$

$$B_{mn} = \begin{cases} \dfrac{2\cos(\overrightarrow{\mu}_n^1 H/2)\cos(\overrightarrow{\mu}_m^1 H/2)\left[\overrightarrow{\mu}_n^1 \tan(\overrightarrow{\mu}_n^1 H/2)-\overrightarrow{\mu}_m^1 \tan(\overrightarrow{\mu}_m^1 H/2)\right]}{\left[(\overrightarrow{\mu}_n^1)^2 - (\overrightarrow{\mu}_m^1)^2\right]}, & m \neq n \\[2em] H/2 + \sin(\overrightarrow{\mu}_m^1 H / (2\overrightarrow{\mu}_m^1) , & m=n \end{cases}$$

Equations for intermediate interface:

Equal Pressure

$$\sum_{n=0}^{N_j-1} a_n^j \left[2\cos(\overrightarrow{\mu}_n^j H/2)\cos(\overleftarrow{\mu}_m^{j-1} H/2)\right]\left[\overrightarrow{\mu}_n^j \tan(\overrightarrow{\mu}_n^j H/2) - \overleftarrow{\mu}_m^{j-1}\tan(\overleftarrow{\mu}_m^{j-1}H/2)\right]/\left[(\overrightarrow{\mu}_n^j)^2 - (\overleftarrow{\mu}_m^{j-1})^2\right]$$

$$-\sum_{n=0}^{N_j-1} b_n^j e^{i\overleftarrow{\lambda}_n^j L_j}\left[2\cos(\overleftarrow{\mu}_n^j H/2)\cos(\overleftarrow{\mu}_m^{j-1}H/2)\right]\left[\overleftarrow{\mu}_n^j \tan(\overleftarrow{\mu}_n^j H/2\right.$$

$$\left.-\overleftarrow{\mu}_m^{j-1}\tan(\overleftarrow{\mu}_m^{j-1}H/2)\right]/\left[(\overrightarrow{\mu}_n^j)^2 - (\overleftarrow{\mu}_m^{j-1})^2\right] = 0, \quad m = 0, (1), N_{j-1} - 1 \tag{E3}$$

Equal Velocity

$$\sum_{n=0}^{N_{j-1}-1} a_n^{j-1}\overrightarrow{\lambda}_n^{j-1} e^{i\overrightarrow{\lambda}_n^{j-1} L_{j-1}}\left[2\cos(\overrightarrow{\mu}_n^{j-1} H/2)\cos(\overrightarrow{\mu}_m^j H/2)\right]\left[\overrightarrow{\mu}_n^{j-1}\tan(\overrightarrow{\mu}_n^{j-1}H/2)-\overrightarrow{\mu}_m^j\tan(\overrightarrow{\mu}_m^j H/2)\right]/\{(1-\overrightarrow{\lambda}_n^{j-1}M/k)$$

$$\left[(\overrightarrow{\mu}_n^{j-1})^2 - (\overrightarrow{\mu}_m^j)^2\right]\} + \sum_{n=0}^{N_j-1} b_n^{j-1}\overleftarrow{\lambda}_n^{j-1}\left[2\cos(\overleftarrow{\mu}_n^{j-1}H/2)\cos(\overrightarrow{\mu}_m^j H/2)\right]\left[\overleftarrow{\mu}_n^{j-1}\tan(\overleftarrow{\mu}_n^{j-1}H/2)-\overrightarrow{\mu}_m^j\tan(\overrightarrow{\mu}_m^j H/2)\right]/$$

$$\{(1-\overleftarrow{\lambda}_n^{j-1}M/k)\left[(\overleftarrow{\mu}_n^{j-1})^2-(\overrightarrow{\mu}_m^j)^2\right]\} - \sum_{n=0}^{N_j-1} a_n^j \overrightarrow{\lambda}_n^j B_{mn}/(1-\overrightarrow{\lambda}_n^j M/k)-$$

$$\sum_{n=0}^{N_j-1} b_n^j \overleftarrow{\lambda}_n^j e^{i\overleftarrow{\lambda}_n^j L_j}\left[2\cos(\overleftarrow{\mu}_n^j H/2)\cos(\overrightarrow{\mu}_m^j H/2)\right]\left[\overleftarrow{\mu}_n^j \tan(\overleftarrow{\mu}_n^j H/2)-\overrightarrow{\mu}_m^j\tan(\overrightarrow{\mu}_m^j H/2)\right]/ \tag{E4}$$

$$(1-\overleftarrow{\lambda}_n^j M/k)\left[(\overleftarrow{\mu}_n^j)^2-(\overrightarrow{\mu}_m^j)^2\right]\} = 0, \quad m = 0, (1), N_j - 1$$

Where

$$B_{mn} = \begin{cases} \dfrac{2\cos(\overleftarrow{\mu}_n^{j-1}H/2)\cos(\overleftarrow{\mu}_m^{j-1}H/2)\left[\overleftarrow{\mu}_n^{j-1}\tan(\overleftarrow{\mu}_n^{j-1}H/2)-\overleftarrow{\mu}_m^{j-1}\tan(\overleftarrow{\mu}_m^{j-1}H/2)\right]}{(\overleftarrow{\mu}_n^{j-1})^2 - (\overleftarrow{\mu}_m^{j-1})^2}, & m \neq n \\[2em] H/2 + \sin(\overleftarrow{\mu}_m^{j-1}H/2)/(2\overleftarrow{\mu}_m^{j-1}), & m = n \end{cases}$$

90

Equations for final interface:

Equal Pressure

$$\sum_{n=0}^{N_{J-2}-1} a_n^{J-2}\ e^{i\lambda_n^{j-1}L_{j-2}}\ \left[2\cos(\vec{\mu}_n^{J-2}H/2)\cos(\overleftarrow{\mu}_m^{J-2}H/2)\right]\left[\vec{\mu}_n^{J-2}\tan(\vec{\mu}_n^{J-2}H/2)-\overleftarrow{\mu}_m^{J-2}\tan(\overleftarrow{\mu}_m^{J-2}H/2)\right]/$$

$$\left[(\vec{\mu}_n^{J-2})^2-(\overleftarrow{\mu}_m^{J-2})^2\right] + \sum_{n=0}^{N_{J-2}-1} b_n^{J-2}B_{mn} - \sum_{n=0}^{N_{J-1}-1} a_{,n}^{J-1}\left[(1/2)\overleftarrow{\mu}_m^{J-2}H^2(-1)^n\sin(\overleftarrow{\mu}_m^{J-2}H/2)\right]/ \tag{E5}$$

$$\left[(\overleftarrow{\mu}_m^{J-2})^2-(n\pi)^2\right]=0,\ m=0,\ (1),\ N_{J-2}-1$$

Equal Velocity

$$\sum_{n=0}^{N_{J-2}-1} a_n^{J-2}\ \vec{\lambda}_n^{J-2}\ e^{i\vec{\lambda}_n^{J-2}L_{J-2}}\ \left[(1/2)\vec{\mu}_n^{J-2}H^2(-1)^m\sin(\vec{\mu}_n^{J-2}H/2)\right]/\left\{(1-\vec{\lambda}_n^{J-2}M/k)\left[(\vec{\mu}_n^{J-2})^2-(m\pi)^2\right]\right\}$$

$$+\sum_{n=0}^{N_{J-2}-1} b_n^{J-2}\ \overleftarrow{\lambda}_n^{J-2}\ \left[(1/2)\overleftarrow{\mu}_n^{J-2}H^2(-1)^m\sin(\overleftarrow{\mu}_n^{J-2}H/2)\right]/\left\{(1-\overleftarrow{\lambda}_n^{J-2}M/k)\left[(\overleftarrow{\mu}_n^{J-2})^2-(m\pi)^2\right]\right\}$$

$$\tag{E6}$$

$$-a_m^{J-1}\ \vec{\lambda}_m^{J-1}\ A_m/(1-\vec{\lambda}_m^{J-1}M/k)=0,\ \ m=0,\ (1),\ N_{J-1}-1$$

Where

$$A_m = \begin{cases} H, & m=0 \\ H/2, & m>0 \end{cases}$$

APPENDIX F

TERMINATION EQUATIONS

Suppose the duct termination to contain an arbitrary nonuniformity between the last soft-walled segment and the final semi-infinite hard-walled duct. Then the acoustic field in the last hard-walled uniform segment can be written in terms of the "reflection coefficient" matrix for the nonuniformity. Begin, for example, by writing the acoustic field in the nonuniform section in terms of right moving and left moving wave systems

$$p^* = \sum_n a_n^* \Phi_n(y,z) + \sum_n b_n^* \psi_n(y,z)$$

$$w^* = \sum_n a_n^* \zeta_n(y,z) + \sum_n b_n^* \xi_n(y,z)$$

(F1)

where the asterisk denotes the nonuniformity. By equating pressure and velocities on the outlet side of the nonuniformity equations for the unknown coefficients can be written as:

$$[A]\{a_n^*\} + [B]\{b_n^*\} = [C]\{a_n^{J-1}\}$$

$$[D]\{a_n^*\} + [E]\{b_n^*\} = [F]\{a_n^{J-1}\}$$

(F2)

where the a_n^{J-1} are the coefficients of the transmitted hardwall modes. The a_n^{J-1} may be eliminated from equation (F2):

$$\left[[A] - [C][F]^{-1}[D]\right]\{a_n^*\} + \left[[B] - [C][F]^{-1}[E]\right]\{b_n^*\} = \{0\}$$

$$\text{or } [\alpha]\{a_n^*\} + [\beta]\{b_n^*\} = \{0\}$$

(F3)

Next, equate pressures and velocities on the inlet side to obtain:

$$[Q]\{a_n^{J-2}\} + [R]\{b_n^{J-2}\} = [S]\{a_n^*\} + [T]\{b_n^*\}$$

$$[W]\{a_n^{J-2}\} + [X]\{b_n^{J-2}\} = [Y]\{a_n^*\} + [Z]\{b_n^*\}$$

(F4)

Using (F3):

$$[Q]\{a_n^{J-2}\} + [R]\{b_n^{J-2}\} = \left[[T] - [S][\alpha]^{-1}[\beta]\right]\{b_n^*\}$$

$$= [\mathcal{T}]\{b_n^*\}$$

(F5)

PRECEDING PAGE BLANK NOT FILMED

$$[W]\{a_n^{J-2}\}+[X]\{b_n^{J-2}\}=\Big[[Z]-[Y][\alpha]^{-1}[\beta]\Big]\{b_n^*\}$$

$$=[\gamma]\{b_n^*\}$$

(F6)

from which the b_n^* can be eliminated:

$$\Big[[W]-[\gamma][\mathcal{G}]^{-1}[Q]\Big]\{a_n^{J-2}\}+\Big[[X]-[\gamma][\mathcal{G}]^{-1}[R]\Big]\{b_n^{J-2}\}=\{0\}$$

(F7)

or

$$\{b_n^{J-2}\}=-[X]^{-1}[\omega]\{a_n^{J-2}\}=[\mathcal{R}]\{a_n^{J-2}\}$$

(F8)

$$[\mathcal{R}]\{a_n^{J-2}\}-[I]\{b_n^{J-2}\}=\{0\}$$

where $[\mathcal{R}]$ is the reflection coefficient matrix, which can be derived separately from the segmented duct analysis and input directly. Typical methods for obtaining $[\mathcal{R}]$ may be found in refs. 7-12 and 24-25.

APPENDIX G

ENERGY FLUX EXPRESSIONS

Incident in Hard-Walled Duct

$$\Pi_a = \frac{1}{2\rho C}\sum_{m=0}^{N_0-1} A_m \left\{ a_m^0 a_m^{0*}\left[(1+M^2)\text{REAL}\left(\frac{\overrightarrow{\lambda}_m^0/k}{1-\overrightarrow{\lambda}_m^0 M/k}\right)+M\right.\right.$$

$$+M\left(\frac{\overrightarrow{\lambda}_m^0/k}{1-\overrightarrow{\lambda}_m^0 M/k}\right)\left(\frac{\overrightarrow{\lambda}_m^0/k}{1-\overrightarrow{\lambda}_m^0 M/k}\right)^*\right] + b_m^0 b_m^{0*}\left[(1+M^2)\text{REAL}\left(\frac{\overleftarrow{\lambda}_m^0/k}{1-\overleftarrow{\lambda}_m^0 M/k}\right)+M\right.$$

$$+M\left(\frac{\overleftarrow{\lambda}_m^0/k}{1-\overleftarrow{\lambda}_m^0 M/k}\right)\left(\frac{\overleftarrow{\lambda}_m^0/k}{1-\overleftarrow{\lambda}_m^0 M/k}\right)^*\right] + \text{REAL}\left(\left[a_m^0 b_m^{0*}\right]\left[(1+M^2)\left(\frac{\overleftarrow{\lambda}_m^0/k}{1-\overleftarrow{\lambda}_m^0 M/k}\right)^*\right.\right.$$

$$\left.+M+M\left(\frac{\overrightarrow{\lambda}_m^0/k}{1-\overrightarrow{\lambda}_m^0 M/k}\right)\left(\frac{\overleftarrow{\lambda}_m^0/k}{1-\overleftarrow{\lambda}_m^0 M/k}\right)^*\right]\right) + \text{REAL}\left(\left[a_m^0 b_m^{0*}\right]\left[(1+M^2)\left(\frac{\overrightarrow{\lambda}_m^0/k}{1-\overrightarrow{\lambda}_m^0 M/k}\right)^*\right.\right.$$

$$\left.\left.\left.+M+M\left(\frac{\overleftarrow{\lambda}_m^0/k}{1-\overleftarrow{\lambda}_m^0 M/k}\right)\left(\frac{\overrightarrow{\lambda}_m^0/k}{1-\overrightarrow{\lambda}_m^0 M/k}\right)^*\right]\right)\right\}$$

(G1)

$$\Pi_b = \frac{1}{2\rho C}\sum_{m=0}^{N_0-1} A_m \left\{ a_m^0 a_m^{0*}\left[\text{REAL}\left(\frac{\overrightarrow{\lambda}_m^0/k}{1-\overrightarrow{\lambda}_m^0 M/k}\right)^* + \frac{M}{2} + \frac{M}{2}\left(\frac{\overrightarrow{\lambda}_m^0/k}{1-\overrightarrow{\lambda}_m^0 M/k}\right)\left(\frac{\overrightarrow{\lambda}_m^0/k}{1-\overrightarrow{\lambda}_m^0 M/k}\right)^*\right.\right.$$

$$+\frac{C_m}{A_m}\frac{M}{2}\left(\frac{2m\pi/kH}{1-\overrightarrow{\lambda}_m^0 M/k}\right)\left(\frac{2m\pi/kH}{1-\overrightarrow{\lambda}_m^0 M/k}\right)^*\right] + b_m^0 b_m^{0*}\left[\text{REAL}\left(\frac{\overleftarrow{\lambda}_m^0/k}{1-\overleftarrow{\lambda}_m^0 M/k}\right)^* + \frac{M}{2}\right.$$

$$+\frac{M}{2}\left(\frac{\overleftarrow{\lambda}_m^0/k}{1-\overleftarrow{\lambda}_m^0 M/k}\right)\left(\frac{\overleftarrow{\lambda}_m^0/k}{1-\overleftarrow{\lambda}_m^0 M/k}\right)^* + \frac{C_m}{A_m}\frac{M}{2}\left(\frac{2m\pi/kH}{1-\overleftarrow{\lambda}_m^0 M/k}\right)\left(\frac{2m\pi/kH}{1-\overleftarrow{\lambda}_m^0 M/k}\right)^*\right]$$

$$+\text{REAL}\left(a_m^0 b_m^{0*}\left[\left(\frac{\overleftarrow{\lambda}_m^0/k}{1-\overleftarrow{\lambda}_m^0 M/k}\right)^* + \frac{M}{2} + \frac{M}{2}\left(\frac{\overrightarrow{\lambda}_m^0/k}{1-\overrightarrow{\lambda}_m^0 M/k}\right)\left(\frac{\overleftarrow{\lambda}_m^0/k}{1-\overleftarrow{\lambda}_m^0 M/k}\right)\right.\right.$$

$$\left.+\frac{C_m}{A_m}\frac{M}{2}\left(\frac{2m\pi/kH}{1-\overrightarrow{\lambda}_m^0 M/k}\right)\left(\frac{2m\pi/kH}{1-\overleftarrow{\lambda}_m^0 M/k}\right)^*\right]\right) + \text{REAL}\left(a_m^{0*} b_m^0\left[\left(\frac{\overrightarrow{\lambda}_m^0/k}{1-\overrightarrow{\lambda}_m^0 M/k}\right)^* + \frac{M}{2}\right.\right.$$

$$\left.\left.\left.+\frac{M}{2}\left(\frac{\overleftarrow{\lambda}_m^0/k}{1-\overleftarrow{\lambda}_m^0 M/k}\right)\left(\frac{\overrightarrow{\lambda}_m^0/k}{1-\overrightarrow{\lambda}_m^0 M/k}\right)^* + \frac{C_m}{A_m}\frac{M}{2}\left(\frac{2m\pi/kH}{1-\overleftarrow{\lambda}_m^0 M/k}\right)\left(\frac{2m\pi/kH}{1-\overrightarrow{\lambda}_m^0 M/k}\right)^*\right]\right)\right\}$$

Where $A_m = \begin{cases} H, & m=0 \\ H/2, & m>0 \end{cases}$ $\qquad$ $C_m = \begin{cases} 0, & m=0 \\ H/2, & m>0 \end{cases}$

Transmitted in Hard-Walled Duct

$$\Pi_a = \frac{1}{2\rho C} \sum_{m=0}^{N_{J-1}-1} A_m \left\{ a_m^{J-1} a_m^{J-1*} \left[(1+M^2) \, \text{REAL} \left(\frac{\overrightarrow{\lambda}_m^{J-1}/k}{1-\overrightarrow{\lambda}_m^{J-1}M/k} \right)^* + M \right. \right.$$

$$\left. \left. + M \left(\frac{\overrightarrow{\lambda}_m^{j-1}/k}{1-\overrightarrow{\lambda}_m^{j-1}M/k} \right) \left(\frac{\overrightarrow{\lambda}_m^{j-1}/k}{1-\overrightarrow{\lambda}_m^{j-1}M/k} \right)^* \right] \right\}$$

$$\Pi_b = \frac{1}{2\rho C} \sum_{m=0}^{N_{J-1}-1} A_m \left\{ a_m^{J-1} a_m^{J-1*} \left[\text{REAL} \left(\frac{\overrightarrow{\lambda}_m^{J-1}/k}{1-\overrightarrow{\lambda}_m^{J-1}M/k} \right)^* + \frac{M}{2} \right. \right.$$

$$\left. \left. + \frac{M}{2} \left(\frac{\overrightarrow{\lambda}_m^{J-1}/k}{1-\overrightarrow{\lambda}_m^{J-1}M/k} \right) \left(\frac{\overrightarrow{\lambda}_m^{J-1}/k}{1-\overrightarrow{\lambda}_m^{J-1}M/k} \right)^* + \frac{C_m}{A_m} \quad \frac{M}{2} \left(\frac{2m\pi/kH}{1-\overrightarrow{\lambda}_m^{J-1}M/k} \right) \left(\frac{2m\pi/kH}{1-\overrightarrow{\lambda}_m^{J-1}M/k} \right)^* \right] \right\} \tag{G2}$$

Transmitted in Soft-Walled Duct

$$\Pi_a = \frac{1}{2\rho C} \, \text{REAL} \sum_{n=0}^{N_J-1} \sum_{m=0}^{N_J-1} \left\{ a_n^j a_m^{j*} e^{-i(\overrightarrow{\lambda}_n^j - \overrightarrow{\lambda}_m^j)Z_j} \left[M + (1+M^2)\overrightarrow{\Gamma}_m^{j*} + M\overrightarrow{\Gamma}_n^j \overrightarrow{\Gamma}_m^{j*} \right] \left[\overrightarrow{\mu}_n^j \tan(\overrightarrow{\mu}_n^j H/2) \right. \right.$$

$$\left. - \overrightarrow{\mu}_m^j \tan(\overrightarrow{\mu}_m^{j*} H/2) \right] \left[\frac{2\cos(\overrightarrow{\mu}_n^j H/2)\cos(\overrightarrow{\mu}_m^{j*} H/2)}{(\overrightarrow{\mu}_n^j)^2 - (\overrightarrow{\mu}_m^{j*})^2} \right] + a_n^j b_m^{j*} e^{-i(\overrightarrow{\lambda}_n^j \overleftarrow{\lambda}_n^{j*})Z_j - i\overleftarrow{\lambda}_m^{j*}L_j} \left[M + (1+M^2)\overleftarrow{\Gamma}_m^{j*} \right.$$

$$\left. + M\overrightarrow{\Gamma}_n^j \overleftarrow{\Gamma}_m^{j*} \right] \left[\overrightarrow{\mu}_n^j \tan(\overrightarrow{\mu}_n^j H/2) - \overleftarrow{\mu}_m^{j*}\tan(\overleftarrow{\mu}_m^{j*} H/2) \right] \left[\frac{2\cos(\overrightarrow{\mu}_n^j H/2)\cos(\overleftarrow{\mu}_m^{j*} H/2)}{(\overrightarrow{\mu}_n^j)^2 - (\overleftarrow{\mu}_m^{j*})^2} \right] \tag{G3}$$

$$+ a_m^{j*} b_n^j e^{-i(\overleftarrow{\lambda}_n^j - \overrightarrow{\lambda}_m^{j*})Z_j + i\overleftarrow{\lambda}_n^j L_j} \left[M + (1+M^2)\overrightarrow{\Gamma}_m^{j*} + M\overleftarrow{\Gamma}_n^j \overrightarrow{\Gamma}_m^{j*} \right] \left[\frac{2\cos(\overleftarrow{\mu}_n^j H/2)\cos(\overrightarrow{\mu}_m^{j*} H/2)}{(\overleftarrow{\mu}_n^j)^2 - (\overrightarrow{\mu}_m^{j*})^2} \right] \left[\overleftarrow{\mu}_n^j \tan(\overleftarrow{\mu}_n^j H/2) \right.$$

$$\left. - \overrightarrow{\mu}_m^{j*} \tan(\overrightarrow{\mu}_m^{j*} H/2) \right] + b_n^j b_m^{j*} e^{-i(\overleftarrow{\lambda}_n^j - \overrightarrow{\lambda}_m^{j*})(Z_j - L_j)} \left[M + (1+M^2)\overrightarrow{\Gamma}_m^{j*} + M\overleftarrow{\Gamma}_n^j \overrightarrow{\Gamma}_m^{j*} \right] \left[\overleftarrow{\mu}_n^j \tan(\overleftarrow{\mu}_n^j H/2) \right.$$

$$\left. - \overleftarrow{\mu}_m^{j*}\tan(\overleftarrow{\mu}_m^{j*} H/2) \right] \left[\frac{2\cos(\overleftarrow{\mu}_n^j H/2)\cos(\overleftarrow{\mu}_m^{j*} H/2)}{(\overleftarrow{\mu}_n^j)^2 - (\overleftarrow{\mu}_m^{j*})^2} \right]$$

$$
\Pi_b = \frac{1}{2PC}\, \text{REAL} \sum_{n=0}^{N_j-1} \sum_{m=0}^{N_j-1} \left\{ a_n^j a_m^{j*}\, e^{-i(\overrightarrow{\lambda}_n^j - \overrightarrow{\lambda}_m^{j*})Z_j} \left\{ \left[\overrightarrow{\Gamma}_m^{j*} + M + \frac{M}{2}\, \overrightarrow{\Gamma}_n^j \overrightarrow{\Gamma}_m^{j*} \right] \left[\frac{2\cos(\overrightarrow{\mu}_n^j H/2)\cos(\overrightarrow{\mu}_m^{j*}H/2)}{(\overrightarrow{\mu}_n^j)^2 - (\overrightarrow{\mu}_m^{j*})^2} \right] \left[\overrightarrow{\mu}_n^j \tan(\overrightarrow{\mu}_n^j H/2) \right. \right. \right.
$$

$$
\left. \left. - \overrightarrow{\mu}_m^{j*}\tan(\overrightarrow{\mu}_m^j H/2) \right] + \frac{M}{2}\, \overrightarrow{\sigma}_n^j \overrightarrow{\sigma}_m^{j*} \left[\frac{2\sin(\overrightarrow{\mu}_n^j H/2)\sin(\overrightarrow{\mu}_m^{j*}H/2)}{(\overrightarrow{\mu}_n^j)^2 - (\overrightarrow{\mu}_m^{j*})^2} \right] \left[\overrightarrow{\mu}_m^{j*}\cot(\overrightarrow{\mu}_m^{j*}H/2) - \overrightarrow{\mu}_n^j \cot(\overrightarrow{\mu}_n^j H/2) \right] \right\}
$$

$$
+ a_n^j b_m^{j*}\, e^{-i(\overrightarrow{\lambda}_n^j - \overleftarrow{\lambda}_m^{j*})Z_j - i\overleftarrow{\lambda}_m^{j*}L_j} \left\{ \left[M + \overleftarrow{\Gamma}_m^{j*} + \frac{M}{2}\, \overrightarrow{\Gamma}_n^j \overleftarrow{\Gamma}_m^{j*} \right] \left[\frac{2\cos(\overrightarrow{\mu}_n^j H/2)\cos(\overleftarrow{\mu}_m^{j*}H/2)}{(\overrightarrow{\mu}_n^j)^2 - (\overleftarrow{\mu}_m^{j*})^2} \right] \left[\overrightarrow{\mu}_n^j \tan(\overrightarrow{\mu}_n^j H/2) \right. \right.
$$

$$
\left. \left. - \overleftarrow{\mu}_m^{j*}\tan(\overleftarrow{\mu}_m^j H/2) \right] + \frac{M}{2}\, \overrightarrow{\sigma}_n^j \overleftarrow{\sigma}_m^{j*} \left[\frac{2\sin(\overrightarrow{\mu}_n^j H/2)\sin(\overleftarrow{\mu}_m^{j*}H/2)}{(\overrightarrow{\mu}_n^j)^2 - (\overleftarrow{\mu}_m^{j*})^2} \right] \left[\overleftarrow{\mu}_m^{j*}\cot(\overleftarrow{\mu}_m^{j*}H/2) - \overrightarrow{\mu}_n^j \cot(\overrightarrow{\mu}_n^j H/2) \right] \right\}
$$

$$
+ a_m^{j*} b_n^j\, e^{-i(\overleftarrow{\lambda}_n^j - \overrightarrow{\lambda}_m^{j*})Z_j + i\overleftarrow{\lambda}_n^j L_j} \left\{ \left[M + \overrightarrow{\Gamma}_m^{j*} + \frac{M}{2}\, \overleftarrow{\Gamma}_n^j \overrightarrow{\Gamma}_m^{j*} \right] \left[\frac{2\cos(\overleftarrow{\mu}_n^j H/2)\cos(\overrightarrow{\mu}_m^{j*}H/2)}{(\overleftarrow{\mu}_n^j)^2 - (\overrightarrow{\mu}_m^{j*})^2} \right] \left[\overleftarrow{\mu}_n^j \tan(\overleftarrow{\mu}_n^j H/2) \right. \right.
$$

$$
\left. \left. - \overrightarrow{\mu}_m^{j*}\tan(\overrightarrow{\mu}_m^j H/2) \right] + \frac{M}{2}\, \overleftarrow{\sigma}_n^j \overrightarrow{\sigma}_m^{j*} \left[\frac{2\sin(\overleftarrow{\mu}_n^j H/2)\sin(\overrightarrow{\mu}_m^{j*}H/2)}{(\overleftarrow{\mu}_n^j)^2 - (\overrightarrow{\mu}_m^{j*})^2} \right] \left[\overrightarrow{\mu}_m^{j*}\cot(\overrightarrow{\mu}_m^{j*}H/2) - \overleftarrow{\mu}_n^j \cot(\overleftarrow{\mu}_n^j H/2) \right] \right\}
$$

$$
+ b_n^j b_m^{j*}\, e^{-i(\overleftarrow{\lambda}_n^j - \overleftarrow{\lambda}_m^{j*})(Z_j - L_j)} \left\{ \left[M + \overleftarrow{\Gamma}_m^{j*} + \frac{M}{2}\, \overleftarrow{\Gamma}_m^{j*}\overleftarrow{\Gamma}_n^j \right] \left[\frac{2\cos(\overleftarrow{\mu}_n^j H/2)\cos(\overleftarrow{\mu}_m^{j*}H/2)}{(\overleftarrow{\mu}_n^j)^2 - (\overleftarrow{\mu}_m^{j*})^2} \right] \left[\overleftarrow{\mu}_n^j \tan(\overleftarrow{\mu}_n^j H/2) \right. \right.
$$

$$
\left. \left. - \overleftarrow{\mu}_m^{j*}\tan(\overleftarrow{\mu}_m^j H/2) \right] + \frac{M}{2}\, \overleftarrow{\sigma}_n^j \overleftarrow{\sigma}_m^{j*} \left[\frac{2\sin(\overleftarrow{\mu}_n^j H/2)\sin(\overleftarrow{\mu}_m^{j*}H/2)}{(\overleftarrow{\mu}_n^j)^2 - (\overleftarrow{\mu}_m^{j*})^2} \right] \left[\overleftarrow{\mu}_m^{j*}\cot(\overleftarrow{\mu}_m^{j*}H/2) - \overleftarrow{\mu}_n^j \cot(\overleftarrow{\mu}_n^j H/2) \right] \right\} \right\}
$$

(G3)

where

$$
\Gamma_n^j = \frac{\lambda_n^j/k}{1 - \lambda_n^j M/k}
$$

$$
\sigma_n^j = \frac{\mu_n^j/k}{1 - \lambda_n^j M/k}
$$

97

APPENDIX H

COMPARISON OF INFINITE AND FINITE DUCT THEORIES
FOR SINGLE-SEGMENT OPTIMUM LINERS

Although E. J. Rice of NASA Lewis (personal communication) has carried out extensive investigations of uniform liners optimized for specified input pressure distribution and liner lengths, his studies have been based on infinite duct theory. That is, spurious mode generation due to the step-function transitions in wall impedance from soft walls to hard walls at the segment ends was neglected, and only right-moving waves were considered. As part of the present segmented duct study, an investigation was made of single-segment optimum liners including wave reflections from the wall impedance discontinuities.

It was discovered during preliminary data comparisons that excellent correlation existed between the finite length single-segment optimums and Rice's plane wave infinite soft-wall duct optimums. The data of Figure H1 show that the infinite and finite duct results are in good agreement. These results raised the question of whether complete modal expansions, including reflected waves, are even necessary for dissipative liner combinations which do not include low resistance segments.

To answer this question, a program was developed to compute attenuations in infinite soft-wall ducts for initial pressure patterns corresponding to various combinations of hard-wall duct modes. Runs were made with this program and with the semi-infinite hard-wall to soft-wall mode matching program to check out the single-segment optimums. Figure H2 shows attenuation contours in the impedance plane for the single-segment plane wave optimum as determined using the finite duct theory at $kH/2\pi = \eta = 1.6$ and $L/H = 3.0$. In addition, points corresponding to values obtained using the infinite duct theory have been identified. These points may be seen to agree quite well with the finite theory values. Similar data are shown on Figure H3 which depicts the attenuation contours for the case with both the first two modes incident, at equal energy, and in phase. Thus, the infinite and finite theories are in good agreement for other modal inputs, as well as for plane wave incidence.

Since these data were all run for $kH/2\pi = 1.6$, a frequency condition midway between two modal cut-on values, it was decided that further runs should be made at $kH/2\pi = 1.0$ and $kH/2\pi = 2.0$. At these frequencies, which correspond to modal cut-on values, the amplitudes of the spuriously generated second and third modes at the hard-wall to soft-wall interface should reach their largest values. Figure H4 contains tabulations of attenuation values obtained using the finite, infinite, and semi-infinite theories at $kH/2\pi = \eta = 1.0$ and $L/H = 0.5$. Quite poor agreement is evident between the semi-infinite and infinite results, and even poorer agreement between the finite and infinite cases, indicating that the incident pressure distribution was distorted by spurious generation of the second mode at the hard-wall to soft-wall junctions. It should be noted that the finite length attenuations indicate that the optimum impedance is tending toward a low resistance (reactive) liner, a trend also seen near $kH/2\pi = 1.0$ in the single-segment optimizations. This appears to be due to the fact that $\eta = 1.0$ corresponds to cut-on of the second mode; at this frequency, it is apparently more efficient to reflect energy in the second mode than to dissipate it in the plane wave. For plane wave incidence at $kH/2\pi = 2.0$ on a liner of length $L/H = 3.0$ (Figure H5), there was no essential difference between infinite and hard-wall to soft-wall theory predictions. Consequently, it appears that there is little tendency for the third mode to be spuriously generated by the lining impedance discontinuities.

In summary, it appears that infinite or semi-infinite theories may be used for single-segment lining design provided that:

- The liner is highly dissipative (no low resistance segment to cause reflections or standing wave patterns)

- The complex pressure distribution at the entrance to the segment is accurately represented

- The excitation frequency does not lie near the cut-on frequencies for the low order modes

- The duct length is not extremely small compared with the wavelength of the incident sound
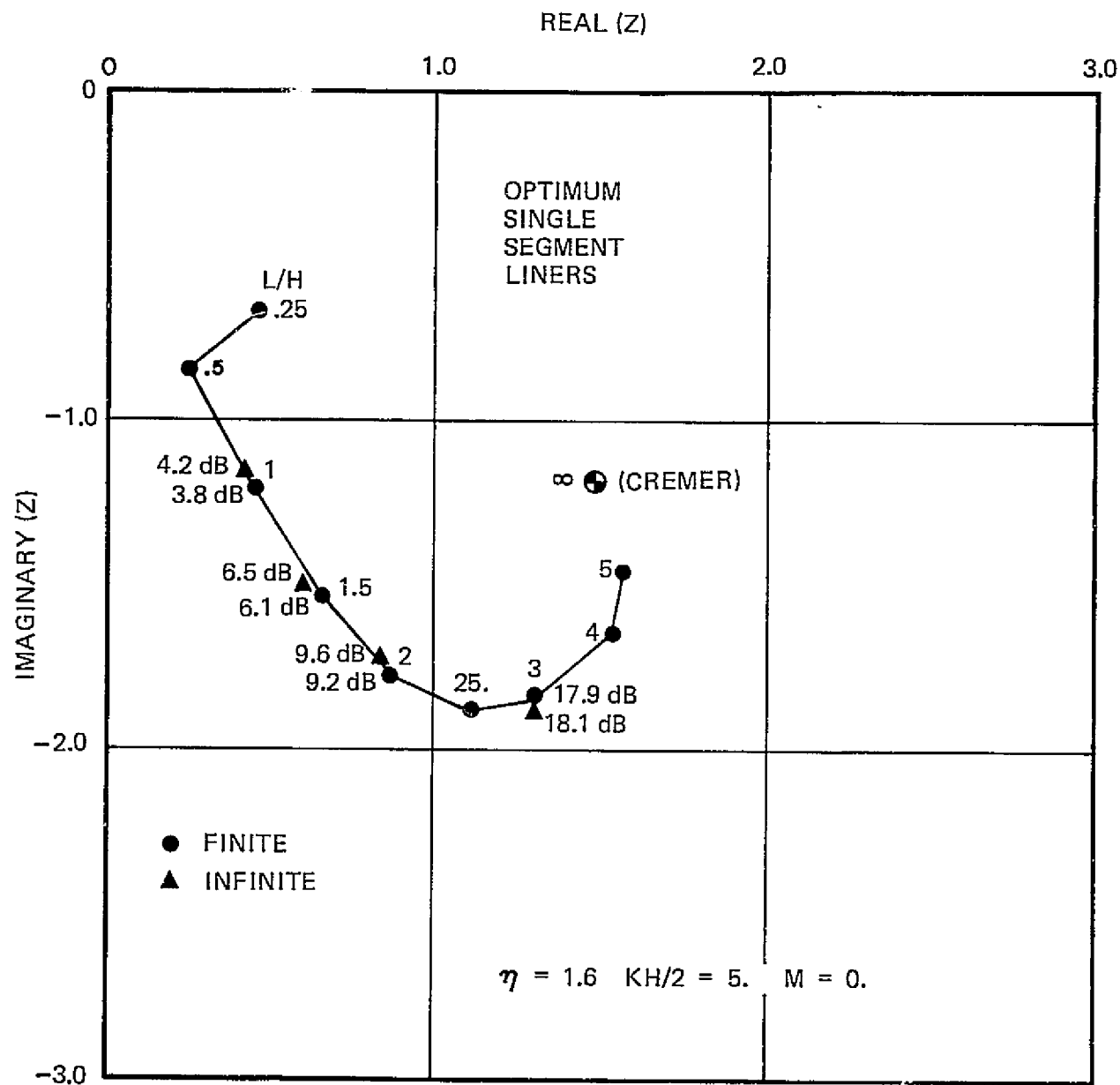
Figure H1.   Comparison of Infinite and Finite Duct Theories for
Plane Wave Single Segment Optimums, M = 0.

Figure H2. Comparison of Infinite and Finite Duct Theories for Single Segment Sound Power Level Attenuation Contours, M = 0.

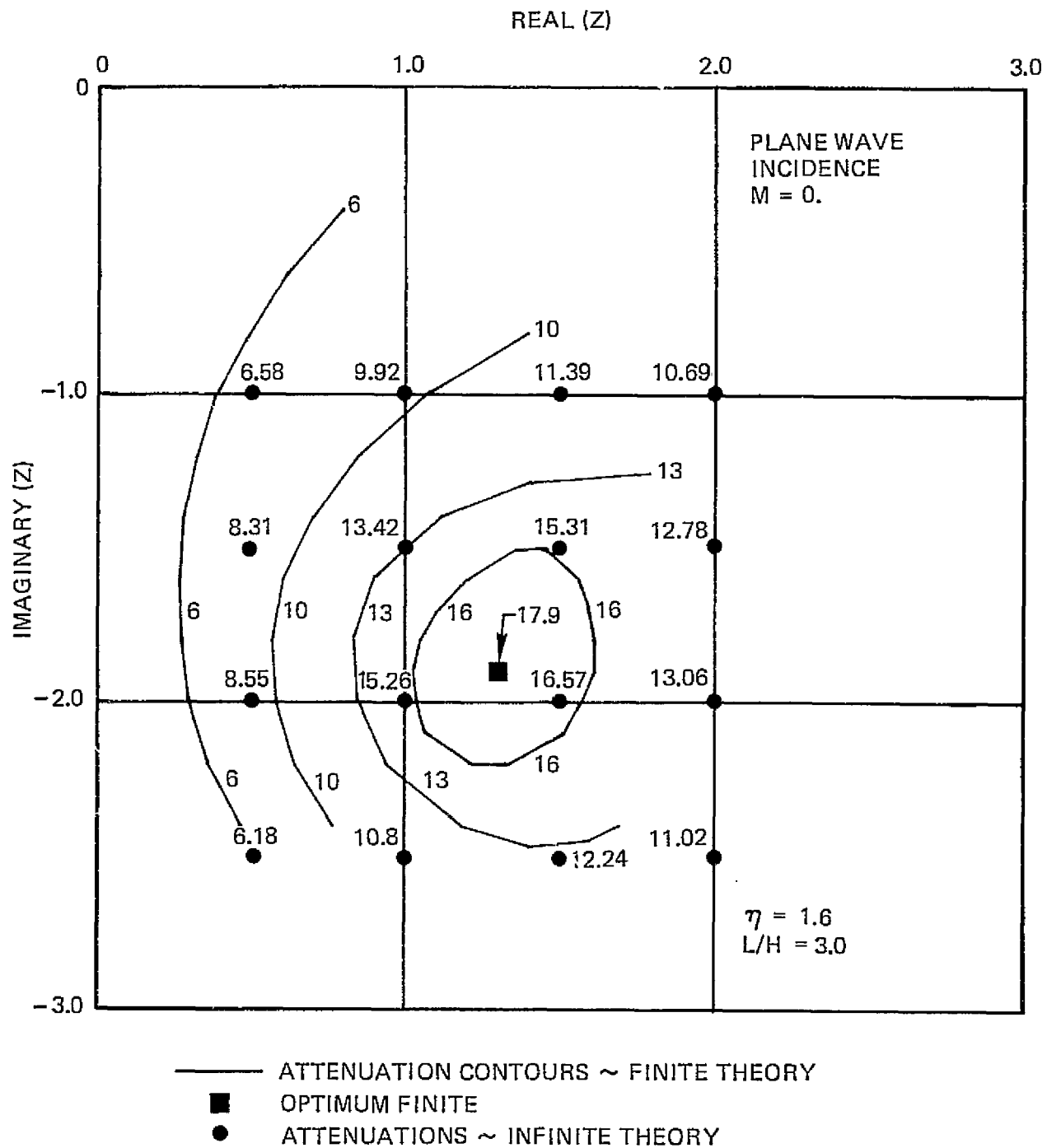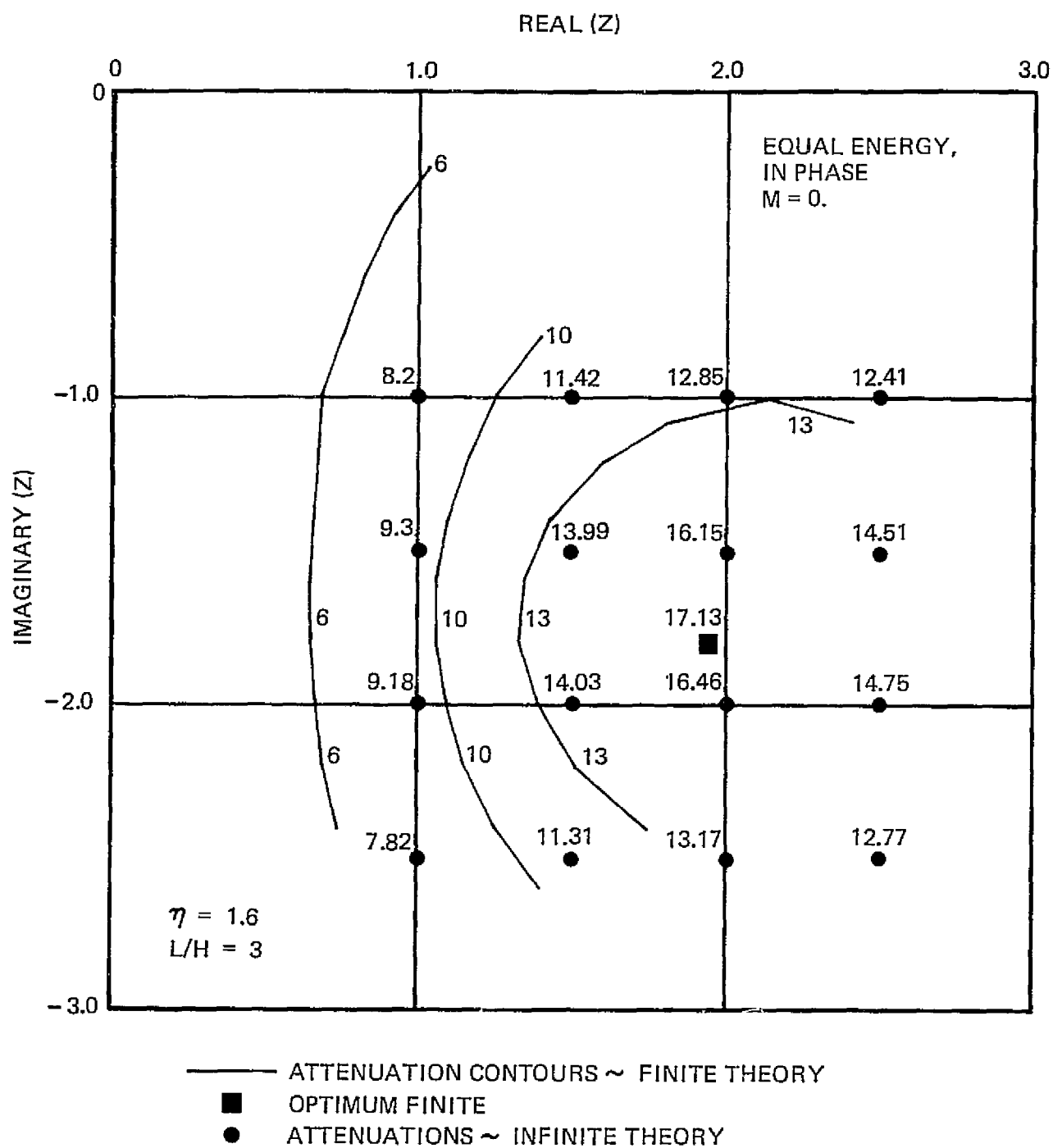Figure H3. Comparison of Infinite and Finite Duct Theories for Single Segment Sound Power Level Attenuation Contours, M = 0.
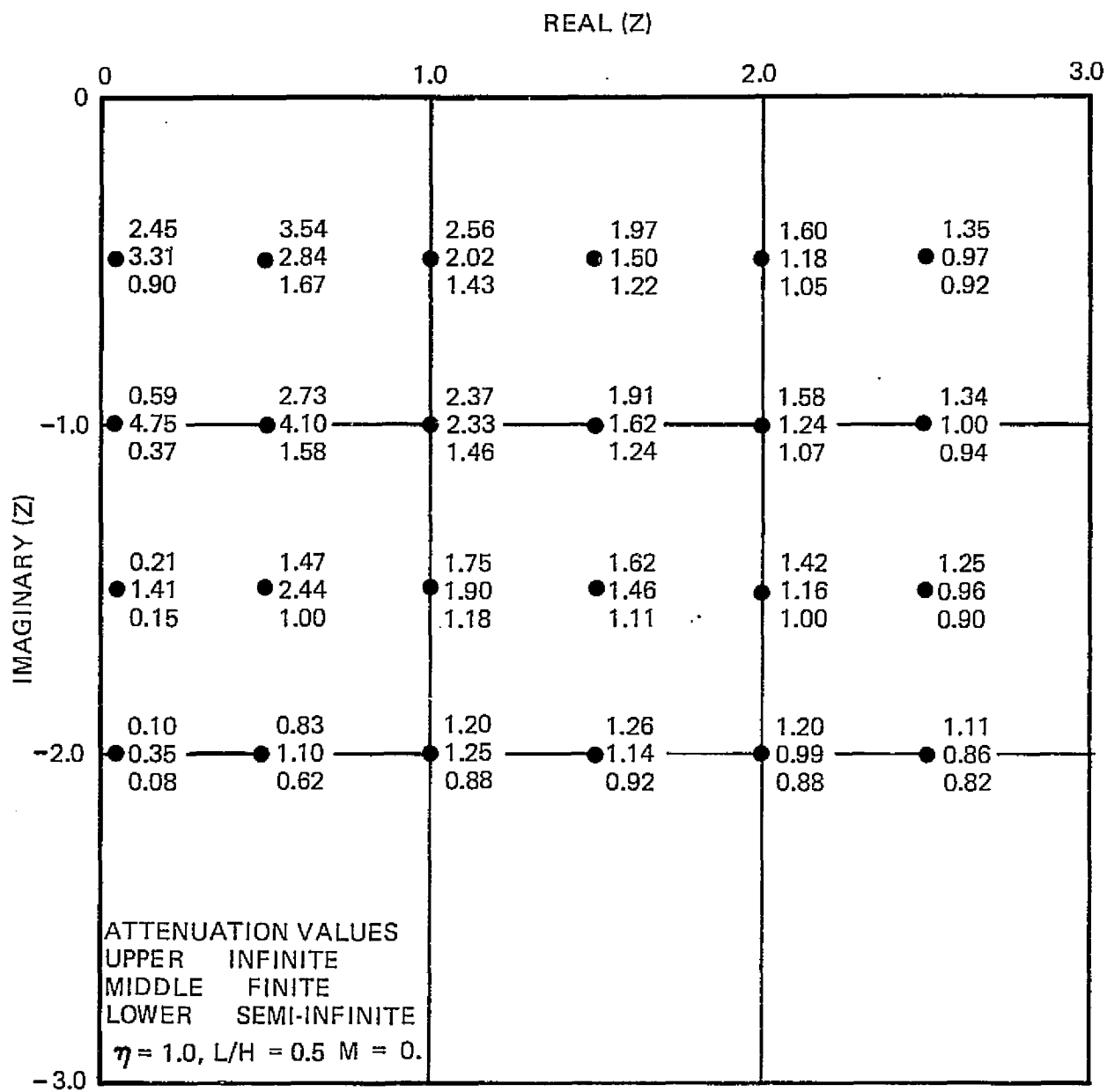
REAL (Z)

Figure H4. Comparison of Infinite, Semi-Infinite, and Finite Duct Theories for Single Segment Sound Power Level Attenuation Contours, M = 0, Plane Wave Incident.
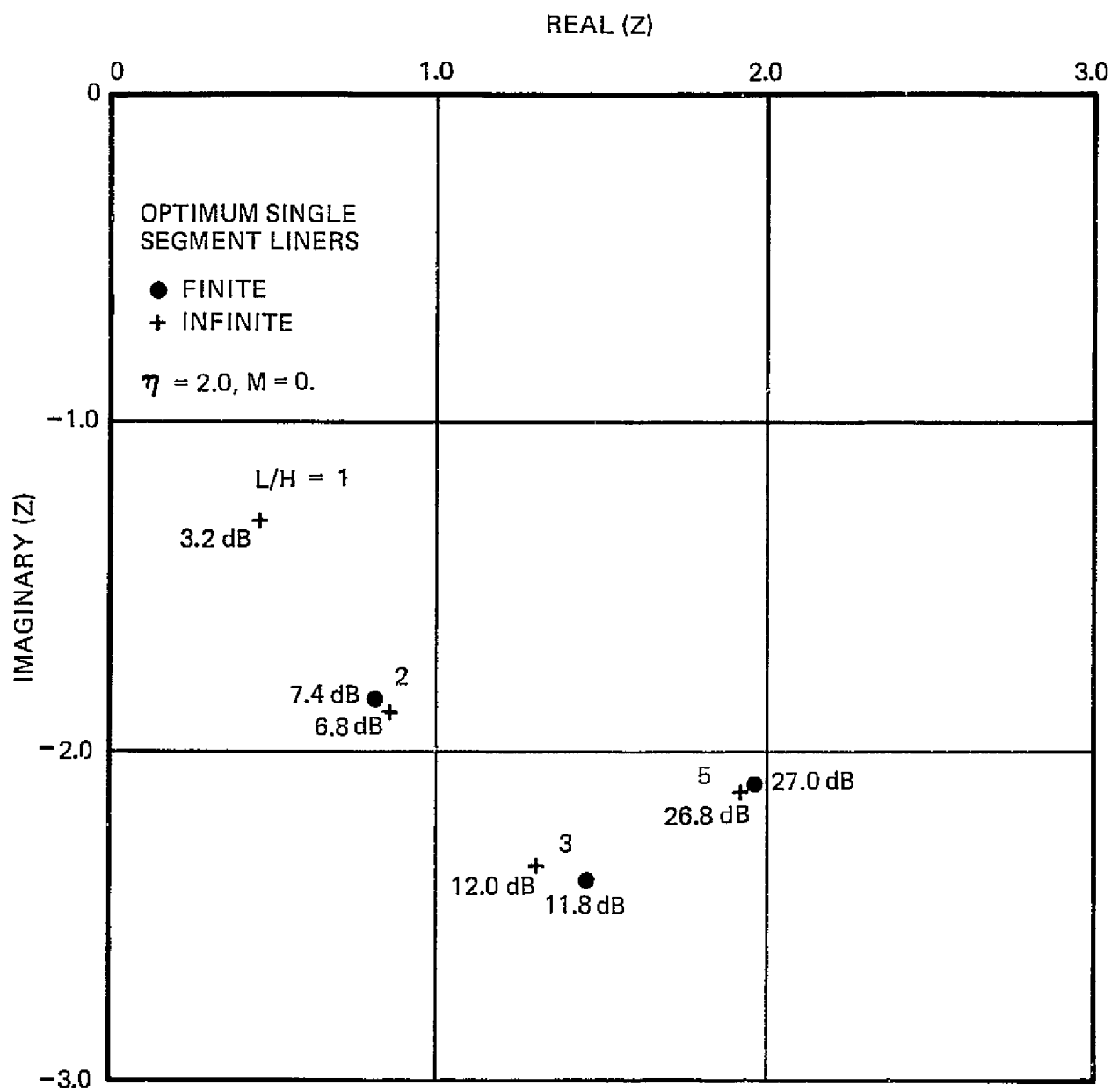
Figure H5. Comparison of Infinite and Finite Duct Theories for Plane Wave
Single Segment Optimums, M = 0.

APPENDIX J

DETERMINATION OF MODEL COEFFICIENTS
FROM
GRAZING FLOW DUCT HARDWALL AXIAL PRESSURE TRAVERSE DATA

For the hardwall duct configuration, the pressure may be expressed in terms of the following expansion:

$$p = \sum_{n=0}^{N-1} a_n \cos(2n\pi y/H) e^{-i\overrightarrow{\lambda}_n z} + \sum_{n=0}^{N-1} b_n \cos(2n\pi y/H) e^{-i\overleftarrow{\lambda}_n (z-L)} \tag{J1}$$

Where $z = 0$ at the beginning (reference microphone) measuring point, and $z = L$ is the location of the end of the uniform cross section portion of the duct (i.e., the beginning of the duct terminating horn). The measured data are comprised of the quantities dB (z) and degree (z) on $y = 0$ (Figure J1):

$$dB\ (z) = 10\ \log_{10} \left(P_{WALL}\ (z)\ P^*_{WALL}\ (z)/P_{REF}\ P^*_{REF} \right) \tag{J2}$$

$$degree\ (z) = 180\ (\phi_{REF} - \phi_{WALL}\ (z))/\pi$$

where the traveling probe measures

$$P_{WALL}(Z) = \left| P_{WALL}(Z) \right| e^{-i\phi_{WALL}(Z)} \tag{J3}$$

and the reference probe measures

$$P_{REF} = \left| P_{REF} \right| e^{-i\phi_{REF}} \tag{J4}$$

Note that (J3) can be written

$$P_{WALL}\ (Z) = 10^{dB(Z)/20} \left| P_{REF} \right| e^{i[\pi \deg(Z)/180 - \phi_{REF}]} \tag{J5}$$
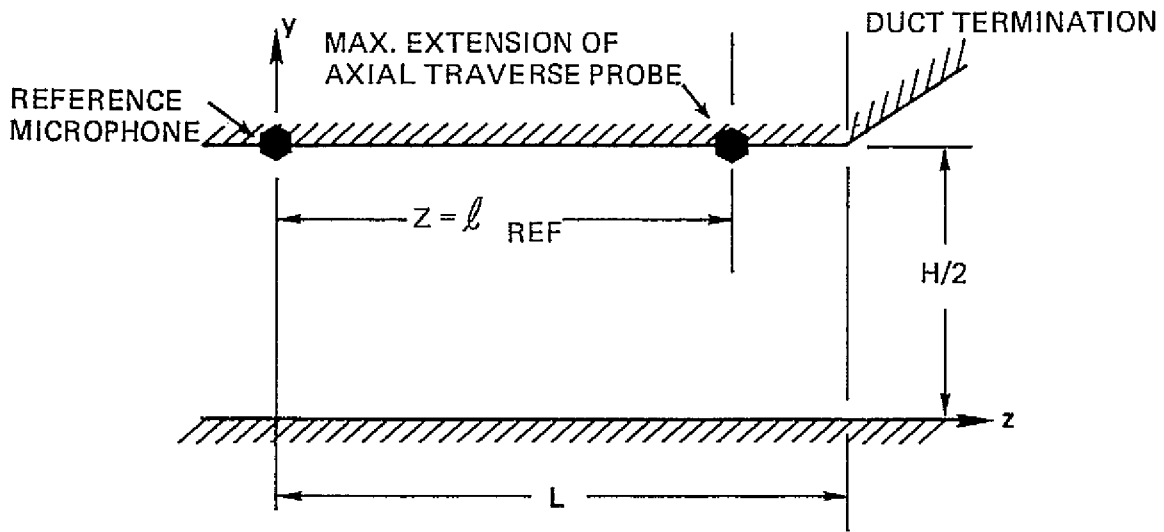
Figure J1.   Geometry for Modal Identification

To determine the modal coefficients a_n and b_n, we require that

$$p(y = 0,z) = P_{WALL} \, (z) \quad \text{on } 0 \leq z \leq L_{REF} \tag{J6}$$

where L_{REF} is the total traverse length. We have chosen to impose (J6) by defining an integral squared error:

$$E^2 = \int_0^{L_{REF}} \left[p(y = 0,z) - P_{WALL} z\text}\right] \left[p^*(y=0,z) - P^*_{WALL} \, (z) \right] dZ \tag{J7}$$

and requiring that the error be minimized with respect to the coefficients:

$$\partial E^2 / \partial a_m = 0, \ \partial E^2 / \partial b_m = 0, \ m = 0, (1), N\text{-}1 \tag{J8}$$

Alternatively, one could impose

$$\partial E^2 / \partial a_m^* = 0, \ \partial E^2 / \partial b_m^* = 0, \ m = 0, (1), N\text{-}1 \tag{J9}$$

108

Equations (J8) and (J9) are equivalent, producing complex conjugate equation sets for a_n^*, b_n^*, and a_n, b_n, respectively. We choose to solve the set for a_n, b_n:

$$\sum_{n=0}^{N-1} a_n \int_0^{L_R} e^{-i\overrightarrow{\lambda_n}z + i\overrightarrow{\lambda_m}^* z}\, dz \;\dotplus\; \sum_{n=0}^{N-1} b_n \int_0^{L_R} e^{-i\overleftarrow{\lambda_n}(z-L) + i\overrightarrow{\lambda_m}^* z}\, dz \tag{J10}$$

$$= \left| P_{REF} \right| \int_0^{L_R} 10^{dB(z)/20}\, e^{i\overrightarrow{\lambda_m}^* z \;+\; i\pi \deg(z)/180 \;-\; i\phi_{ref}}\, dz$$

$$m = 0, (1), N-1$$

$$\sum_{n=0}^{N-1} a_n \int_0^{L_R} e^{-i\overrightarrow{\lambda_n}z + i\overleftarrow{\lambda_m}^*(z-L)}\, dZ \;+\; \sum_{n=0}^{N-1} b_n \int_0^{L_R} e^{-i\overleftarrow{\lambda_n}(z-L) + i\overleftarrow{\lambda_m}^*(z-L)}\, dz \tag{J11}$$

$$= \left| P_{REF} \right| \int_0^{L_R} 10^{dB(z)/20}\, e^{i\overleftarrow{\lambda_m}^*(z-L) + i\pi \deg(z)/180 \;-\; i\phi_{ref}}\, dz$$

$$m = 0, (1), N-1$$

The integrals on the right-hand sides of (J10) and (J11) must be evaluated numerically. Since the test data are digitized at equal sampling intervals, the numerical integration was performed using an equal interval (Simpson) method.

REFERENCES

1. Eversman, W., Nelsen, M. D., Armstrong, D., and Hall, O. J., "Design of Acoustic Linings for Ducts with Flow," J. Aircraft, Vol. 9, No. 8, pp. 548-556, August 1972.

2. Cremer, L., "Theorie der Luftschall-Dampfung in Rechtekanal mit Schluckender Wand und das sich dabei Ergebende hochste Dampfungsmass," Acustica, Vol. 3, pp. 249-263, 1953.

3. Tester, B. J., "The Optimization of Modal Sound Attenuation in Ducts, in the Absence of Mean Flow," J. Sound Vib., Vol. 27, pp. 477-513, 1973.

4. Zorumski, W. E., and Mason, J. P., "Multiple Eigenvalues of Sound-Absorbing Circular and Annular Ducts," J. Acoust. Soc. America, Vol. 55, pp. 1158-1165, 1974.

5. Rice, E. J., "Attenuation of Sound in Soft-Wall Ducts," NASA TM X-52442, 1968.

6. Snow, D. J., "Influence of Source Characteristics on Sound Attenuation in a Lined Circular Duct," J. Sound Vib., Vol. 37, pp. 459-465, 1974.

7. Lansing, D. L. and Zorumski, W. E., "Effects of Wall Admittance Changes on Duct Transmission and Radiation of Sound," J. Sound Vib., Vol. 27, pp. 85-100, 1973.

8. Zorumski, W. E., "Acoustic Theory of Axisymmetric Multisectioned Ducts," NASA TR-R-419, 1974.

9. Alfredson, R. J., "The Propagation of Sound in a Circular Duct of Continuously Varying Cross-Sectional Area," J. Sound Vib., Vol. 23, pp. 433-442, 1972.

10. Beckemeyer, R. J. and Eversman, W., "Computational Methods for Studying Acoustic Propagation in Nonuniform Waveguides," AIAA Paper 73-1006, AIAA Aero-Acoustics Specialist Conference, Seattle, Washington, 1973.

11. Eversman, W., Cook, E. L., and Beckemeyer, R. J., "A Method of Weighted Residuals for the Investigation of Sound Transmission in Nonuniform Ducts Without Flow," J. Sound Vib., Vol. 38, pp. 105-123, 1975.

12. Sawdy, D. T., Beckemeyer, R. J., and Garner, P., "Effects of a Conical Segment on Sound Radiation from a Circular Duct," AIAA Paper 75-517, AIAA 2nd Aero-Acoustics Specialist Conference, Hampton, Virginia, 1975.

13. Nagelberg, E. R. and Shefer, "Mode Conversion in Circular Waveguides," Bell System Tech. Journal, pp. 1321-1338, 1965.

14. Clarricoats, P. J. B. and Slinn, K. R., "Numerical Solution of Waveguide Discontinuity Problems," Proc. IEE, Vol. 114, pp. 878-886, 1967.

15. Masterman and Clarricoats, "Computer Field Matching Solution of Waveguide Transverse Discontinuities," Proc. IEE, Vol. 118, pp. 57-63, 1971.

PRECEDING PAGE BLANK NOT FILMED

16. Martenson, A. J. and Liu, H. K., "Optimum Lining Configurations," NASA SP-207, pp. 425-434, 1969.

17. Wilkinson, J. P. D., "The Calculation of Optimal Linings for Jet Engine Inlet Ducts," NASA CR-1832, August 1971.

18. Kessler, F. M. and Puri, N. N., "Acoustic Filter Synthesis Using Conjugate Gradient Search Techniques," J. Acoustical Soc. America, Vol. 49, No. 5 (Part 1), 1971.

19. Tam, C. K. W., "Transmission of Spinning Modes in a Slightly Nonuniform Duct," J. Sound Vib., Vol. 18, pp. 339-351, 1971.

20. Salant, R. F., "Acoustic Propagation in Waveguides with Sinusoidal Walls," J. Acoust. Soc. Am., Vol. 53, pp. 504-507, 1973.

21. Nayfeh, A. H. and Telionis, D. P., "Acoustic Propagation in Ducts with Varying Cross Section," VPI Engineering Report VPI-E-73-7, Virginia Polytechnic Institute, March 1973.

22. Quinn, D. W., "A Finite Difference Method for Computing Sound Propagation in Nonuniform Ducts," AIAA Paper 75-130, 13th Aerospace Sciences Meeting, Pasadena, California, January 1975.

23. Baumeister, K. J., "Application of Finite Difference Techniques to Noise Propagation in Jet Engine Ducts," NASA TM-X-68261, Lewis Research Center, Cleveland, Ohio, November 1973.

24. Eversman, W., Cook, E. L., and Beckemeyer, R. J., "A Computational Method for the Investigation of Sound Transmission in Nonuniform Ducts," Proceedings of the Second Interagency Symposium on University Research in Transportation Noise, North Carolina State University, Raleigh, North Carolina, pp. 859-873, June 5-7, 1974.

25. Beckemeyer, R. J., "Computational Methods for Analyzing Nonuniform Acoustic Waveguides," PhD Thesis, University of Kansas, 1974.

26. Eversman, W. and Beckemeyer, R. J., "Transmission of Sound in Ducts with Thin Shear Layers — Convergence to the Uniform Flow Case," J. Acoustical Society of America, Vol. 52, No. 1 (Part 2), pp. 216-220, 1972.

27. Eversman, W., "The Effect of Mach Number on the Tuning of an Acoustic Lining in a Flow Duct," J. Acoust. Soc. America, Vol. 48, No. 2 (Part 1), pp. 425-428, 1970.

28. Yurkovich, R., "Attenuation of Acoustic Modes in Circular and Annular Ducts in the Presence of Uniform Flow," AIAA Paper 74-552, AIAA 7th Fluid and Plasma Dynamics Conference, Palo Alto, California, 1974.

29. Goldstein, M. E., "Aeroacoustics," NASA SP-346, NASA Lewis Research Center, 1974.

30. Morfey, C. L., "Acoustic Energy Flux in Nonuniform Flows," J. Sound Vib., Vol. 14, No. 2, pp. 159-170, 1971.

31. Ryshov, O. S., and Shefter, G. M., "On the Energy of Acoustic Waves Propagating in Moving Media," J. Appl. Math. Mech., Vol. 26, No. 5, pp 1293-1309, 1962.

32. Heins, A. H. and Feshbach, H., "The Coupling of Two Acoustical Ducts," J. Math Physics, Vol. 26, pp. 143-155, 1947.

33. Rice, E. J., "Propagation of Waves in an Acoustically Lined Duct with a Mean Flow," NASA SP-207, pp. 345-355, 1969.

34. Unruh, J. F., "Acoustic Mode Matching for Segmented Lining Design — Part I Theory," Boeing Document D6-40124, 1975.

35. Baumeister, K. J., "Generalized Wave Envelope Analysis of Sound Propagation in Ducts with Stepped Noise Source Profiles and Variable Axial Impedance," NASA TM X-71674, Lewis Research Center, Cleveland, Ohio, March 1975.

36. Quinn, D.W., "Attenuation of Sound Associated with a Plane Wave in a Multisectioned Cylindrical Duct," AIAA Paper 75-496, American Institute of Aeronautics and Astronautics Second Aero-Acoustics Specialist Conference, Hampton, Virginia, 1975.

37. Patterson, J.D., Sawdy, D.T., and Beckemeyer, R. J., "Test Results in Support of a Study of an Optimum Multisegmented Lining Noise Suppression Concept," Boeing Document D3-9812-2, Wichita, Kansas, 1975.

38. Lester, H. C., and Posey, J. W., "Duct Liner Optimization for Turbomachinery Noise Sources," NASA TM X-72789, NASA Langley Research Center, November, 1975.

39. Eversman, W., "Signal Velocity in a Duct with Flow," J. Acoustical Society of America, Vol. 50, pp. 421-425, 1971.